MOTC-IOT-IHMT-89-008

非線性波浪引起港池振盪之研究(二)

著作：劉立方、蔡丁貴、蘇青和

交通部
運輸研究所 港灣技術研究中心 委託

國立台灣大學土木工程研究所 辦理

中華民國 八十九 年 十二 月

交通部運輸研究所港灣技術研究中心委託研究計畫出版品摘要表

出版品名稱：非線性波浪引起港池振盪之研究(二)

國際標準書號（或叢刊號）	政府出版品統一編號	港灣技術研究中心出版品編號
	009254890350	MOTC-IOT-IHMT-89-008

本中心主辦單位：數學模式組 主管：簡仲璟 主辦人員：蘇青和 聯絡電話：04-6564216~408 傳真號碼：04-6571329	委託研究單位：台灣大學土木研究 計畫主持人：蔡丁貴 研究人員：劉立方 地址：台北市羅斯福路台灣大學 聯絡電話：02-23630231~2408~16	研究期間 自 89 年 1 月 至 89 年 12 月

關鍵詞：非線性波浪、港池振盪、數值模式

摘要： 本文首先說明研究計畫之背景與研究目的。研究計畫主要建立新的非線性波浪引起港池振盪之有限元素法模式，新的模式包括二維連續方程式及運動方程式之垂直積分理論建立，而描述弱非線性與弱分散波也爲本模式之基礎。本年度主要探討二維之問題,爲適合Galerkin 有限元素法計算,首先將控制方程式做重新整理,而模式之元素可採用線性三角形或四邊形。其次爲了減低數值計算時間及邊界條件之容易處理，引用部份輔助變數，輔助變數之引用也有去除第三階微分項之益處。時間積分方面引用隱性 predictor-corrector 疊代法，空間積分方面則引用Galerkin殘餘權重法,邊界條件則包括有全反射、吸收邊界、入射波邊界等。最後本文並計算數個應用例子，以探討模式可能之應用範圍及驗證模式之正確性。

出版日期	頁數	工本費	本出版品取得方式
2000 年 12 月	127	260	凡屬機密性出版品均不對外公開。普通性出版品，公營、公益機關團體及學校可函洽本中心免費贈閱；私人及私營機關團體可按工本費價購。

機密等級：

□限閱 □密 □機密 □極機密 □絕對機密

（解密【限】條件：□ 年 月 日解密，□公布後解密，□附件抽存後解密，□工作完成或會議終了時解密，□另行檢討後辦理解密）

■普通

備註：本研究之結論與建議不代表交通部運輸研究所之意見。

PUBLICATION ABSTRACTS OF RESEARCH PROJECTS
INSTITUTE OF HARBOR & MARINE TECHNOLOGY
INSTITUTE OF TRANSPORTATION
MINISTRY OF TRANSPORTATION AND COMMUNICATIONS

TITLE:Harbor Oscillations Induced by Nonlinear Transient Waves (II)

ISBN(OR ISSN)	GOVERNMENT PUBLICATIONS NUMBER	IHMT SERIAL NUMBER
	009254890350	MOTC-IOT-IHMT-89-008

DIVISION : Institute of Harbor and Marine Technology
DIVISION CHIEF : Chien, Chung-Ching
ADMINISTRATION STAFF: Su,Ching-Ho
PHONE:04-6564216-408
FAX:04-6571329

PROJECT PERIOD
FROM: 2000/01
TO : 2 000/12

RESEARCH AGENCY:Department of Civil Engineering National Taiwan University
PRINCIPAL INVESTIGATOR:Ting-Kuei Tsay
PROJECT STAFF:Philip L.-F. Liu
ADDRESS:Tapai Department of Civil Engineering National Taiwan University
PHONE:02-23630231-2408-16

KEY WORDS: nonlinear wave , numerical model, harbor oscillation

ABSTRACT: In this report a brief literature review is given first to summarize the background and research approaches of the project .The need for developing a finite element model for computing harbor oscillations induced by nonlinear transient waves is firmly established. Vertically integrated two-dimensional continuity and momentum equations, describing weakly nonlinear and weakly depressive waves, are the basis of the new finite element model. The governing equations are rearranged in such a way that it is suitable for the application of Galerkin finite element method. The present model uses linear triangular and rectangular elements and linear shape functions. To remove the third spatial derivative terms in the governing equations, an auxiliary variable is introduced. The advantage of this arrangement over other previous work is discussed in terms of computational cost and the treatment of boundary conditions. For spatial integration the Galerkin weighted residual method is used. For time integration an implicit predictor-corrector iterative scheme is employed. Several different kinds of boundary conditions, including the perfect reflecting boundary, the absorbing boundary (sponge layer) and the incident wave boundary, are implemented. Numerical results are obtained for various examples.

DATE OF PUBLICATION	NUMBER OF PAGES	PRICE	CLASSIFICATION
2000/12	127	260	☐ SECRET ☐ CONFIDENTIAL ■ UNCLASSIFIED

2D Numerical Model of Harbor Oscillations Induced by Nonlinear Waves

Contents

Harbor Oscillations Induced by Nonlinear Transient Waves (II)

Contents

Part I

2D Numerical Model of Harbor Oscillations Induced by Nonlinear Waves

1 Introduction

1.1 Background of harbor resonance

Harbor resonance is the phenomenon of trapping and amplification of wave energy inside a semi-enclosed water body, such as a harbor or a bay. If wave motions inside a harbor are forced at one or more of natural frequencies of the harbor, which depend on the harbor configuration, the amplitudes of harbor oscillations will become rather large. These large amplitude oscillations could create unacceptable vessel movements and excessive mooring forces leading to the breaking of mooring lines. In designing a new harbor or modifying an existing harbor, it is essential to have a good understanding of the natural frequencies of the harbor and the possible sources of forcing for harbor resonance. Moreover, a model, either numerical or physical model, should be used to examine the temporal and spatial variations of wave amplitudes inside the proposed harbor under design wave conditions.

Typical resonant periods for a harbor or a moored vessel are of the order of magnitude of several minutes. Therefore, harbor resonance at this frequency range is not caused directly by wind waves since wind wave periods are of the order of magnitude of several seconds. Other possible sources of resonance forcing include tsunamis, atmospheric pressure disturbances, locally generated infragravity waves, and free infragravity waves generated at and radiated from distant shores. Tsunamis and atmospheric pressure disturbances have been shown convincingly in previous studies as possible causes for harbor resonance (e.g., Carrier et al. 1971). However, they alone cannot account for the resonance problems existing in many harbors around the world. Munk (1949) was the first one who observed the infragravity waves associated with wind waves. Later, Longuet-Higgins and Stewart (1962) gave physical and mathematical explanations for the generation of free and bound infragravity waves through nonlinearity. Field observations in three small harbors (two in Hawaii and one in California) have shown that harbor resonance can be forced primarily by free infragravity waves originated in the offshore region (Okihiro et al. 1993, Okihiro and Guza 1996). However, many researchers have also shown theoretically and experimentally that bound infragravity waves (associated with groups of wind waves impinging at a harbor mouth) can cause harbor resonance (e.g., Bowers 1977, Mei and Agnon 1989, Wu and Liu 1990). Moreover, free infragravity waves can also be generated locally (inside or in the vicinity of a harbor) through interactions of bound infragravity waves and harbor boundaries.

For a simple harbor geometry with a constant depth the natural frequencies and the corresponding free surface oscillations can be predicted analytically. However, for more complex harbor geometry, for transient excitations, and for cases where nonlinear effects are important, the harbor response can be determined only from experiments conducted in a hydraulic model or with a numerical model. Although the usefulness of conducting a hydraulic model study should never be

underestimated, there are several limitations. First, it is costly to construct and modify the hydraulic model to collect data for a long duration with a fine spatial resolution. Secondly, the scaling of the hydraulic model is also a difficult issue when both short waves and infragravity waves are of interest. Therefore, research efforts focused on the development of numerical models for calculating the harbor oscillations induced by nonlinear transient waves are essential.

1.2 Wave Theories

In Principle, water wave motions can be modeled by the Navier-Stokes equations for incompressible Newtonian fluid,which represent the conservation of mass and momentum. Free surface boundary conditions, ensuring the continuity of stress tesor across the free surface, are necessary in determining the free surface location. Both the Navier-Stokes equations and the free surface boundary conditions are nonlinear. Consequently, even when the turbulence is ignored, the computational effort required for solving a truly three-dimensional wave propagation problem, which has a horizontal length scale of over hundreds or more wavelengths, is too large to be employed in engineering practice at the present time.

(1) Ray Approximation . Efforts for reducing the computation efforts are necessary and have been sought by reducing the dimension of the computational domain. Moreover,continuing efforts have been made to construct a unified model that can propagate wave from deep water into shall water, even into surf zone. The forerunner of this kind of effort is the ray approximation for infinitesimal waves propagating over bathymetry that varies slowly over horizontal distances much longer than the local wavelength. In this approximation, one frist finds wave rays by adopting the geometrical optic theory,which defines the wave ray as a curve tangential to wave number vectors. One then calculates the spatial variation of the wave envelope along the rays by involking the principle of conservation of energy flux,i.e., wave energy can only propagate along a ray tube formed by two adjacent wave rays. Numerical discretization can be done in steps along a ray not necessarily small in comparison with a typical wavelength . In the early 1960's the wave ray tracing method was a common tool for consulting engineers to estimate wave characteristics at a project site. Since the ray approximation does not allow wave energy flux across a wave ray, it fails near caustics or forcal regions, where neighboring wave rays intersect and diffract and possibly nonlinearity are important. While numrical methods for local remedies are available, it is not always convenient to implement them in practice.

(2) Mild-Slope Equation . With the framework of linear wave theory, an improvement to the ray approximation was first suggested by Eckart(1952) and was later rederived by Berkhoff(1972,1976), who proposed a tw-dimension theory that can deal with large regions of wave refraction and diffraction. The underlying

assumption of the theory is that evanescent modes are not important for waves propagating over a slowly varying bathymetry, except in the immediate vicinity of a three-dimensional obstacle. For a monochromatic wave with frequency ω and free surface displacement η, it is reasonable model only, as:

$$\phi = \frac{-ig\eta}{\omega}\frac{\cosh k(z+h)}{\cosh kh}e^{-i\omega t} \tag{1}$$

where $k(x,y)$ and $h(x,y)$ vary slowly in the horizontal direction, x and y,according to the linear frequency dispersion relation

$$\omega^2 = gk\tanh kh \tag{2}$$

and g is the gravitational acceleration. Using a perturbation argument, Smith and Sprinks(1975) have shown that the free surface displacement η must satify the following equation:

$$\nabla\cdot(CC_g\nabla\eta) + \frac{\omega^2}{g}\eta = 0 \tag{3}$$

where

$$C = \frac{\omega}{k}, C_g = \frac{d\omega}{dk} = \frac{C}{2}(1 + \frac{kh}{\sinh 2kh}) \tag{4}$$

are the local phase and group velocities of a plane progressive wave. The elliptic-type partial differential equation, (3), is asymptotically valid for sufficiently small $\delta(= |\nabla h|/kh$ to the leading order) and is known as the mild-slope equation. An indication of its versatility can be seen in two limits. For long waves in shallow water, the limit of (3) for $kh << 1$ reduces to the well-known linear shallow-water equation that is valid even if $\delta = O(1)$. On the other hand, if the depth is a constant or for short waves in deep water ($kh >> 1$), (3) reduces to the Helmholtz equation where k satisfies the dispersion relation (2). Both limits can be used to calculate diffraction legitimately. Thus, the mild slope-equation should be a good interpolation for all kh and is suitable for propagating wave from deep water to shallow water as long as the linearization is acceptable. A similar mild-slope equation for waves propagating over gradually varying currents has also been derived (e.g. Liu, 1990).

(3) Parabolic Approximation . In applying the mild-slope equation to a large coastal region, one encounters the difficulty of specifying appropriate boundary conditions along the shoreline, which are essential for solving the elliptic-type mild-slope equation. The difficulty arises because the location of the breaker cannot be determined a priori. A remedy to this problem is to apply the parabolic approximation to the mild-slope equation. For essentially forward propagation problems, the parabolic approximation expands the validity of the ray theory by allowing wave energy "diffuse" across the wave "ray". Therefore, the effects of diffraction

have been approximately included in the parabolic approximation. Although the parabolic approximation has been used primarily for forward propagation, adopting an iterative procedure can also include weakly backward propagation (e.g. Liu and Tsay 1983; Chen and Liu 1994).

(4) Stokes Waves. For finite amplitude waves, the usual linearizatin assumptions, which require that

$$kA << 1 \quad everywhere \quad and \quad A/h << 1 \quad in \quad shallow \quad water \quad (kh << 1) \tag{5}$$

might become invalid. A more relevant theory in the deep water and intermediate water is perhaps the higher-order Stokes wave theory that takes the effects of finite wave amplitude into consideration in the perturbation sense. The finiteness of the wave amplitude has direct effect on the frequency dispersion and consequently the phase speed. For instance, for the second-order Stokes wave, the nonlinear dispersion relation has the following form:

$$\omega^2 = gk \tanh kh + kA2 + ... \tag{6}$$

where

$$\kappa = \frac{k^4 C^2}{8 \sinh^4 kh}(8 + \cosh 4kh - 2\tanh^2 kh) \tag{7}$$

and A denotes the wave amplitude. Equation (6) can be viewed as a power series in terms of the small parameter $kA << 1$. The corresponding nonlinear mild-slope equation and its parabolic approximation have been derived and reported by Kirby and Dalrymple (1983) and Liu and Tsay (1984). However, one must exercise caution in extending the nonlinear Stokes wave theory into the shallow water. An additional condition needs to be satisfied. In the limit of $kh \rightarrow O$ the nonlinear dispersion relation can be approximated as:

$$\omega^2 = ghk^2(1 + \frac{9}{8}\frac{A/h}{k^2h^2}\frac{A}{h} + ...) \tag{8}$$

To ensure the series converges for $A/h << 1$, one must make sure that the coefficient of the second term in the series is of order one or smaller, i.e.,

$$U_r = O\left(\frac{A/h}{(kh)^2}\right) \leq O(1) \tag{9}$$

where U_r, is also called Ursell parameter. The condition (9), requiring the Ursell parameter to be of order one or smaller in the shallow water region, is very difficult to fulfill in practice. According to the linear theory, in shallow water the wave amplitude, A, grows proportional to $h^{-1/4}$ and kh decreases as $\sqrt{h}$. Therefore, the Ursell parameter will grow proportional to $h^{-9/4}$ as the water depth decreases and will certainly exceed order one at certain depth. One can conclude that the

nonlinear Stokes wave theory is not applicable in the shallow water and alternative model equations must be found.

(5) Boussinesq Approximation. Boussinesq-type equations provide a means for studying water wave propagation over a gradual varying bathymetry. The core of the Boussinesq-type equations is made of the shallow water equations for linear nondispersive wave propagation. This basic foundation is expanded by adding terms that represent effects of nonlinearity and frequency dispersion.

Asseming that both nonlinearity and frequency dispersion are weak and are in the same order of magnitude, Peregrine (1967) derived the standard Boussinesq equations for variable depth.

$$\eta_t + \nabla \cdot [(\eta + h)\overline{u}] = 0 \tag{10}$$

$$\overline{u}_t + \frac{1}{2}\nabla|\overline{u}|^2 + g\nabla\eta + \left\{\frac{h^2}{6}\nabla(\nabla\cdot\overline{u}_t) - \frac{h}{2}\nabla(\nabla(h\overline{u}_t))\right\} = 0 \tag{11}$$

in which$\overline{u}$ is the depth-averaged velocity, η the free surface displacement;h the still water depth, $\nabla = (\partial/\partial x, \partial/\partial y)$ the horizontal gradient operator, g the gravitational acceleration; and the subscript t the partial derivative with respect to time. Boussinesq equations can be cast into similar equations in terms of either the velocity on the bottom or he velocity on the free surface. While the dispersion relationship and the wave speed associated with these equations differ slightly, the order of magnitude of accuracy of these equations remains the same. Numerical results based on the standard Boussinesq equations or the equivalent formulations have compared quite well with field data (Elgar and Guza 1985 and laboratory data (Goring 1978, Liu et al. 1985).

The applications of the standard Boussinesq equations are limited to the shallow water depth because of the assumption of the weak frequency dispersion effects. The standard Boussinesq equations written in terms of the depth-averaged velocity break down when the depth is greater than one-fifth of the equivalent deep-water wavelength. For many engineering applications including harbor oscillation computations, where the incident wave energy spectrum consists of many frequency components, a lesser depth restriction is desirable. Furthermore, when the Boussinesq equations are solved numerically, high frequency oscillations with wavelengths related to the grid size could cause numerical instability. To extend the applications to shorter waves many modified forms of Boussinesq-type equations have been introduced (e.g. Madsen et al. 1991, Nwogu 1993, Beji and Nodaoka 1996, Chen and Liu 1995). Although the methods of derivation are different, the resulting dispersion relations of the linear components of these modified Boussinesq equations are similar, and may be viewed as a slight modification of the (2,2) Pade approximation of the full dispersion relation for linear water wave (Witting 1984). It has been demonstrated that the modified Boussinesq equations are able to simulate

wave propagation from deep water to shallow water including the wave-current interaction (Chen et al. 1998).

Despite of the success of the modified Boussinesq equations in intermediate and deep water, these equations are still restricted to weakly nonlinear interactions. As waves approach shore, wave height increases due to shoaling and wave breaks on most gentle natural beaches. The wave-height to water depth ratios associated with this physical process become too high for the Boussinesq approximation. Of course this restriction can be readily removed by eliminating the weak nonlinearity assumption (e.g., Wei et al. 1995). Strictly speaking, these strongly nonlinear equations can no longer be called Boussinesq-type equations since the nonlinearity is no longer in balance with the frequency dispersion, which is the spirit of the original Boussinesq assumption.

1.3 Wave Models

There are several existing numerical models which could be used with or without any modification to calculate the harbor oscillations. In this section only the models which have been designed specifically for studying the harbor oscillation problems and have been applied to field problems are briefly discussed. This brief review should also provide justifications for proposing a new numerical model.

(1) Finite element model based on the mild-slope equation. These models have been developed by several research groups with a similar approach (e.g. Chen, 1984, 1986, Tsay and Liu 1983, Kostense et al. 1986, Xu, et al. 1996). These are finite element models that calculate linear monochromatic wave oscillations in harbors of arbitrary configuration and variable bathymetry. The effects of bottom friction and boundary absorption (reflection) are included. These models use a hybrid element solution method which involves the combination of analytical (in offshore area) and finite element numerical (near and inside the harbor) solutions to determine the harbor response to a small amplitude wave with a single wave frequency. These models are the extension of the original model developed by Chen and Mei (1974), which was based on the linear shallow water equations.

Because of their simplicity these models have been used for assessing the design or modifications of existing harbors (e.g., Lillycrop et. al. 1993). However, the most serious drawback of the model is the limitation of the linear theory. The model can not be used to investigate harbor oscillations induced by nonlinear transient waves.

(2) Finite element model based on Boussinesq-type equations. Lepelletier (1980) developed a finite element model for solving the weakly nonlinear-dispersive-dissipative equations of motion for variable depth (also see Lepelletier and Raichlen 1987). Several dissipative effects such as bottom friction and entrance loss, were included in the model. The open sea conditions were simulated by using a time

varying radiation condition at a finite distance from the harbor entrance.

Since the Boussinesq approximation was employed in the model, the weakly nonlinear effects were included. However, the water depth must remain small relative to the wavelength throughout the entire domain of interest, including the offshore region. Therefore, this model is not suitable for studying the problems where the incident waves consist of short wave components. For example, in the Haw-lien harbor situation, the dominating wave outside of the harbor (ST 2) has a wavelength such that $kh \approx 1$ and cannot be considered as a shallow water wave. As discussed in the previous section, these short wave components are responsible for generating bound and free infragravity waves near and inside the harbor (e.g., Mei and Agnon 1989, Wu and Liu 1990), which might be reasonated in the harbor as possibly in the Haw-lien harbor case.

(3) Finite differences models based on Boussinesq-type equations. During the last twenty-five years scientists and engineers at the Danish Hydraulic Institute (DHI) have developed a series of finite differences models based on either the nonlinear shallow water equations or Boussinesq-type equations (e.g., Abbott 1979, Abbott, et al. 1978, Madsen, et al. 1991). These harbor models are components of a much larger system called MIKE 21 for studying the flow phenomena in estuaries and coastal waters. The disadvantages of these finite differences models are primarily due to the inflexibility of finite-difference methods in modeling the irregular boundaries as well as the complex bathymetrics. Furthermore, the MIKE 21 is a commercial package. It is impossible to obtain the source program for any further investigation and improvement.

From the brief review given above it is clear that existing harbor numerical models are limited by either the linear wave (mild-slope equation) or the shallow water depth assumption (Boussinesq-type equations). It is the objective of this proposed research to develop a finite element model, using the weakly nonlinear and weakly dispersive wave equations, to investigate the nonlinear transient harbor oscillations.

1.4 Objective and Scope of Present Study

During last year's research effort, based on the strongly nonlinear and weakly dispersive equations, an one-dimensional finite element model has been developed to calculate the transient, nonlinear wave propagation (Woo and Liu, 2000). The finite element model is based on the Petrov-Galerkin weighted residual method, in which the linear shape function and the cubic spline weighting function have been employed. The model has been successfully applied to several problems, including the shoaling of solitary wave, interactions of two solitons and the scattering of a nonlinear wave train by a submerged bar.

This year's research effort has been focused on the development of a two-dimensional model. Various approaches have been investigated. First, we have

considered the possibility of extension of the Petrov-Galerkin method used in the one-dimensional problem. It is straightforward to extend the Petrov-Galerkin FEM to a two-dimensional domain with non-uniform structured quadrilateral grids (Gardner and Gardner 1995). However, applying this method to unstructured grids needs careful consideration. Although it is possible to extend the Petrov-Galerkin approach to a two-dimensional domain with unstructured grids (Alfeld *et al.* 1987; Sabin 1997), the computational costs for mapping the C^1 type weighting function over a unstructured mesh will be quite expensive. It is concluded that the Petrov-Galerkin weighted residual method is not practical for two-dimensional problems, which, in general, require a unstructured finite element mesh. Instead, a Galerkin finite element is to be developed. With this approach, linear triangular or rectangular elements with linear shape functions are employed. Although one auxiliary variable must be introduced so as to deal with the third spatial derivative terms in the governing equations, the resulting algorithm is still more computationally efficient than the Petrov-Galerkin weighted residual method.

In this report, the two-dimensional governing equations are derived first. Some of the details of derivations are given for completeness. In section 3, based on the Galerkin method, the spatial discretization and the time integration scheme are discussed. Particularly, the choice of the auxiliary functions is also discussed. The input data file for the numerical model is presented in section 4. In section 5, several numerical examples are given, which demonstrate the accuracy of the proposed numerical scheme. In the appendix, the detailed information for the mass matrix, forcing vector and boundary vector for the matrix equation are p

2 Basic Equations for the Numerical Model

The objective of the research project is to develop a two-dimensional finite element model for computing transient, nonlinear harbor oscillations. The theoretical foundation of the proposed new model is based on the strongly nonlinear and weakly dispersive wave equations that can be applied in both intermediate and shallow water (e.g., Liu 1994, Wei et al. 1995). A brief derivation of these governing equations is given as follows.

The Stokes' wave theory breaks down when the Ursell number,

$$U_r = \frac{kA}{(kh)^3},$$

becomes an order one or larger quantity. This is often the case in shallow water in which kh becomes small. A different set of approximate governing equations need to be derived to describe the characteristics of long wave propagation in shallow water.

To facilitate discussions the following normalizations are introduced

$$x = \frac{x'}{\ell_0}, \quad y = \frac{y'}{\ell_0}, \quad z = \frac{z'}{h_0}, \quad t = \frac{\sqrt{gh_0}}{\ell_0}t', \quad h = \frac{h'}{h_0}, \tag{1}$$

in which ℓ_0 denotes the characteristic horizontal length scale such as the wave length, and h_0, the typical water depth. The time scale measures the time required for a long wave to travel a distance ℓ_0. Denoting a_0 as the characteristic wave amplitude and considering that the wave motion is irrotational, we can define the dimensionless free surface displacement η and velocity potential Φ as

$$\eta = \frac{\eta'}{a_0}, \quad \Phi = \frac{h_0}{a_0\ell_0\sqrt{gh_0}}\Phi'. \tag{2}$$

The dimensionless governing equation and boundary conditions can be written as:

$$\mu^2\nabla^2\Phi + \frac{\partial^2\Phi}{\partial z^2} = 0, \qquad -h < z < \varepsilon\eta, \tag{3}$$

$$\frac{\partial\Phi}{\partial z} = \mu^2\left(\frac{\partial\eta}{\partial t} + \varepsilon\nabla\Phi\cdot\nabla\eta\right), \qquad \text{on } z = \varepsilon\eta, \tag{4}$$

$$\frac{\partial\Phi}{\partial z} = -\mu^2\nabla\Phi\cdot\nabla h, \qquad \text{on } z = -h, \tag{5}$$

$$\left(\frac{\partial\Phi}{\partial t} + \eta\right) + \frac{\varepsilon}{2}\left[(\nabla\Phi)^2 + \frac{1}{\mu^2}\left(\frac{\partial\Phi}{\partial z}\right)^2\right] = 0, \qquad \text{on } z = \varepsilon\eta, \tag{6}$$

where $\nabla = (\partial/\partial x, \partial/\partial y)$ is the horizontal gradient and

$$\varepsilon = \frac{a_0}{h_0}, \tag{7}$$

$$\mu^2 = \left(\frac{h_0}{\ell_0}\right)^2, \tag{8}$$

measure the nonlinearity and the shallowness of the water, respectively. For long waves or very shallow water

$$O\left(\mu^2\right) \ll 1,$$

is usually assumed. If the nonlinearity is significant and $O(\varepsilon) \approx O(1)$, the Ursell number is certainly greater than one. However, if

$$O(\varepsilon) \approx O(\mu^2) \ll 1,$$

the Ursell number will be an order one quantity. This approximation is called Boussinesq approximation.

The objective of this derivation is to reduce the original three-dimensional problem to a two-dimensional problem on the x-y (horizontal) plane. To achieve this goal, one needs to find the distribution of the velocity potential in the vertical z-direction. To illustrate this point, we integrate the Laplace equation (3) from $z = -h$ to $z = \varepsilon\eta$ to get

$$\mu^2 \int_{-h}^{\varepsilon\eta} \nabla^2\Phi dz + \int_{-h}^{\varepsilon\eta} \frac{\partial^2\Phi}{\partial z^2} dz = 0.$$

If we rewrite $\nabla^2\Phi = \nabla \cdot (\nabla\Phi)$ and apply the Leibniz rule to the first integral, the above equation can be expressed as

$$\mu^2 \nabla \cdot \int_{-h}^{\varepsilon\eta} \nabla\Phi \, dz - \left\{\mu^2 \varepsilon \nabla\eta \cdot \nabla\Phi - \frac{\partial\Phi}{\partial z}\right\}\Bigg|_{z=\varepsilon\eta}$$

$$- \left\{\frac{\partial\Phi}{\partial z} + \mu^2 \nabla\Phi \cdot \nabla h\right\}\Bigg|_{z=-h} = 0.$$

Using the boundary condition (4) and (5) in the above equation yields

$$\nabla \cdot \int_{-h}^{\varepsilon\eta} \nabla\Phi \, dz + \frac{\partial\eta}{\partial t} = 0. \tag{9}$$

The resulting equation is exact and independent of the vertical coordinate z. We may define a depth averaged horizontal velocity vector

$$\bar{\mathbf{u}} = \frac{1}{h+\varepsilon\eta}\int_{-h}^{\varepsilon\eta} \nabla\Phi \, dz. \tag{10}$$

Equation (9) becomes

$$\frac{\partial\eta}{\partial t} + \nabla\cdot\left[(\varepsilon\eta + h)\,\bar{\mathbf{u}}\right] = 0, \tag{11}$$

which is the exact continuity equation for a vertical column of fluid with a unit cross-sectional area. To solve for the free surface displacement η and the depth averaged velocity $\bar{\mathbf{u}}$, one needs to derive another equation. This will be done with a formal perturbation technique in the following section.

For long waves or waves in a very shallow water, the parameter μ^2 is assumed to be small. However, the parameter representing nonlinearity, ε, remains an order one quantity. The following perturbation solutions are sought.

$$\Phi(x,y,z,t) = \sum_{n=0}^{\infty} \mu^{2n}\Phi_n(x,y,z,t). \tag{12}$$

Only the even powers of μ are included in the solution form, since only the parameter μ^2 appears in the governing equation and boundary conditions, (2). Substituting the solution form, (12), into the Laplace equation (3) and bottom boundary condition (5) and collecting the first two orders yield:

$O(1)$:

$$\frac{\partial^2\Phi_0}{\partial z^2} = 0, \qquad -h < z < \varepsilon\eta, \tag{13}$$

$$\frac{\partial\Phi_0}{\partial z} = 0, \qquad z = -h, \tag{14}$$

$O(\mu^2)$:

$$\frac{\partial^2\Phi_1}{\partial z^2} = -\nabla^2\Phi_0, \qquad -h < z < \varepsilon\eta, \tag{15}$$

$$\frac{\partial\Phi_1}{\partial z} = -\nabla\Phi_0\cdot\nabla h, \qquad z = -h. \tag{16}$$

From (13) and (14), the leading-order solution, Φ_0, is independent of the vertical coordinate. Thus, we can define

$$\Phi_0 = \phi_{00}(x,y,t), \tag{17}$$

which also implies that the leading order vertical velocity component vanishes.

From the $O(\mu^2)$ problem, (2), we can integrate the continuity equation twice to obtain

$$\Phi_1(x,y,z,t) = \phi_{10}(x,y,t) + z\,\phi_{11}(x,y,t) - \frac{z^2}{2}\nabla^2\phi_{00}.$$

Substituting the above equation into the bottom boundary condition, (14), yields

$$\phi_{11} = -\nabla\cdot(h\nabla\phi_{00}).$$

Consequently

$$\Phi_1 = \phi_{10}(x,y,t) - z\nabla\cdot(h\nabla\phi_{00}) - \frac{z^2}{2}\nabla^2\phi_{00}, \tag{18}$$

$$\frac{\partial\Phi_1}{\partial z} = -\nabla\cdot(h\nabla\phi_{00}) - z\nabla^2\phi_{00}. \tag{19}$$

The second-order horizontal velocity, $\nabla\Phi_1$, is a quadratic function in z, while the vertical velocity is a linear function in z.

Up to the second-order in μ, the potential function can be summarized as

$$\Phi(x,y,z,t) = \phi_{00} + \mu^2\left[\phi_{10} - z\nabla\cdot(h\nabla\phi_{00}) - \frac{z^2}{2}\nabla^2\phi_{00}\right] + O\left(\mu^2\right), \tag{20}$$

in which both ϕ_{00} and ϕ_{10} are unknown and are to be determined from the free surface boundary conditions. We can also express (20) in terms of the potential function on a specified surface $z = z_\alpha(x,y)$. Denoting

$$\Phi_\alpha(x,y,t) = \Phi(x,y,z_\alpha(x,y),t),$$

From (20) we obtain

$$\Phi_\alpha(x,y,t) = \phi_{00} + \mu^2\left[\phi_{10} - z_\alpha\nabla\cdot(h\nabla\phi_{00}) - \frac{z_\alpha^2}{2}\nabla^2\phi_{00}\right] + O(\mu^4). \tag{21}$$

Substituting (20) into (21) yields

$$\Phi(x,y,z,t) = \Phi_\alpha + \mu^2\left[(z_\alpha - z)\,\nabla\cdot(h\nabla\phi_{00}) + \frac{1}{2}\left(z_\alpha^2 - z^2\right)\nabla^2\phi_{00}\right] + O(\mu^4).$$

Because $\Phi_\alpha = \phi_{00} + O(\mu^2)$, the above equation can be written in terms of Φ_α as

$$\Phi(x,y,z,t) = \Phi_\alpha + \mu^2\left[(z_\alpha - z)\nabla\cdot(h\nabla\Phi_\alpha) + \frac{1}{2}\left(z_\alpha^2 - z^2\right)\nabla^2\Phi_\alpha\right] + O(\mu^4). \tag{22}$$

It is noted here that $z_\alpha(x,y)$ is a given surface. A special case is that $z_\alpha(x,y) = -h(x,y)$. The corresponding velocity potential Φ_α describes the potential along the seafloor.

Substituting (22) into the continuity equation (9), we get an approximate continuity equation

$$\begin{aligned}\frac{\partial \eta}{\partial t} \quad & +\nabla\cdot[(\varepsilon\eta+h)\nabla\Phi_\alpha] + \mu^2\nabla\cdot\left\{(\varepsilon\eta+h)\nabla\left[z_\alpha\left(\nabla\cdot h\nabla\Phi_\alpha\right)+\frac{1}{2}z_\alpha^2\nabla^2\Phi_\alpha\right]\right. \\ & \left.-\frac{1}{2}\left(\varepsilon^2\eta^2-h^2\right)\nabla\left(\nabla\cdot h\nabla\Phi_\alpha\right)-\frac{1}{6}\left(\varepsilon^3\eta^3+h^3\right)\nabla\left(\nabla^2\Phi_\alpha\right)\right\} = O(\mu^4). \quad (23)\end{aligned}$$

It is reiterated that the nonlinearity parameter ε is treated as an order one quantity in the above equation.

Substitution of (22) into the dynamic boundary condition, (5), yields

$$\begin{aligned}\frac{\partial \Phi_\alpha}{\partial t} \quad & +\eta+\frac{\varepsilon}{2}\left(\nabla\Phi_\alpha\right)^2+\mu^2\left\{\left(z_\alpha-\varepsilon\eta\right)\nabla\cdot\left(h\nabla\frac{\partial\Phi_\alpha}{\partial t}\right)+\frac{1}{2}\left(z_\alpha^2-\varepsilon^2\eta^2\right)\nabla^2\frac{\partial\Phi_\alpha}{\partial t}\right. \\ & +\varepsilon\nabla\Phi_\alpha\cdot\nabla\left[\left(z_\alpha-\varepsilon\eta\right)\nabla\cdot\left(h\nabla\Phi_\alpha\right)+\frac{1}{2}\left(z_\alpha^2-\varepsilon^2\eta^2\right)\nabla^2\Phi_\alpha\right] \\ & \left.+\frac{\varepsilon}{2}\left[\nabla\cdot\left(h\nabla\Phi_\alpha\right)+\varepsilon\eta\nabla^2\Phi_\alpha\right]^2\right\} = O(\mu^4). \quad (24)\end{aligned}$$

Equations (23) and (24) constitute governing equations for the free surface displacement η and the velocity potential Φ_α. Once they are found, the velocity potential for the entire flow field can be obtained from (22). Usually, it is more convenient to express the governing equations in terms of a velocity quantity instead of the velocity potential. Thus, we define the horizontal velocity along $z = z_\alpha(x,y)$ as

$$\begin{aligned}\mathbf{u}_\alpha \quad & = (\nabla\Phi)|_{z=z_\alpha} \\ & = \nabla\Phi_\alpha+\mu^2\left[\nabla z_\alpha\nabla\cdot\left(h\nabla\Phi_\alpha\right)+z_\alpha\nabla z_\alpha\nabla^2\Phi_\alpha\right]+O(\mu^4), \quad (25)\end{aligned}$$

i.e.

$$\nabla\Phi_\alpha = \mathbf{u}_\alpha-\mu^2\left[\nabla z_\alpha\nabla\cdot\left(h\mathbf{u}_\alpha\right)+z_\alpha\nabla z_\alpha\nabla\cdot\mathbf{u}_\alpha\right]+O(\mu^4), \quad (26)$$

for $\nabla\Phi_\alpha = \mathbf{u}_\alpha + O(\mu^2)$. Substituting (26) into the continuity equation (23) yield

$$\begin{aligned}\frac{\partial\eta}{\partial t} \quad & +\nabla\cdot[(\varepsilon\eta+h)\mathbf{u}_\alpha]+\mu^2\nabla\cdot\left\{\left(\frac{z_\alpha^2}{2}-\frac{h^3}{6}\right)h\nabla(\nabla\cdot\mathbf{u}) \right. \\ & \left.+\left(z_\alpha+\frac{h}{2}\right)h\nabla\left[\nabla\cdot\left(h\mathbf{u}_\alpha\right)\right]\right\}+\mu^2\varepsilon\nabla\cdot\left\{\eta\left[\left(z_\alpha-\frac{1}{2}\varepsilon\eta\right)\nabla\left(\nabla\cdot h\mathbf{u}_\alpha\right)\right.\right. \\ & \left.\left.+\frac{1}{2}\left(z_\alpha^2-\frac{1}{3}\varepsilon^2\eta^2\right)\nabla(\nabla\cdot\mathbf{u}_\alpha)\right]\right\} = O(\mu^4). \quad (27)\end{aligned}$$

Taking the horizontal gradient of (24) and substituting (26) into the resulting equation, we obtain

$$\begin{aligned}\frac{\partial \mathbf{u}_\alpha}{\partial t} \quad & +\nabla\eta+\frac{\varepsilon}{2}\nabla|\mathbf{u}_\alpha|^2+\mu^2\left\{z_\alpha\nabla\left[\nabla\cdot\left(h\frac{\partial \mathbf{u}_\alpha}{\partial t}\right)\right]+\frac{1}{2}z_\alpha^2\nabla\left(\nabla\cdot\frac{\partial \mathbf{u}_\alpha}{\partial t}\right)\right\}\\ & +\mu^2\varepsilon\nabla\left\{\frac{1}{2}z_\alpha^2\mathbf{u}_\alpha\cdot\nabla(\nabla\cdot\mathbf{u}_\alpha)+z_\alpha\mathbf{u}\cdot\nabla(\nabla\cdot h\mathbf{u}_\alpha)\right.\\ & \left.+\frac{1}{2}\left[\nabla\cdot(h\mathbf{u}_\alpha)\right]^2-\eta\nabla\cdot\left(h\frac{\partial \mathbf{u}_\alpha}{\partial t}\right)\right\}\\ & +\mu^2\varepsilon^2\nabla\left\{\eta(\nabla\cdot h\mathbf{u}_\alpha)(\nabla\cdot\mathbf{u}_\alpha)-\frac{\eta^2}{2}\nabla\cdot\left(\frac{\partial \mathbf{u}_\alpha}{\partial t}\right)-\mathbf{u}_\alpha\cdot\nabla\left[\eta\nabla\cdot(h\mathbf{u}_\alpha)\right]\right\}\\ & +\mu^2\varepsilon^3\nabla\left\{\frac{1}{2}\eta^2(\nabla\cdot\mathbf{u}_\alpha)^2-\mathbf{u}_\alpha\cdot\nabla\left(\frac{1}{2}\eta^2\nabla\cdot\mathbf{u}_\alpha\right)\right\}=O(\mu^4).\end{aligned}\tag{28}$$

Once again (27) and (28) are the governing equations for η and $\mathbf{u}_\alpha$ for arbitrary ε.

For many situations the nonlinearity and the frequency dispersion are equally important. In other words

$$O(\varepsilon)\approx O(\mu^2)\ll 1.\tag{29}$$

The general long wave equations (27) and (28) can be simplified as

$$\begin{aligned}\frac{\partial \eta}{\partial t} \quad & +\nabla\cdot\left[(\varepsilon\eta+h)\mathbf{u}_\alpha\right]+\mu^2\nabla\cdot\left\{\left(\frac{z_\alpha^2}{2}-\frac{h^2}{6}\right)h\nabla(\nabla\cdot\mathbf{u})\right.\\ & \left.+\left(z_\alpha+\frac{h}{2}\right)h\,\nabla\left[\nabla\cdot(h\mathbf{u}_\alpha)\right]\right\}=O(\mu^2\varepsilon,\mu^4),\end{aligned}\tag{30}$$

$$\begin{aligned}\frac{\partial \mathbf{u}_\alpha}{\partial t} \quad & +\nabla\eta+\frac{\varepsilon}{2}\nabla|\mathbf{u}_\alpha|^2+\mu^2\left\{z_\alpha\nabla\left[\nabla\cdot\left(h\frac{\partial \mathbf{u}_\alpha}{\partial t}\right)\right]\right.\\ & \left.+\frac{1}{2}z_\alpha^2\nabla\left(\nabla\cdot\frac{\partial \mathbf{u}_\alpha}{\partial t}\right)\right\}=O(\mu^2\varepsilon,\mu^4).\end{aligned}\tag{31}$$

These equations are called Boussinesq equations for weakly nonlinear and dispersive long waves. Several different forms of the Boussinesq equations can be obtained by specifying $z_\alpha(x,y)$. For instance, if $z_\alpha=0$, the horizontal velocity vector, $\mathbf{u}_\alpha=\mathbf{u}_0$, is evaluated on the still water surface, $z=z_\alpha=0$. The corresponding Boussinesq equations become

$$\begin{aligned}\frac{\partial \eta}{\partial t} \quad & +\nabla\cdot\left[(\varepsilon\eta+h)\mathbf{u}_0\right]+\mu^2\nabla\cdot\left\{\frac{h^2}{2}\nabla\left[\nabla\cdot(h\mathbf{u}_0)\right]\right.\\ & \left.-\frac{h^3}{6}\nabla(\nabla\cdot\mathbf{u}_0)\right\}=O(\mu^2\varepsilon,\mu^4),\end{aligned}\tag{32}$$

$$\frac{\partial \mathbf{u}_0}{\partial t} + \nabla\eta + \frac{\varepsilon}{2}\nabla|\mathbf{u}_0|^2 = O(\mu^2\varepsilon, u^4). \tag{33}$$

On the other hand, if $z_\alpha = -h$, the horizontal velocity vector $\mathbf{u}_\alpha = \mathbf{u}_b$ is the horizontal velocity along the seafloor. The Boussinesq equations take the following form

$$\begin{aligned}\frac{\partial \eta}{\partial t} \quad & +\nabla\cdot\{(\varepsilon\eta + h)\mathbf{u}_b] + \mu^2\nabla\cdot\left(\frac{h^3}{3}\nabla(\nabla\cdot\mathbf{u}_b)\right. \\ & \left.-\frac{h^2}{2}\left[\nabla\cdot(h\mathbf{u}_b)\right]\right\} = O(\mu^2\varepsilon, \mu^4),\end{aligned} \tag{34}$$

$$\begin{aligned}\frac{\partial \mathbf{u}_b}{\partial t} \quad & +\nabla\eta + \frac{\varepsilon}{2}\nabla|\mathbf{u}_b|^2 + \mu^2\left\{h^2\nabla\left(\nabla\cdot\frac{\partial \mathbf{u}_b}{\partial t}\right)\right. \\ & \left.-h\nabla\left[\nabla\cdot\left(h\frac{\partial \mathbf{u}_b}{\partial t}\right)\right]\right\} = O(\mu^2\varepsilon, \mu^4).\end{aligned} \tag{35}$$

Another commonly seen form of Boussinesq equations is presented in terms of the depth averaged horizontal velocity defined in (10). To convert the general Boussinesq equation form, we need to find the relation between $\mathbf{u}_\alpha$ and $\bar{\mathbf{u}}$ first. Substituting (22) into (10) yields

$$\begin{aligned}\bar{\mathbf{u}} = \quad & \mathbf{u}_\alpha + \mu^2\left\{\left(\frac{h}{2} + z_\alpha\right)\nabla\left[\nabla\cdot(h\mathbf{u}_\alpha)\right]\right. \\ & \left.+\left(\frac{z_\alpha^2}{2} - \frac{h^2}{6}\right)\nabla(\nabla\cdot\mathbf{u}_\alpha)\right\} + O(\mu^2\varepsilon, \mu^4),\end{aligned} \tag{36}$$

in which (25) has been used. Substituting the equation above into (30) and (31), we obtain

$$\frac{\partial \eta}{\partial t} + \nabla\cdot[(\varepsilon\eta + h)\bar{\mathbf{u}}] = 0, \tag{37}$$

$$\begin{aligned}\frac{\partial \bar{\mathbf{u}}}{\partial t} \quad & +\nabla\eta + \frac{1}{2}\varepsilon\nabla|\bar{\mathbf{u}}|^2 + \mu^4\left\{\frac{h^2}{6}\nabla\left(\nabla\cdot\frac{\partial \bar{\mathbf{u}}}{\partial t}\right)\right. \\ & \left.-\frac{h}{2}\nabla\left[\nabla\cdot\left(h\frac{\partial \bar{\mathbf{u}}}{\partial t}\right)\right]\right\} = O(\mu^2\varepsilon, \mu^4).\end{aligned} \tag{38}$$

It is noted here that the continuity equation (37) is exact in terms of the depth-averaged velocity as shown in (11).

All these Boussinesq equations have the same accuracy, namely the truncation errors are $O(\mu^2\varepsilon, \mu^4)$. More different forms can be generated by replacing the higher terms, $O(\mu^2)$, by a lower order relationship. For example, in all the momentum equations the time derivative of the velocity vector can be replaced by the negative of the horizontal gradient of the free surface displacement without affecting the accuracy of the resulting equation. However, the dispersion relationships for each set of the equations are quite different and will change the range of applicability of these equations in terms of μ^2.

To examine the linear dispersion relationship for different forms of Boussinesq equations, we consider the constant depth case. The linearized form of the Boussinesq equations (30) and (31) become

$$\frac{\partial \eta}{\partial t} + h\nabla \cdot \mathbf{u}_\alpha + \mu^2 \left(\alpha + \frac{1}{3}\right) h^3 \nabla^2 (\nabla \cdot \mathbf{u}_\alpha) = 0, \tag{39}$$

$$\frac{\partial \mathbf{u}_\alpha}{\partial t} + \nabla \eta + \mu^2 \alpha h^2 \nabla \left(\nabla \cdot \frac{\partial \mathbf{u}_\alpha}{\partial t}\right) = 0, \tag{40}$$

in which

$$\alpha = \frac{1}{2}\left(\frac{z_\alpha}{h}\right)^2 + \frac{z_\alpha}{h}, \tag{41}$$

and z_α has been assumed to be a constant. If $z_\alpha = 0, \alpha = 0; z_\alpha = -h, \alpha = -0.5$.

Consider a small amplitude progression wave propagating on the x-direction

$$\eta = a_0 \exp[i(kx - \omega t)], \tag{42}$$

$$u_\alpha = b_0 \exp[i(kx - \omega t)], \tag{43}$$

in which a_0 and b_0 are constants. Substituting the equations above into the governing equations, we obtain

$$\begin{bmatrix} -i\omega & +ikh - i\mu^2\left(\alpha + \frac{1}{3}\right)k^3h^3 \\ ik & -i\omega + i\mu^2\alpha k^2h^2\omega \end{bmatrix} \begin{Bmatrix} a_0 \\ b_0 \end{Bmatrix} = 0, \tag{44}$$

which is a system of homogeneous equations for a_0 and b_0. To ensure nontrivial solutions for a_0 and b_0, the determinant of the above equation must vanish, i.e.

$$\omega^2(1 - \alpha\mu^2k^2h^2) - k^2h\left[1 - \left(\alpha + \frac{1}{3}\right)\mu^2k^2h^2\right] = 0,$$

or

$$\frac{\omega^2}{k^2} = C^2 = \left[\frac{1 - \left(\alpha + \frac{1}{3}\right)\mu^2k^2h^2}{1 - \alpha\mu^2k^2h^2}\right] h, \tag{45}$$

which gives the phase speed. When the right-hand is negative either ω or k becomes an imaginary constant. Hence, the system grows either in time or in space. For instance, when $\alpha = 0$

$$C^2 = \left[1 - \frac{1}{3}\mu^2 k^2 h^2\right] h. \tag{46}$$

This represents the dispersion relationship for the linearized Boussinesq equation when the horizontal velocity on the still water level is used in the equation. This system becomes unstable when

$$\mu k h > \sqrt{3}, \tag{47}$$

which could happen only for very short waves. For $\alpha = -0.5$,

$$C^2 = \frac{1 + \frac{1}{6}\mu^2 k^2 h^2}{1 + \frac{1}{2}\mu^2 k^2 h^2}, \tag{48}$$

which is always positive. Therefore, the Boussinesq equations, written in terms of the horizontal velocity along the seafloor, have a better characteristic for instability.

The governing equations, (27) and (28), can be expressed in the following concise forms (Liu 1994; Wei et al. 1995)

$$\frac{\partial \eta}{\partial t} + \nabla \cdot \mathbf{M} = 0 \tag{49}$$

$$\frac{\partial \mathbf{u}_\alpha}{\partial t} + \varepsilon \left(\mathbf{u}_\alpha \cdot \nabla\right) \mathbf{u}_\alpha + \nabla \eta + \mu^2 \mathbf{V_1} + \varepsilon \mu^2 \mathbf{V_2} = \mathbf{O}\left(\mu^4\right) \tag{50}$$

in which

$$\mathbf{M} = \mathbf{M_1} + \mathbf{M_2} \tag{51}$$

$$\mathbf{M_1} = (h + \varepsilon\eta)\, \mathbf{u}_\alpha \tag{52}$$

$$\begin{aligned} \mathbf{M_2} = \mu^2 (h + \varepsilon\eta) \Bigg\{ & \left[\frac{1}{2} z_\alpha^2 - \frac{1}{6}\left(h^2 - \varepsilon\eta h + (\varepsilon\eta)^2\right)\right] \nabla \left(\nabla \cdot \mathbf{u}_\alpha\right) \\ & + \left[z_\alpha + \frac{1}{2}(h - \varepsilon\eta)\right] \nabla \left(\nabla \cdot (h\mathbf{u}_\alpha)\right) \Bigg\} + 0\left(\mu^4\right) \end{aligned} \tag{53}$$

$$\begin{aligned} \mathbf{V_1} = & \frac{1}{2} z_\alpha^2 \nabla \left(\nabla \cdot \frac{\partial \mathbf{u}_\alpha}{\partial t}\right) + z_\alpha \nabla \left(\nabla \cdot \left(h \frac{\partial \mathbf{u}_\alpha}{\partial t}\right)\right) \\ & - \nabla \left[\frac{1}{2} (\varepsilon\eta)^2 \nabla \cdot \left(\frac{\partial \mathbf{u}_\alpha}{\partial t}\right) + \varepsilon\eta \nabla \cdot \left(h \frac{\partial \mathbf{u}_\alpha}{\partial t}\right)\right] \end{aligned} \tag{54}$$

$$\mathbf{V_2} = \nabla \left[(z_\alpha - \varepsilon\eta) (\mathbf{u}_\alpha \cdot \nabla) (\nabla \cdot h\mathbf{u}_\alpha) + \frac{1}{2} \left(z_\alpha^2 - (\varepsilon\eta)^2 \right) (\mathbf{u}_\alpha \cdot \nabla) (\nabla \cdot \mathbf{u}_\alpha) \right.$$

$$\left. + \frac{1}{2} (\nabla \cdot (h\mathbf{u}_\alpha) + \varepsilon\eta \, \nabla \cdot \mathbf{u}_\alpha)^2 \right] \tag{55}$$

These equations are suitable for modeling finite amplitude waves with weakly dispersive effects. By improving the linear dispersion characteristics of these equations with an appropriate choice of z_α value, these equations can be used in the intermediate depth (e.g., Nwogu 1993, Chen and Liu 1995). For instance, Chen and Liu (1995) suggested that the best value for z_α should be approximately -0.52 h. We should point out that by including the higher order frequency dispersive effects and the nonlinear effects the third order spatial derivatives are introduced in the conservation of mass, $\nabla \cdot \mathbf{M_2}$, and the momentum equation, $\varepsilon\mu^2\mathbf{V_2}$, respectively. Special attention needs to be focused on the treatment of these third derivative terms in the development of numerical algorithms.

Once the horizontal velocity vector $\mathbf{u}_\alpha$ is obtained, the vertical profiles of velocity components can be expressed as

$$\mathbf{u} = \mathbf{u}_\alpha + \mu^2 \left\{ (z_\alpha - z) \nabla [\nabla \cdot (h\mathbf{u}_\alpha)] + \frac{1}{2} \left(z_\alpha^2 - z^2 \right) \nabla (\nabla \cdot \mathbf{u}_\alpha) \right\} + O(\mu^4) \tag{56}$$

$$w = -\mu^2 [\nabla \cdot (h\mathbf{u}_\alpha) + z\nabla \cdot \mathbf{u}_\alpha] + O(\mu^4) \tag{57}$$

in which w is the vertical velocity component.

2.1 Two-dimensional Governing Equations for weakly nonlinear and weakly dispersive waves

In this report, only weakly nonlinear problems will be discussed in detail. If the assumption of $O(\varepsilon) \simeq O(\mu^2) \leq 1$ is applied in (49) - (55), the governing equations are reduced to modified Boussinesq equations as follows:

$$\frac{\partial \eta}{\partial t} + \nabla \cdot [(h + \varepsilon\eta)\mathbf{u}_\alpha] + \mu^2 \nabla \cdot [C_1 h^3 \nabla(\nabla \cdot \mathbf{u}_\alpha) + C_3 h^2 \nabla(\nabla \cdot (h\mathbf{u}_\alpha))] = 0 \tag{58}$$

$$\frac{\partial \mathbf{u}_\alpha}{\partial t} + \nabla\eta + \frac{\varepsilon}{2} \nabla(\mathbf{u}_\alpha \cdot \mathbf{u}_\alpha) + \mu^2 \left[C_2 h^2 \nabla \left(\nabla \cdot \frac{\partial \mathbf{u}_\alpha}{\partial t} \right) + \beta h \nabla \left(\nabla \cdot \left(h \frac{\partial \mathbf{u}_\alpha}{\partial t} \right) \right) \right] = 0 \tag{59}$$

in which

$$C_1 = \frac{1}{2} \left(\beta^2 - \frac{1}{3} \right), \; C_2 = \frac{\beta^2}{2}, \; C_3 = \beta + \frac{1}{2}, \; \beta = \frac{z_\alpha}{h} \tag{60}$$

Note that the third order spatial derivative terms appear in the continuity equation, but not in the momentum equations. Due to the presence of the third order spatial

derivative, the linear Galerkin finite element cannot be applied directly. To reduce the order of highest spatial derivative, auxiliary variables are introduced, i.e.,

$$P := \nabla \cdot \mathbf{u}_\alpha, \quad R_1 := \frac{\partial^2 h}{\partial x^2}, \quad R_2 := \frac{\partial^2 h}{\partial y^2}, \quad R_3 := \frac{\partial^2 h}{\partial x \partial y} \tag{61}$$

With these new variables the governing equations can be rewritten in a lower order form as follows:

$$\begin{aligned}
\dot{\eta} \;+\; & \frac{\partial}{\partial x}\left[(h+\varepsilon\eta)u_\alpha\right] + \frac{\partial}{\partial y}\left[(h+\varepsilon\eta)v_\alpha\right] \\
+\; & \mu^2 \frac{\partial}{\partial x}\left[C_1 h^3 \frac{\partial P}{\partial x} + C_3 h^2 \left(\frac{\partial (hP)}{\partial x} + \frac{\partial u_\alpha}{\partial x}\frac{\partial h}{\partial x} + u_\alpha R_1 + \frac{\partial v_\alpha}{\partial x}\frac{\partial h}{\partial y} + v_\alpha R_3\right)\right] \\
+\; & \mu^2 \frac{\partial}{\partial y}\left[C_1 h^3 \frac{\partial P}{\partial y} + C_3 h^2 \left(\frac{\partial (hP)}{\partial y} + \frac{\partial u_\alpha}{\partial y}\frac{\partial h}{\partial x} + u_\alpha R_3 + \frac{\partial v_\alpha}{\partial y}\frac{\partial h}{\partial y} + v_\alpha R_2\right)\right] \\
=\; & 0
\end{aligned} \tag{62}$$

$$\begin{aligned}
\dot{u}_\alpha \;+\; & \mu^2 \left[C_2 h^2 \frac{\partial^2 \dot{u}_\alpha}{\partial x^2} + \beta h \frac{\partial^2 (h\dot{u}_\alpha)}{\partial x^2}\right] \\
+\; & \frac{\partial}{\partial x}\left[\eta + \varepsilon\frac{1}{2}(u_\alpha^2 + v_\alpha^2) + \mu^2 \left\{C_2 h^2 \frac{\partial \dot{v}_\alpha}{\partial y} + \beta h \frac{\partial (h\dot{v}_\alpha)}{\partial y}\right\}\right] = 0
\end{aligned} \tag{63}$$

$$\begin{aligned}
\dot{v}_\alpha \;+\; & \mu^2 \left[C_2 h^2 \frac{\partial^2 \dot{v}_\alpha}{\partial y^2} + \beta h \frac{\partial^2 (h\dot{v}_\alpha)}{\partial y^2}\right] \\
+\; & \frac{\partial}{\partial y}\left[\eta + \varepsilon\frac{1}{2}(u_\alpha^2 + v_\alpha^2) + \mu^2 \left\{C_2 h^2 \frac{\partial \dot{u}_\alpha}{\partial x} + \beta h \frac{\partial (h\dot{u}_\alpha)}{\partial x}\right\}\right] = 0
\end{aligned} \tag{64}$$

$$P - \frac{\partial u_\alpha}{\partial x} - \frac{\partial v_\alpha}{\partial y} = 0 \tag{65}$$

in which the overdot denotes the partial differentiation with respect to time. Note that the highest spatial derivative in the governing equation is second order at the expense of introducing one additional differential equation into the system. R_1, R_2, and R_3 will be calculated from the bathymetry data once before the time integration procedure begins, since R_1 and R_2 are invariant in time. The treatment of $\dot{v}_\alpha$ in equation (63) and $\dot{u}_\alpha$ in equation (64) will be explained in detail at the time integration section.

3 Numerical Schemes

The major effort of proposed research is to develop an efficient and accurate finite element model to solve the governing equations (58) and (59) with a variable depth and an irregular domain. The proper choice of spatial approximation scheme and time integration scheme will be discussed carefully and will be the main focus of attention for the present research.

3.1 Spatial Approximation Schemes

3.1.1 Galerkin finite element method

For the development of the Galerkin finite element method, the weighted residuals of the governing equations are required to be zero, i.e., equations (62), (63), (64) and (65) are multiplied by a weighting function $W(x,y)$ and integrated over the spatial domain Ω. Then the weak form of the governing equations is constructed by performing integration by parts and introducing integrals on the boundary Γ.

$$
\begin{aligned}
&\iint_\Omega W\dot{\eta}\, dxdy \\
&= \iint_\Omega \left\{ \frac{\partial W}{\partial x}\left[(h+\varepsilon\eta)u_\alpha + \mu^2\left(C_1h^3\frac{\partial P}{\partial x}\right.\right.\right. \\
&\qquad \left.\left.\left. +C_3h^2\left(\frac{\partial(hP)}{\partial x}+\frac{\partial u_\alpha}{\partial x}\frac{\partial h}{\partial x}+u_\alpha R_1+\frac{\partial v_\alpha}{\partial x}\frac{\partial h}{\partial y}+v_\alpha R_3\right)\right)\right] \right. \\
&\quad \left. +\frac{\partial W}{\partial y}\left[(h+\varepsilon\eta)v_\alpha + \mu^2\left(C_1h^3\frac{\partial P}{\partial y}\right.\right.\right. \\
&\qquad \left.\left.\left. +C_3h^2\left(\frac{\partial(hP)}{\partial y}+\frac{\partial u_\alpha}{\partial y}\frac{\partial h}{\partial x}+u_\alpha R_3+\frac{\partial v_\alpha}{\partial y}\frac{\partial h}{\partial y}+v_\alpha R_2\right)\right)\right] \right\} dxdy \\
&- \int_\Gamma \left\{ n_x W\left[(h+\varepsilon\eta)u_\alpha + \mu^2\left(C_1h^3\frac{\partial P}{\partial x}\right.\right.\right. \\
&\qquad \left.\left.\left. +C_3h^2\left(\frac{\partial(hP)}{\partial x}+\frac{\partial u_\alpha}{\partial x}\frac{\partial h}{\partial x}+u_\alpha R_1+\frac{\partial v_\alpha}{\partial x}\frac{\partial h}{\partial y}+v_\alpha R_3\right)\right)\right] \right. \\
&\quad \left. +n_y W\left[(h+\varepsilon\eta)v_\alpha + \mu^2\left(C_1h^3\frac{\partial P}{\partial y}\right.\right.\right. \\
&\qquad \left.\left.\left. +C_3h^2\left(\frac{\partial(hP)}{\partial y}+\frac{\partial u_\alpha}{\partial y}\frac{\partial h}{\partial x}+u_\alpha R_3+\frac{\partial v_\alpha}{\partial y}\frac{\partial h}{\partial y}+v_\alpha R_2\right)\right)\right] \right\} d\Gamma
\end{aligned}
\tag{66}
$$

$$\iint_\Omega \left\{ W - \mu^2 \left[W \left(C_4 \frac{\partial h^2}{\partial x}\frac{\partial}{\partial x} + \beta \left(\frac{\partial h}{\partial x} \right)^2 \right) + \frac{\partial W}{\partial x} \left(C_5 h^2 \frac{\partial}{\partial x} + \frac{\beta}{2}\frac{\partial h^2}{\partial x} \right) \right] \right\} \dot{u}_\alpha dxdy$$
$$= \iint_\Omega \Bigg\{ \mu^2 W \left[C_2 \frac{\partial h^2}{\partial x}\frac{\partial \dot{v}_\alpha}{\partial y} + \beta \frac{\partial h}{\partial x}\frac{\partial (h\dot{v}_\alpha)}{\partial y} \right]$$
$$+ \frac{\partial W}{\partial x} \left[\eta + \varepsilon \frac{1}{2}(u_\alpha^2 + v_\alpha^2) + \mu^2 \left(C_2 h^2 \frac{\partial \dot{v}_\alpha}{\partial y} + \beta h \frac{\partial (h\dot{v}_\alpha)}{\partial y} \right) \right] \Bigg\} dxdy$$
$$- \int_\Gamma n_x W \left\{ \eta + \varepsilon \frac{1}{2}(u_\alpha^2 + v_\alpha^2) + \mu^2 \left[C_2 h^2 \left(\frac{\partial \dot{u}_\alpha}{\partial x} + \frac{\partial \dot{v}_\alpha}{\partial y} \right) + \beta h \left(\frac{\partial h\dot{u}_\alpha}{\partial x} + \frac{\partial h\dot{v}_\alpha}{\partial y} \right) \right] \right\} d\Gamma \tag{67}$$

$$\iint_\Omega \left\{ W - \mu^2 \left[W \left(C_4 \frac{\partial h^2}{\partial y}\frac{\partial}{\partial y} + \beta \left(\frac{\partial h}{\partial y} \right)^2 \right) + \frac{\partial W}{\partial y} \left(C_5 h^2 \frac{\partial}{\partial y} + \frac{\beta}{2}\frac{\partial h^2}{\partial y} \right) \right] \right\} \dot{v}_\alpha dxdy$$
$$= \iint_\Omega \Bigg\{ \mu^2 W \left[C_2 \frac{\partial h^2}{\partial y}\frac{\partial \dot{u}_\alpha}{\partial x} + \beta \frac{\partial h}{\partial y}\frac{\partial (h\dot{u}_\alpha)}{\partial x} \right]$$
$$+ \frac{\partial W}{\partial y} \left[\eta + \varepsilon \frac{1}{2}(u_\alpha^2 + v_\alpha^2) + \mu^2 \left(C_2 h^2 \frac{\partial \dot{u}_\alpha}{\partial x} + \beta h \frac{\partial (h\dot{u}_\alpha)}{\partial x} \right) \right] \Bigg\} dxdy$$
$$- \int_\Gamma n_y W \left\{ \eta + \varepsilon \frac{1}{2}(u_\alpha^2 + v_\alpha^2) + \mu^2 \left[C_2 h^2 \left(\frac{\partial \dot{u}_\alpha}{\partial x} + \frac{\partial \dot{v}_\alpha}{\partial y} \right) + \beta h \left(\frac{\partial h\dot{u}_\alpha}{\partial x} + \frac{\partial h\dot{v}_\alpha}{\partial y} \right) \right] \right\} d\Gamma \tag{68}$$

$$\iint_\Omega WP \, dxdy = \iint_\Omega W \left(\frac{\partial u_\alpha}{\partial x} + \frac{\partial v_\alpha}{\partial y} \right) dxdy \tag{69}$$

in which

$$C_4 = \frac{1}{2}\beta(\beta + 1), \quad C_5 = \beta \left(\frac{1}{2}\beta + 1 \right), \tag{70}$$

and n_x and n_y are the x and y components of the outward unit normal vector to the boundary, $\mathbf{n}$, respectively.

The dependent variables are approximated in the form of linear combination of shape functions ($\psi_j(x, y)$) and the corresponding nodal values of dependent variable as follows:

$$\eta(x, y, \, n\Delta t) \simeq \sum_{j=1}^{ND} \psi_j(x, y) \{\eta\}_j^n \tag{71}$$

$$u_\alpha(x, y, \, n\Delta t) \simeq \sum_{j=1}^{ND} \psi_j(x, y) \{u\}_j^n \tag{72}$$

$$v_\alpha(x,y,\ n\Delta t) \simeq \sum_{j=1}^{ND} \psi_j(x,y)\{v\}_j^n \tag{73}$$

$$P(x,y,\ n\Delta t) \simeq \sum_{j=1}^{ND} \psi_j(x,y)\{P\}_j^n \tag{74}$$

where 'ND' is the total number of nodes in the domain and $n = 0,\ 1,\ 2,\ldots$, represent the time levels. The time step size Δt is a constant. The water depth and second-order spatial derivatives of the water depth are also approximated with the same set of shape functions, i.e.,

$$h(x,y) \simeq \sum_{j=1}^{ND} \psi_j(x,y)\{h\}_j \tag{75}$$

$$R_1(x,y) \simeq \sum_{j=1}^{ND} \psi_j(x,y)\{R_1\}_j \tag{76}$$

$$R_2(x,y) \simeq \sum_{j=1}^{ND} \psi_j(x,y)\{R_2\}_j \tag{77}$$

$$R_3(x,y) \simeq \sum_{j=1}^{ND} \psi_j(x,y)\{R_3\}_j \tag{78}$$

The Galerkin finite element method is applied here so that the weighting function ($W(x,y)$) is the same as shape function ($\psi(x,y)$).

Substituting (71) $\sim$ (78) into the weak forms (66) $\sim$ (69), we obtain the following matrix equations:

$$\sum_{j=1}^{ND} [M^\eta]_{ij}\{\dot{\eta}\}_j^n = \{f^\eta\}_i^n + \{q^\eta\}_i^n \tag{79}$$

$$\sum_{j=1}^{ND} [M^u]_{ij}\{\dot{u}\}_j^n = \{f^u\}_i^n + \{q^u\}_i^n \tag{80}$$

$$\sum_{j=1}^{ND} [M^v]_{ij}\{\dot{v}\}_j^n = \{f^v\}_i^n + \{q^v\}_i^n \tag{81}$$

$$\sum_{j=1}^{ND} [M^P]_{ij}\{P\}_j^n = \{f^P\}_i^n \tag{82}$$

in which $i = 1, 2, \ldots ND$. The detailed expressions for these matrices and vectors are given in the Appendix.

3.1.2 Element and shape function

For spatial approximation in two-dimensional finite element method, the computational domain Ω is partitioned into a set of non-overlapping elements. Linear three-node triangular and four-node rectangular elements are used in this work. A triangular element is known to be very suitable for approximating any arbitrary boundary shape and domain. A 'node' is defined at the vertices of the triangles and there are total 'ND' number of nodes in the domain. The Lagrange interpolation function is chosen to be a shape function, with the property at each node,

$$\psi_i(x_j,\ y_j) = \delta_{ij} \tag{83}$$

where δ_{ij} is the Dirac delta function.

On each triangular element (Ω_e) there will be three local shape functions ($\psi_1^e,\ \psi_2^e,\ \psi_3^e$), which is shown in Figure 1.

3.2 Time integration scheme

The time integration scheme should be accurate enough so that the truncation errors would not produce any non-physical dispersion or dissipation. In this section, we shall describe the Adams-Bashforth-Moulton predictor-corrector scheme to integrate (79) $\sim$ (82). This scheme is one of widely used time integration schemes. The basic idea of the procedure is described as follows. First, based on the solution from the current time step, an initial guess for the solution of the governing equation at the next time step is made (predictor stage). The predicted solution is inserted into the right-hand-side of the governing equation to find the updated – or "corrected" – solution (corrector stage). The updated solution is inserted back into the right-hand side of the governing equation to find another "updated" solution. This procedure is repeated until the difference between two successive updated solutions is smaller than error tolerance (Lapidus and Seinfeld 1971).

Specifically, in the present model the third-order Adams-Bashforth scheme is employed for the predictor step.

$$P[\eta]:\ \ [M^\eta]_{ij}\left(\frac{\{\eta\}_{j(0)}^{n+1} - \{\eta\}_j^n}{\Delta t}\right) = \frac{1}{12}\left[23\{f^\eta\}_i^n - 16\{f^\eta\}_i^{n-1} + 5\{f^\eta\}_i^{n-2}\right] \tag{84}$$

$$P[u_\alpha]:\ \ [M^u]_{ij}\left(\frac{\{u\}_{j(0)}^{n+1} - \{u\}_j^n}{\Delta t}\right) = \frac{1}{12}\left[23\{f^u\}_i^n - 16\{f^u\}_i^{n-1} + 5\{f^u\}_i^{n-2}\right] \tag{85}$$

$$P[v_\alpha]:\ \ [M^v]_{ij}\left(\frac{\{v\}_{j(0)}^{n+1} - \{v\}_j^n}{\Delta t}\right) = \frac{1}{12}\left[23\{f^v\}_i^n - 16\{f^v\}_i^{n-1} + 5\{f^v\}_i^{n-2}\right] \tag{86}$$

We remark here that the forcing vectors, $\{f^u\}$ and $\{f^v\}$ contain the time derivative of velocity ($\{\dot{v}\}$ in $\{f^u\}$ and $\{\dot{u}\}$ in $\{f^v\}$). For the predictor stage, these derivatives are evaluated as

$$\{\dot{r}\}_i^n = \frac{1}{2\Delta t}\left[3\{r\}_i^n - 4\{r\}_i^{n-1} + \{r\}_i^{n-2}\right] + O(\Delta t^2) \tag{87}$$

$$\{\dot{r}\}_i^{n-1} = \frac{1}{2\Delta t}\left[\{r\}_i^n - \{r\}_i^{n-2}\right] + O(\Delta t^2) \tag{88}$$

$$\{\dot{r}\}_i^{n-2} = \frac{-1}{2\Delta t}\left[3\{r\}_i^{n-2} - 4\{r\}_i^{n-1} + \{r\}_i^n\right] + O(\Delta t^2) \tag{89}$$

where $\{r\}$ represents $\{u\}$ or $\{v\}$.

Solving equations (84), (85) and (86), one obtains solutions for the first predicted values, $\{\eta\}_{j(0)}^{n+1}$, $\{u\}_{j(0)}^{n+1}$ and $\{v\}_{j(0)}^{n+1}$ at j-th node and $(n+1)$-th time step. Using these values, the auxiliary variable is updated at the $(n+1)$-th time level by solving equation (82); i.e.,

$$\{P\}_{j(0)}^{n+1} = [M^P]_{ij}^{-1}\{f^P\}_{i(0)}^{n+1} \tag{90}$$

To update the forcing vectors of the corrector stage, the time derivative terms in the forcing vectors need to be evaluated in the following manner:

$$\{\dot{r}\}_{i(0)}^{n+1} = \frac{1}{6\Delta t}\left[11\{r\}_{i(0)}^{n+1} - 18\{r\}_i^n + 9\{r\}_i^{n-1} - 2\{r\}_i^{n-2}\right] + O(\Delta t^3) \tag{91}$$

$$\{\dot{r}\}_{i(0)}^{n} = \frac{1}{6\Delta t}\left[2\{r\}_{i(0)}^{n+1} - 3\{r\}_i^n - 6\{r\}_i^{n-1} + \{r\}_i^{n-2}\right] + O(\Delta t^3) \tag{92}$$

$$\{\dot{r}\}_{i(0)}^{n-1} = \frac{1}{6\Delta t}\left[-\{r\}_{i(0)}^{n+1} + 6\{r\}_i^n - 3\{r\}_i^{n-1} - 2\{r\}_i^{n-2}\right] + O(\Delta t^3) \tag{93}$$

$$\{\dot{r}\}_{i(0)}^{n-2} = \frac{1}{6\Delta t}\left[2\{r\}_{i(0)}^{n+1} - 9\{r\}_i^n + 18\{r\}_i^{n-1} - 11\{r\}_i^{n-2}\right] + O(\Delta t^3) \tag{94}$$

After the forcing vectors are updated at the $(n+1)$-th time level; i.e., $\{f^\eta\}_{i(0)}^{n+1}$, $\{f^u\}_{i(0)}^{n+1}$, and $\{f^v\}_{i(0)}^{n+1}$, the corrected solutions are then obtained by applying the fourth-order Adams-Moulton corrector method (Lapidus and Seinfeld 1971). The subsequent iteration procedure can be explained as follows. To obtain the s-th corrected value for $\{\eta\}_{j(s)}^{n+1}$, in which s denotes the number of iteration ($s = 1, 2, ...$), the continuity equation (79) is integrated in the following manner:

$$C[\eta]: \quad \{\eta\}_{j(s)}^{n+1} = \{\eta\}_j^n + \frac{\Delta t}{24}[M^\eta]_{ij}^{-1}\Big(9\{f^\eta\}_{i(s-1)}^{n+1} + 19\{f^\eta\}_i^n - 5\{f^\eta\}_i^{n-1} + \{f^\eta\}_i^{n-2}\Big) \tag{95}$$

Using $\{\eta\}_{j(s)}^{n+1}$, $\{u\}_{j(s-1)}^{n+1}$, and $\{v\}_{j(s-1)}^{n+1}$, we update the forcing vector $\{f^u\}_{i(s-1)}^{n+1}$. The momentum equation (80) can be integrated as

$$C[u_\alpha]: \quad \{u\}_{j(s)}^{n+1} = \{u\}_j^n + \frac{\Delta t}{24}[M^u]_{ij}^{-1}\Big(9\{f^u\}_{i(s-1)}^{n+1} + 19\{f^u\}_i^n - 5\{f^u\}_i^{n-1} + \{f^u\}_i^{n-2}\Big) \tag{96}$$

Likewise, with $\{\eta\}_{j(s)}^{n+1}$, $\{u\}_{j(s)}^{n+1}$ and $\{v\}_{j(s-1)}^{n+1}$, the forcing vector $\{f^v\}_{i(s-1)}^{n+1}$ is updated and the momentum equation (81) is integrated as

$$C[v_\alpha]: \quad \{v\}_{j(s)}^{n+1} = \{v\}_j^n + \frac{\Delta t}{24}[M^v]_{ij}^{-1}\Big(9\{f^v\}_{i(s-1)}^{n+1} + 19\{f^v\}_i^n - 5\{f^v\}_j^{n-1} + \{f^v\}_i^{n-2}\Big) \tag{97}$$

If the next corrector step is required, then the forcing vector for auxiliary variable $\{f^P\}_{i(s)}^{n+1}$ is updated using $\{u\}_{j(s)}^{n+1}$ and $\{v\}_{j(s)}^{n+1}$ and equation (82) is solved for $\{P\}_{j(s)}^{n+1}$.

The relative errors between two successive correction steps are defined as

$$\Delta e_\eta = \max\left(\frac{\{\eta\}_{j(s)}^{n+1} - \{\eta\}_{j(s-1)}^{n+1}}{\{\eta\}_{j(s)}^{n+1}}\right) \tag{98}$$

$$\Delta e_u = \max\left(\frac{\{u\}_{j(s)}^{n+1} - \{u\}_{j(s-1)}^{n+1}}{\{u\}_{j(s)}^{n+1}}\right) \tag{99}$$

$$\Delta e_v = \max\left(\frac{\{v\}_{j(s)}^{n+1} - \{v\}_{j(s-1)}^{n+1}}{\{v\}_{j(s)}^{n+1}}\right) \tag{100}$$

The corrector step continues until Δe_η, Δe_u and Δe_v are all less than 10^{-4}.

3.3 Boundary conditions

Applying an appropriate boundary condition is necessary to obtain proper numerical solutions in a finite computational domain. We shall discuss three types of boundary conditions in this section: (1) impermeable reflective wall boundary condition, (2) wave maker (or incident) boundary condition, and (3) absorbing (or outgoing) boundary condition.

3.3.1 Reflective wall boundary condition

Here, an attempt is made to implement an reflective wall boundary condition in a mathematically and physically consistent manner. The physical boundary condition at the rigid impermeable wall is that no fluid should pass through the wall, *i.e.* no-flux boundary condition. To satisfy no-flux boundary condition in the depth-integrated equation system, the depth-averaged horizontal velocity normal to the wall should always be zero.

$$\bar{\mathbf{u}} \cdot \mathbf{n} = 0, \qquad \mathbf{x} \in \Gamma_W \tag{101}$$

where Γ_W is wall boundary. The above condition needs to be rewritten in terms of $\mathbf{u}_\alpha$, since $\mathbf{u}_\alpha$ is one of the unknown variables. Under the assumption of $O(\nabla h) \approx O(\mu^2)$ near the boundary, the relationship between $\bar{\mathbf{u}}$ and $\mathbf{u}_\alpha$ can be written as (from the equation (36))

$$\bar{\mathbf{u}} = \mathbf{u}_\alpha + \mu^2 h^2 C_6 \nabla P \tag{102}$$

in which

$$C_6 = \frac{\beta^2}{2} + \beta + \frac{1}{3}$$

Hence, the no-flux boundary condition of $\mathbf{u}_\alpha$ at the reflective boundary can be expressed as

$$\mathbf{u}_\alpha \cdot \mathbf{n} = -\mu^2 h^2 C_6 \nabla P \cdot \mathbf{n} \tag{103}$$

This condition will be used when the boundary condition of momentum equation is discussed.

Now, let us derive the no-flux boundary condition from the continuity equation. By integrating equation (58) over the domain Ω, we obtain

$$\int_\Omega \left\{ \frac{\partial \eta}{\partial t} + \nabla \cdot [(h + \varepsilon\eta)\mathbf{u}_\alpha] + \mu^2 \nabla \cdot [C_1 h^3 \nabla P + C_3 h^2 \nabla(\nabla \cdot (h\mathbf{u}_\alpha))] \right\} d\Omega = 0 \tag{104}$$

Using the divergence theorem and taking the time derivative of free surface outside of the spatial integral gives

$$\frac{\partial}{\partial t} \int_\Omega \eta d\Omega + \int_\Gamma \left\{ [(h+\varepsilon\eta)\mathbf{u}_\alpha] \cdot \mathbf{n} + \mu^2 [C_1 h^3 \nabla P + C_3 h^2 \nabla(\nabla \cdot (h\mathbf{u}_\alpha))] \cdot \mathbf{n} \right\} d\Gamma = 0 \tag{105}$$

We will assume $\Gamma \equiv \Gamma_W$. In other words, the whole domain is completely enclosed by impermeable walls. It is noted that this assumption is consistent with our overall design of the computational domain, since the radiating open boundary condition will be treated as a sponge layer located in front of the wall and the

wave maker boundary will be located inside domain (Figure 2). These boundary conditions will be discussed in detail in the following sections.

Since $\Gamma \equiv \Gamma_W$, there is no loss or gain of mass in the whole domain. So the time derivative of total mass, which is the first term in the above equation, is zero. Using the vector identity, the third term in the boundary integral in (105) can be expressed as

$$\begin{aligned}
\mu^2 C_3 h^2 \nabla(\nabla \cdot (h\mathbf{u}_\alpha)) &= \mu^2 C_3 h^2 \Big\{ \nabla(\nabla h \cdot \mathbf{u}_\alpha) + \nabla(hP) \Big\} \\
&= \mu^2 C_3 h^2 \Big\{ (\nabla h \cdot \nabla)\mathbf{u}_\alpha + (\mathbf{u}_\alpha \cdot \nabla)\nabla h + \nabla h \times (\nabla \times \mathbf{u}_\alpha) \\
&\qquad + \mathbf{u}_\alpha \times (\nabla \times \nabla h) + P\nabla h + h\nabla P \Big\} \qquad (106)
\end{aligned}$$

Since $O(\nabla \times \mathbf{u}_\alpha) \approx O(\varepsilon\mu^2)$, the order of the third term on the right hand side of the above equation is $O(\varepsilon\mu^4)$. The fourth term is also zero since the curl of gradient is identically zero. With these results, equation (105) can be rewritten as

$$\int_\Gamma \Big\{ [h + \varepsilon\eta + \mu^2 C_3 h^2 (\nabla h \cdot \nabla)]\mathbf{u}_\alpha + \mu^2 [C_6 h^3 \nabla P + C_3 h^2 (\mathbf{u}_\alpha \cdot \nabla + P)\nabla h] \Big\} \cdot \mathbf{n}\, d\Gamma = 0 \qquad (107)$$

It can be shown that under the assumption of $O(\nabla h) \approx O(\mu^2)$ near the boundary, by using equation (103), the integrand in the equation (107) is zero with the truncation error of $O(\varepsilon\mu^2, \mu^4)$.

It is noted that the integrand in the boundary integral in equation (105) is identical to that of boundary integral in the weak form of the continuity equation (66) multiplied by the weighting function W. With the same argument shown before, the integrand multiplied by weighting function W can be shown to be zero. Since the integrand is identically zero, the boundary integral of the weak form for the continuity equation vanishes. Therefore, there is no additional work need to be done for the treatment of the boundary condition for the free surface at solid walls.

Let us consider the application of the no-flux boundary condition to the momentum equations. As we mentioned before, the physical boundary condition imposes a constraint on the normal velocity at the wall. When the normal velocity is specified at a boundary node, the momentum equation in the tangential direction is solved for the tangential velocity at the node. Since the orientation of a boundary segment does not always coincide with the global Cartesian axes, we will consider a locally rotated coordinate system at a boundary node. This local coordinate transformation idea is based on the previous work by Engelman *et al.* (1982) and Pinder and Gray (1977). Let us introduce a local coordinate system (n, T) with n aligned with the outward normal and T aligned with the tangent at

the boundary. This corresponds to locally rotating the (x, y) coordinate system by an angle θ to the new coordinate system (n, T) in the counter-clockwise direction. Hence velocity components (u_n, u_T) in terms of the coordinate system (n, T) are now related to the velocity components (u_α, v_α) in (x, y) coordinate system by

$$\begin{aligned}
\begin{pmatrix} u_n \\ u_T \end{pmatrix} &= \begin{bmatrix} cos\,\theta & sin\,\theta \\ -sin\,\theta & cos\,\theta \end{bmatrix} \begin{pmatrix} u_\alpha \\ v_\alpha \end{pmatrix} \\
&= \begin{bmatrix} n_x & n_y \\ T_x & T_y \end{bmatrix} \begin{pmatrix} u_\alpha \\ v_\alpha \end{pmatrix} \\
&= \begin{pmatrix} \mathbf{n} \cdot \mathbf{u}_\alpha \\ \mathbf{T} \cdot \mathbf{u}_\alpha \end{pmatrix}
\end{aligned} \tag{108}$$

in which $\mathbf{n} = (n_x, n_y)$ is the outward normal vector and $\mathbf{T} = (T_x, T_y)$ is the tangent vector to the boundary.

Now let us transform the x and y momentum equations to the tangential momentum equation with the constraint on the normal velocity component. The tangential momentum equation at the boundary node is obtained from the inner product of (x, y) momentum equations with the tangent vector $\mathbf{T}$ at that boundary node,

$$\begin{aligned}
& \mathbf{T} \cdot \left\{ \dot{\mathbf{u}}_\alpha + \nabla\eta + \frac{\varepsilon}{2}\nabla(\mathbf{u}_\alpha \cdot \mathbf{u}_\alpha) + \mu^2 \left[C_2 h^2 \nabla \left(\nabla \cdot \dot{\mathbf{u}}_\alpha \right) + \beta h \nabla \left(\nabla \cdot (h\dot{\mathbf{u}}_\alpha) \right) \right] \right\} \\
= \; & T_x \left\{ \dot{u}_\alpha + \mu^2 \left[C_2 h^2 \frac{\partial^2 \dot{u}_\alpha}{\partial x^2} + \beta h \frac{\partial^2 (h\dot{u}_\alpha)}{\partial x^2} \right] \right. \\
& \qquad \left. + \frac{\partial}{\partial x} \left[\eta + \varepsilon \frac{1}{2}(u_\alpha^2 + v_\alpha^2) + \mu^2 \left(C_2 h^2 \frac{\partial \dot{v}_\alpha}{\partial y} + \beta h \frac{\partial (h\dot{v}_\alpha)}{\partial y} \right) \right] \right\} \\
& + T_y \left\{ \dot{v}_\alpha + \mu^2 \left[C_2 h^2 \frac{\partial^2 \dot{v}_\alpha}{\partial y^2} + \beta h \frac{\partial^2 (h\dot{v}_\alpha)}{\partial y^2} \right] \right. \\
& \qquad \left. + \frac{\partial}{\partial y} \left[\eta + \varepsilon \frac{1}{2}(u_\alpha^2 + v_\alpha^2) + \mu^2 \left(C_2 h^2 \frac{\partial \dot{u}_\alpha}{\partial x} + \beta h \frac{\partial (h\dot{u}_\alpha)}{\partial x} \right) \right] \right\} \\
= \; & 0
\end{aligned} \tag{109}$$

The constraint on the normal velocity component is obtained from the physical no-flux boundary condition and it is shown in (102). It can be rewritten as,

$$\mathbf{n} \cdot \mathbf{u}_\alpha \;=\; n_x\, u_\alpha + n_y\, v_\alpha = -\mu^2 h^2 C_6 \nabla P \cdot \mathbf{n} \tag{110}$$

It is important that the normal velocity at the boundary is not simply zero, but is related to the normal gradient of the auxiliary variable P.

We have constructed a set of equations at the boundary which is different from the governing equations in the domain. To solve the new set of equations in the framework of the time integration procedure, where the equation for $\dot{u}$ is solved independently of that for $\dot{v}$, a decision has to be made whether the time integration is performed for $\dot{u}$ or for $\dot{v}$ in the tangential momentum. In this work, the choice is made according to the angle of normal vector, θ. For example, when $\theta = 0$, which means that the boundary is parallel to the y-axis, $\dot{v}$ should be solved in the tangential momentum equation and $u = 0$ should be specified from the constraint equation. On the other hand, if $\theta = \pi/2$ and the boundary is parallel to the x-axis, $\dot{u}$ should be solved and $v = 0$ should be imposed. We suggest that

$$\begin{cases} (\frac{\pi}{4} \le \theta < \frac{3\pi}{4}) \text{ or } (\frac{5\pi}{4} \le \theta < \frac{7\pi}{4}) : \dot{u} \text{ is solved from (109), } v \text{ is decided from (110)} \\ (-\frac{\pi}{4} \le \theta < \frac{\pi}{4}) \text{ or } (\frac{3\pi}{4} \le \theta < \frac{5\pi}{4}) : \dot{v} \text{ is solved from (109), } u \text{ is decided from (110)} \end{cases} \tag{111}$$

Now the weak form of the tangential momentum equation needs to be constructed. And we shall show that boundary integral term in the weak form vanishes. The weak form for the time integration of $\dot{u}_\alpha$ can be expressed as

$$\begin{aligned}
&\iint_\Omega \left\{ W - \mu^2 \left[W \left(C_4 \frac{\partial h^2}{\partial x}\frac{\partial}{\partial x} + \beta \left(\frac{\partial h}{\partial x}\right)^2 \right) + \frac{\partial W}{\partial x}\left(C_5 h^2 \frac{\partial}{\partial x} + \frac{\beta}{2}\frac{\partial h^2}{\partial x} \right) \right] \right. \\
&\qquad \left. -\mu^2 \frac{T_y}{T_x} \left[W \left(C_4 \frac{\partial h^2}{\partial y}\frac{\partial}{\partial x} + \beta \frac{\partial h}{\partial y}\frac{\partial h}{\partial x} \right) + \frac{\partial W}{\partial y}\left(C_5 h^2 \frac{\partial}{\partial x} + \frac{\beta}{2}\frac{\partial h^2}{\partial x} \right) \right] \right\} \dot{u}_\alpha \, d\Omega \\
&= \iint_\Omega \left\{ \mu^2 W \left[C_2 \frac{\partial h^2}{\partial x}\frac{\partial \dot{v}_\alpha}{\partial y} + \beta \frac{\partial h}{\partial x}\frac{\partial (h\dot{v}_\alpha)}{\partial y} \right] \right. \\
&\qquad + \frac{\partial W}{\partial x}\left[\eta + \varepsilon \frac{1}{2}(u_\alpha^2 + v_\alpha^2) + \mu^2 \left(C_2 h^2 \frac{\partial \dot{v}_\alpha}{\partial y} + \beta h \frac{\partial (h\dot{v}_\alpha)}{\partial y} \right) \right] \\
&\qquad + \frac{T_y}{T_x} W \left[-\dot{v}_\alpha + \mu^2 \left(C_2 \frac{\partial h^2}{\partial y}\frac{\partial \dot{v}_\alpha}{\partial y} + \beta \frac{\partial h}{\partial y}\frac{\partial (h\dot{v}_\alpha)}{\partial y} \right) \right] \\
&\qquad \left. + \frac{T_y}{T_x}\frac{\partial W}{\partial y}\left[\eta + \varepsilon \frac{1}{2}(u_\alpha^2 + v_\alpha^2) + \mu^2 \left(C_2 h^2 \frac{\partial \dot{v}_\alpha}{\partial y} + \beta h \frac{\partial (h\dot{v}_\alpha)}{\partial y} \right) \right] \right\} d\Omega \\
&- \int_\Gamma n_x W \left\{ \eta + \varepsilon \frac{1}{2}(u_\alpha^2 + v_\alpha^2) \right. \\
&\qquad \left. + \mu^2 \left[C_2 h^2 \left(\frac{\partial \dot{u}_\alpha}{\partial x} + \frac{\partial \dot{v}_\alpha}{\partial y} \right) + \beta h \left(\frac{\partial h\dot{u}_\alpha}{\partial x} + \frac{\partial h\dot{v}_\alpha}{\partial y} \right) \right] \right\} d\Gamma \\
&- \int_\Gamma \frac{T_y}{T_x} n_y W \left\{ \eta + \varepsilon \frac{1}{2}(u_\alpha^2 + v_\alpha^2) \right. \\
&\qquad \left. + \mu^2 \left[C_2 h^2 \left(\frac{\partial \dot{u}_\alpha}{\partial x} + \frac{\partial \dot{v}_\alpha}{\partial y} \right) + \beta h \left(\frac{\partial h\dot{u}_\alpha}{\partial x} + \frac{\partial h\dot{v}_\alpha}{\partial y} \right) \right] \right\} d\Gamma
\end{aligned} \tag{112}$$

Here, it is clearly shown that all boundary integral terms are canceled each other out, since $n_x = -\frac{T_y}{T_x} n_y$. It is noted that the weak form is arranged in such way that the boundary integral cancelation can take place. If we compare the above equation with the weak form of u_α in the domain (equation (67)), we can see additional terms followed by $\frac{T_y}{T_x} (= -cot\ \theta)$ have appeared.

This equation is solved together with

$$v_\alpha = -\frac{1}{n_y}(n_x\, u_\alpha + \mu^2 h^2 C_6 \nabla P \cdot \mathbf{n}) \tag{113}$$

at the boundary node whose normal angle is in the range of $(\frac{\pi}{4} \leq \theta < \frac{3\pi}{4})$ or $(\frac{5\pi}{4} \leq \theta < \frac{7\pi}{4})$. Outside of this range of angle, a different set of equations is solved. The weak form for $\dot{v}_\alpha$ at the boundary can be written as

$$\begin{aligned}
&\iint_\Omega \left\{ W - \mu^2 \left[W \left(C_4 \frac{\partial h^2}{\partial y} \frac{\partial}{\partial y} + \beta \left(\frac{\partial h}{\partial y} \right)^2 \right) + \frac{\partial W}{\partial y} \left(C_5 h^2 \frac{\partial}{\partial y} + \frac{\beta}{2} \frac{\partial h^2}{\partial y} \right) \right] \right. \\
&\qquad \left. -\mu^2 \frac{T_x}{T_y} \left[W \left(C_4 \frac{\partial h^2}{\partial x} \frac{\partial}{\partial y} + \beta \frac{\partial h}{\partial x} \frac{\partial h}{\partial y} \right) + \frac{\partial W}{\partial x} \left(C_5 h^2 \frac{\partial}{\partial y} + \frac{\beta}{2} \frac{\partial h^2}{\partial y} \right) \right] \right\} \dot{v}_\alpha \, d\Omega \\
&= \iint_\Omega \left\{ \mu^2 W \left[C_2 \frac{\partial h^2}{\partial y} \frac{\partial \dot{u}_\alpha}{\partial x} + \beta \frac{\partial h}{\partial y} \frac{\partial (h \dot{u}_\alpha)}{\partial x} \right] \right. \\
&\qquad + \frac{\partial W}{\partial y} \left[\eta + \varepsilon \frac{1}{2} (u_\alpha^2 + v_\alpha^2) + \mu^2 \left(C_2 h^2 \frac{\partial \dot{u}_\alpha}{\partial x} + \beta h \frac{\partial (h \dot{u}_\alpha)}{\partial x} \right) \right] \\
&\qquad + \frac{T_x}{T_y} W \left[-\dot{u}_\alpha + \mu^2 \left(C_2 \frac{\partial h^2}{\partial x} \frac{\partial \dot{u}_\alpha}{\partial x} + \beta \frac{\partial h}{\partial x} \frac{\partial (h \dot{u}_\alpha)}{\partial x} \right) \right] \\
&\qquad \left. + \frac{T_x}{T_y} \frac{\partial W}{\partial x} \left[\eta + \varepsilon \frac{1}{2} (u_\alpha^2 + v_\alpha^2) + \mu^2 \left(C_2 h^2 \frac{\partial \dot{u}_\alpha}{\partial x} + \beta h \frac{\partial (h \dot{u}_\alpha)}{\partial x} \right) \right] \right\} d\Omega \\
&- \int_\Gamma n_y W \left\{ \eta + \varepsilon \frac{1}{2} (u_\alpha^2 + v_\alpha^2) \right. \\
&\qquad \left. + \mu^2 \left[C_2 h^2 \left(\frac{\partial \dot{u}_\alpha}{\partial x} + \frac{\partial \dot{v}_\alpha}{\partial y} \right) + \beta h \left(\frac{\partial h \dot{u}_\alpha}{\partial x} + \frac{\partial h \dot{v}_\alpha}{\partial y} \right) \right] \right\} d\Gamma \\
&- \int_\Gamma \frac{T_x}{T_y} n_x W \left\{ \eta + \varepsilon \frac{1}{2} (u_\alpha^2 + v_\alpha^2) \right. \\
&\qquad \left. + \mu^2 \left[C_2 h^2 \left(\frac{\partial \dot{u}_\alpha}{\partial x} + \frac{\partial \dot{v}_\alpha}{\partial y} \right) + \beta h \left(\frac{\partial h \dot{u}_\alpha}{\partial x} + \frac{\partial h \dot{v}_\alpha}{\partial y} \right) \right] \right\} d\Gamma
\end{aligned} \tag{114}$$

The boundary integral terms also vanishes, since $n_y = -\frac{T_x}{T_y} n_x$. And the constraint equation which is to be solved together with the above equation is,

$$u_\alpha = -\frac{1}{n_x}(n_y\, v_\alpha + \mu^2 h^2 C_6 \nabla P \cdot \mathbf{n}) \tag{115}$$

Finally, let us discuss the boundary condition for the auxiliary variable. Usually when an auxiliary variable is introduced in order to reduce the higher order spatial derivative, a new boundary condition for the additional variable is needed. In the literature, Li et al. (1999) used $\frac{\partial \eta}{\partial x}$ and $\frac{\partial \eta}{\partial y}$ as auxiliary variables for Beji and Nodaoka's (1996) extended Boussinesq equations and they need to specify $\frac{\partial \eta}{\partial n} = 0$ at the solid wall boundary. Walkley (1999) introduced an auxiliary vector $\mathbf{W} := C_1 h^3 \nabla(\nabla \cdot \mathbf{u}_\alpha) + C_3 h^2 \nabla(\nabla \cdot (h\mathbf{u}_\alpha))$ for Nwogu's (1993) extended Boussinesq equations. He derived $\mathbf{W} \cdot \mathbf{n} = 0$ as a boundary condition for the new variable under the assumption of $\mathbf{u}_\alpha \cdot \mathbf{n} = 0$.

In the present work, however, there is no need for introducing additional boundary condition for the new variable. The boundary integral does not exist in the weak form of the auxiliary variable since the integration by parts is not performed. The effect on the boundary caused by the auxiliary variable acts on the determination of normal velocity in a physically consistent way. In other words we do not introduce any non-physical constraint at the boundary.

3.3.2 Wave maker boundary condition

It is important to implement the incident wave boundary condition into the numerical model, since steady state solutions are frequently required for practical problems. With a proper choice of incident and outgoing wave boundary conditions, steady state solutions can be obtained in the time domain model. The following procedure is used to implement the incident wave boundary condition in the present FEM with the implicit time integration scheme.

At the incident wave boundary the time series of η, u and v are known. Since the nodal value at the boundary is known, it is regarded as an essential boundary condition. As shown in the previous section, equation (79) is solved for $\{\eta\}_j^{n+1}$. Since $\{\eta\}_{j=m}^{n+1}$ is known, the matrix $[M^\eta]_{ij}$ and vector $\{f^\eta\}_i^n$ should be modified. Specifically, the elements of the m-th row of $[M^\eta]$ are set to zero, except for the element $[M^\eta]_{mm}$ that is set to unity. The m-th row of the vector $\{f^\eta\}_{i=m}^n$ is also replaced by the following known information:

$$\{f^\eta\}_m^n = \left(\frac{\{\eta\}_m^{n+1*} - \{\eta\}_m^n}{\Delta t} \right) \tag{116}$$

where $\{\eta\}_m^{n+1*}$ is the known value at next time step. For the predictor step of continuity equation (84), the m-th row of the matrix equation becomes,

$$[0\,0\,\cdots 1 \cdots 0\,0] \left(\frac{\{\eta\}_{m(0)}^{n+1} - \{\eta\}_m^n}{\Delta t} \right) = \left(\frac{\{\eta\}_m^{n+1*} - \{\eta\}_m^n}{\Delta t} \right) \tag{117}$$

in which the '1' locates at m-th column. Consequently, the boundary condition for $\{\eta\}_m^{n+1}$ has been applied. The same approach is applied to the momentum equations and the subsequent iterative corrector procedure.

As an example, let us consider a finite-difference-like structured quadrilateral grid system on a rectangular domain, in which the node number $m := (k, l)$ is defined in such a way that $\Delta x_k = x_k - x_{k-1},\ k = 1,\ 2, \ldots,\ K$ and $\Delta y_l = y_l - y_{l-1},\ l = 1,\ 2, \ldots,\ L$. If the incident wave boundary is located at the left-hand side of the computational domain ($x = 0$), the given surface elevation and velocities are assigned to nodal values at m_b, in which m_b represents a set of nodes whose $k = 1, 2$ and $l = 1,\ 2, \ldots,\ L$.

The solution at nodes ($k = 3, l = 1,\ 2, \ldots,\ L$) where the real computational domain begins, depends on nodal values at m_b, since the weighting function is distributed over four elements, *e.g* nodal values at ($k = 3, l = 2$) are coupled with the nodal value at ($2 \leq k \leq 4, 1 \leq l \leq 3$). Note that the information of η, u and v at nodes ($k = 1, l = 1,\ 2, \ldots,\ L$) is necessary for the evaluation of auxiliary variable P at nodes ($k = 2, l = 1,\ 2, \ldots,\ L$).

We should remark here that imposing two adjacent Dirichlet conditions is similar to specifying a first spatial derivative at the boundary. This may lead to difficulties for nonlinear wave input, similar to that encountered from imposing solution and its derivative at a single point. However, by increasing the number of nodes where the Dirichlet conditions is applied, we can increase, in principle, the accuracy of spatial derivative at the boundary.

3.3.3 Absorbing boundary condition

In order to perform practical computations, it is inevitable to restrict the size of the computational domain and apply a radiation boundary condition, which allows waves to propagate out of the domain, at the radiation boundary. It is important to minimize the non-physical reflection at this boundary. Here, a sponge layer boundary condition is adopted near the boundary to absorb all wave energy arriving at the boundary from within the fluid domain. In Figure 2, Γ_W^E indicates the impermeable wall boundary locating at the end of the sponge layer and Γ^S denotes the starting position of the sponge layer. The selection of Γ^S is problem dependent and Γ^S is decided in such a way that it can provide enough thickness of the sponge layer. $\mathbf{x}_C$ is defined as a center of radiation and is selected in such a way that the line connecting $\mathbf{x}_C$ and a point on Γ_W^E can offer a proper radiation direction. If the sponge layer can effectively damp out the wave energy, it is unnecessary to treat Γ_W^E as a radiation boundary condition, since no wave will reach Γ_W^E. However, in this case, we need a rather thick sponge layer.

The sponge layer is installed by adding the following terms

$$S_\eta = C_\eta \nabla^2 \eta \tag{118}$$

$$S_u = -C_{u1} u + C_{u2} \nabla^2 u \tag{119}$$

$$S_v = -C_{u1}v + C_{u2}\nabla^2 v \tag{120}$$

to the right hand side of the continuity equation (62), and momentum equations (63), and (64), respectively. The linear damping terms with u and v are called "Newtonian cooling" and those with second-order derivative terms are artificial viscous terms (Israeli and Orszag 1981).

The damping coefficients C_η, C_{u1}, and C_{u2} decrease exponentially away from the boundary Γ_W^E and they are defined as

$$C_\eta = G_1^\eta \frac{exp[\parallel \mathbf{x}-\mathbf{x}_s \parallel / \parallel \mathbf{x}_e-\mathbf{x}_s \parallel]^{G_2^\eta} - 1}{exp(1)-1} \tag{121}$$

$$C_{u1} = \omega\, G_1^{u1} \frac{exp[\parallel \mathbf{x}-\mathbf{x}_s \parallel / \parallel \mathbf{x}_e-\mathbf{x}_s \parallel]^{G_2^{u1}} - 1}{exp(1)-1} \tag{122}$$

$$C_{u2} = \omega\, G_1^{u2} \frac{exp[\parallel \mathbf{x}-\mathbf{x}_s \parallel / \parallel \mathbf{x}_e-\mathbf{x}_s \parallel]^{G_2^{u2}} - 1}{exp(1)-1} \tag{123}$$

where $\mathbf{x}_s$ is the starting coordinate the sponge layer ($\mathbf{x}_s \in \Gamma^S$) and $\mathbf{x}_e$ is the ending coordinate of the sponge layer ($\mathbf{x}_e \in \Gamma_W^E$), ω is the frequency of wave to be damped, and $G_1^\eta, G_2^\eta, G_1^{u1}, G_2^{u1}, G_1^{u2}, G_2^{u2}$ are constants to be determined for tuning the amount of viscosity at the boundary. These constants are problem dependent. For given $\mathbf{x}$, $\mathbf{x}_s$ and $\mathbf{x}_e$ are coordinates of the points at which the line connecting $\mathbf{x}$ and $\mathbf{x}_C$ intersects Γ^S and Γ_W^E, respectively.

The width of the sponge layer is usually chosen to be two or three times the wave length.

3.4 Discussion on the choice of auxiliary variable

The choice of an auxiliary variable plays an important role in constructing the finite element model since it affects the treatment of boundary condition and the time integration procedure. In the present approach the choice of an auxiliary variable P is guided by three factors.

First, the computational cost should not be high. If $\frac{\partial u}{\partial x}$ (or $\frac{\partial^2 u}{\partial x^2}$) and $\frac{\partial v}{\partial y}$ (or $\frac{\partial^2 v}{\partial y^2}$) were to be used as the auxiliary variables, or Walkley and Berzins' (1999) new variable were to be used, two additional unknowns would have been introduced into the system so that at each time step we need to solve five equations for 5×ND unknowns. In the present work, four equations are solved for 4×ND unknowns. The second factor is the possibility of extention to fully nonlinear and weakly dispersive wave equations. It is straightforward for our choice but it is not for Walkley and Berzins' (1999). Finally, introducing the new variable should not complicate the treatment of boundary condition or require the inclusion of any non-physical

conditions on the boundary. As we mentioned before, the present choice does not require any additional treatment on the boundary.

4 Input data file

Let us briefly show the sample example of input data file. The computational domain is shown in Figure 3. The upper and lower boundary is regarded as solid wall boundary, the left hand side boundary as inflow and the right hand side boundary as radiation. The input data file structure is shown below.

Input Data file structure

1. Total number of node [I15]

2. Total number of element [I15]

3. Coordinate of global node :
   - ▷ row indicates global node number
   - ▷ the first and second column shows x- and y-coordinates of the node in the mesh.

   (global x-coordinate : global y-coordinate) [2F15.7]

4. Connectivity table :
   - ▷ row indicates global element number
   - ▷ first column contains element number and the successive three columns contain node number, given in counter clockwise order

   (1^{st} node : 2^{nd} node : 3^{rd} node) [3I15]

5. Depth of still water :
   - ▷ row indicates global element number

   (water depth) [F15.7]

6. Outward normal angle at the boundary node :
   - ▷ row indicates global node number
   - ▷ unit in radian

   (normal angle) [F15.7]

7. Identification table of boundary element for solving u :
   - ▷ row indicates global element number
   - ▷ 0 = element does not touch the boundary, 1 = element touch the boundary

   (0 *or* 1) [I15]

8. Identification table of boundary element for solving v :
   - ▷ row indicates global element number

▷ 0 = element does not touch the boundary,
1 = element touch the boundary
(0 *or* 1) [I15]

9. Identification table of local node for solving u :
▷ row indicates global node number
▷ $1^{st}, 2^{nd}$,and,3^{rd} column indicates
$1^{st}, 2^{nd}$,and,3^{rd} local node, respectively
▷ 0 = node does not touch the boundary,
1 = node touch the boundary
(0 *or* 1 : 0 *or* 1 : 0 *or* 1) [3I15]

10. Identification table of local node for solving v :
▷ row indicates global node number
▷ $1^{st}, 2^{nd}$,and,3^{rd} column indicates
$1^{st}, 2^{nd}$,and,3^{rd} local node, respectively
▷ 0 = node does not touch the boundary,
1 = node touch the boundary
(0 *or* 1 : 0 *or* 1 : 0 *or* 1) [3I15]

11. Sequence of boundary node where u is solved :
(global node number) [I15]

12. Sequence of boundary node where v is solved :
(global node number) [I15]

Example

```
1.      10
2.      10
3.  -1.0000  -1.0000
     1.0000  -1.0000
     1.0000   1.0000
        0.0   1.0000
        0.0      0.0
    -1.0000      0.0
    -0.1304  -1.0000
     1.0000   0.1304
    -0.5326  -0.5000
     0.5000   0.5326
4.        6        1        9
          5        2        8
          2        5        7
          7        5        9
          8        3       10
          3        4       10
          5        6        9
          1        7        9
          4        5       10
          5        8       10
5.     10.0
       10.0
       12.0
       12.0
       12.0
        8.0
        8.5
       10.0
       10.0
       12.0
6.    392.70
       5.4978
       0.7854
       2.3562
       2.3562
       2.3562
       4.7124
       0.0000
```

0.0000
0.0000

7. 1
0
1
1
1
1
0
1
0
0

8. 1
1
1
1
1
1
1
0
1
1

9. 0 1 0
0 0 0
0 0 1
1 0 0
0 1 0
1 0 0
0 0 0
1 1 0
0 0 0
0 0 0

10. 1 0
1 1 0
1 1 1
0 1 0
1 0 0
0 1 0
1 1 0
0 0 0
1 1 0
1 1 0

5 Numerical Results

In present numerical simulations two different types of finite element mesh are used. One is the structured three node triangular element and the other is the structured four node rectangular element. Figure 4 shows the sketch of these meshes and denotes the definition of Δx and Δy.

5.1 Solitary wave propagation over constant depth

The small amplitude solitary wave can propagate over a long distance without changing shape. The present numerical scheme is first tested for this case. To avoid potential complications caused by the boundary conditions, the theoretical surface profile and the corresponding velocity field for a solitary wave are used as the initial conditions.

The approximate solitary wave solution of Nwogu's (1993) extended Boussinesq equations was derived by Wei and Kirby (1995),

$$\eta = A_1 \, sech^2 \left[B(x - \tilde{c}t)\right] + A_2 \, sech^4 \left[B(x - \tilde{c}t)\right] \tag{124}$$

$$u = A \, sech^2 \left[B(x - \tilde{c}t)\right] \tag{125}$$

where

$$\tilde{c} = \sqrt{(gh_o)}\, c \tag{126}$$

$$A_1 = \frac{h_o}{3}\left(\frac{c^2 - 1}{C_6 - C_5 c^2}\right) \tag{127}$$

$$A_2 = -\frac{h_o}{2}\left(\frac{c^2 - 1}{c}\right)^2 \left(\frac{C_6 + 2C_5 c^2}{C_6 - C_5 c^2}\right) \tag{128}$$

$$A = \sqrt{gh_o}\left(\frac{c^2 - 1}{c}\right) \tag{129}$$

$$B = \frac{1}{2h_o}\sqrt{\left(\frac{c^2 - 1}{C_6 - C_5 c^2}\right)} \tag{130}$$

The parameter c is decided by solving

$$2C_5(c^2)^3 - \left(3C_5 + \frac{1}{3} + 2\epsilon C_5\right)(c^2)^2 + 2\epsilon C_6(c^2) + C_6 = 0 \tag{131}$$

The computational domain is made large enough that both the free surface displacement and the velocity vanish at the boundary throughout the entire numerical simulation.

Figure 5 shows snap shots of the solitary wave with amplitude 0.1 m over constant depth of 1 m. The crest of the initial solitary wave is located at $x = 0$.

Therefore, at the moment shown in Figure 5 (third one), the wave has traveled a distance close to five hundred water depth. In the numerical computations rectangular element of $\Delta x = \Delta y = 0.5(m)$, the total number of element in x axis (nx) = 1000, in y axis (ny) = 4, and $\Delta t = 0.05(sec)$ are used. The 'wavelength', λ, is defined as the width under the solitary wave where $\eta/h_o \geq 0.001$ (Goring 1999). It is estimated as 30.3 m and the corresponding 'wave period' (T) is calculated from the linear dispersion relation as $9.2sec$. There are roughly 60 elements within the solitary wave. Because the wave amplitude is quite small, the numerical results are almost identical to the theoretical solution, which is also plotted in Figure 5.

For a larger solitary wave with 0.3 m amplitude, a slight phase error appears (Figure 6). The phase speed is slightly smaller than the theoretical one and the maximum amplitude is also slightly over-predicted. This result agrees with other numerical solutions (Wei and Kirby 1995; Walkley and Berzins 1999; Li *et al.* 1999).

5.2 Solitary wave shoaling on slopes

Numerical simulations for the shoaling of a non-breaking solitary wave over plane slope are performed. Through this analysis, the nonlinear portion of the present numerical model can be examined. The test case chosen here is the same as the one studied by Wei *et al.* (1995).

The crest of the initial solitary wave is located at $x = 0$, where the beach slope (1:35) begins. The water depth is 0.71 m at $x/h_0 = 10$ and 0.2 m at $x/h_0 = 28$. The incident wave height is $\epsilon = 0.2$. In numerical computations, rectangular elements of $\Delta x = \Delta y = 0.1(m)$, nx = 500, ny = 5, and $\Delta t = 0.02(sec)$ are used. As shown in Figure 7, the present numerical solutions agree well with that of Nwogu's (1993) weakly nonlinear models in terms of wave amplitude and the free surface shape. The dimensionless time (t') and coordinate (x') have been scaled by $\sqrt{(h_0/g)}$ and h_0, respectively.

5.3 Propagation of deep water wave

A numerical experiment is performed to evaluate the ability of simulating the propagation of periodic waves in deep water. The sinusoidal wave with wavelength 2 m, wave height 0.1 m is given as an initial condition over the constant water depth of 1 m. Here, rectangular elements of $\Delta x = \Delta y = 0.1(m)$, nx = 1000, ny = 4, and $\Delta t = 0.02(sec)$ are used. The rightmost 1/4 wavelength of the initial condition are tapered off using $a\ sech^2(0.5kx)$ to avoid the abrupt changes of the water surface at the edge. Since $kh = 3.14$ in this case, the conventional Boussinesq equations are not the appropriate model for its dispersion relation does not converge if $kh > 3.016$.

Figure 8 shows the spatial profiles of the propagating waves at different instances. The vertical line denotes the location of a wave crest at different time according to the exact phase speed calculated from the linear dispersion relationship. The phase speed of the present model agrees very well with the exact phase speed.

5.4 Applications of the boundary conditions

The incident wave boundary and the perfect reflecting wall boundary condition are implemented in a simple wave tank. To check the accuracy of the reflected wall boundary condition, a solitary wave is set free to propagate between two perfectly reflecting walls. (Figure 9) The initial solitary wave of $\epsilon = 0.1$ is given with the crest at $x/h_0 = 0$. The computational domain is $0 \leq x/h_o \leq 20$. In this computation, rectangular elements of $\Delta x = \Delta y = 0.25(m)$, nx = 80, ny = 5, and $\Delta t = 0.2(sec)$ are used.

Wave maker boundary condition is applied at the left hand side and a sponge layer is used as an energy absorbing device on the right hand side boundary (Figure 10). The sinusoidal wave of amplitude $0.023m$, wave period 1 sec wave is generated over constant water depth of $0.45m$. Rectangular elements of $\Delta x = \Delta y = 0.1(m)$, nx = 400, ny = 5, and $\Delta t = 0.02(sec)$ are used. In this experiment, the sponge layer length is set to $10(m)$ and the damping coefficient of $G_1^{\eta} = 0.25$, $G_1^{u1} = 10$, $G_1^{u2} = 0.5$, and $G_2^{\eta} = G_2^{u1} = G_2^{u2} = 2$ are used. The numerical model predicts the general features of incident waves and damping waves reasonably well. However, small element-size oscillations appear near the wave maker boundary during the initial stage. Once they are generated, these high frequency waves seem to persist throughout the whole computation since the present model does not have any dissipation mechanism. For the first $\frac{1}{4}$ wave period, the input wave shape are tapered off to avoid the abrupt change of free surface. During the initial transient period, the input wave velocity, which is given from linearized equation, is not accurate enough. The inaccuracy generates small wiggles. These oscillations are dissipated effectively in the sponge layer.

5.5 Wave evolution in a rectangular basin

The two-dimensional model involves mixed derivative terms with respect to x and y which do not appear in the one-dimensional model. To verify the correctness of the numerical model implementation, wave propagation in a square basin is studied and numerical results are compared with analytic solutions. The computational domain of $0 \leq x \leq 15(m)$, $0 \leq y \leq 15(m)$, and structured uniform triangular elements are used. Here, $\Delta x = \Delta y = 0.1(m)$, $\Delta t = 0.02(sec)$ are used so that nx = ny = 150. Water depth of 0.45 m and surface elevation of Gaussian shape

$$\eta_o = 0.045\ e^{-2[(x-7.5)^2+(y-7.5)^2]} \tag{132}$$

is given as an initial condition. The initial velocity is set to zero over the whole domain. The initial surface profile is axisymmetric about the center at $x = y = 7.5(m)$ with the maximum wave height of 0.045 (m). Due to the gravitational forcing, waves propagate out of the center. The axisymmetry of the propagating wave about the origin ($x = y = 7.5m$) is shown clearly (Figure 11). This verifies that the cross-derivative terms are being implemented correctly in the model. Before the wave hits the boundary, the linear analytic solution and numerical results at several points (x=y=4.5, 6.0, 7.5 (m)) are compared (Figure 12). For the linear model, the numerical solutions are almost identical to the analytic solution. Due to the nonlinear terms, the effect of wave steepening, and faster arrival of leading wave can be seen clearly. By adding the dispersive terms, it is clear that the wave becomes more oscillatory, which is consistent with the water wave theory.

Secondly, the same numerical basin is tested for the treatment of sponge layer. In front of each wall, there exists a $3m$-thick sponge layer. In this experiment, $G_1^{\eta} = 0.2$, $G_1^{u1} = 10$, $G_1^{u2} = 0.5$, and $G_2^{\eta} = G_2^{u1} = G_2^{u2} = 3$ are used. For this specific case, we treat equation (121) $\sim$ (123) in one-dimensional way. For example, in the region (A) in Figure 13, $\mathbf{x}_e \equiv (15, 0), \mathbf{x}_s \equiv (12, 0)$ and only x-component of $\mathbf{x}$ is used. Similarly, for Region (C), $\mathbf{x}_e \equiv (0, 0), \mathbf{x}_s \equiv (3, 0)$, x-component of $\mathbf{x}$, for region (B), $\mathbf{x}_e \equiv (0, 15), \mathbf{x}_s \equiv (0, 12)$, y-component of $\mathbf{x}$, and for region (D), $\mathbf{x}_e \equiv (0, 0), \mathbf{x}_s \equiv (0, 3)$, y-component of $\mathbf{x}$ are used.

It is founded that the Newtonian cooling terms plays an major role in damping mechanism. As we can see in Figure 14, waves propagating from the origin can be effectively damped out through those sponge layers. This verifies the possibility of using sponge layer as an open boundary condition or an absorbing boundary.

Thirdly, reflective wall boundary conditions are applied at each wall (Figure 15). Here, the computation basin is 9m by 9m and rectangular element of $\Delta x = \Delta y = 0.2(m)$ and $\Delta t = 0.05(sec)$ is used. The origin of Gaussian hump is located at $x = y = 4.5(m)$. The initial wave propagate from the center and reflected back to the domain by four side walls.

By simulating this test case, we are able to check the stability of the numerical model associated with boundary condition. It is interesting to see how the corner boundary respond to the higher harmonic waves which is generated as time goes on. We ran the model until simulation time reaches 30 minute, which correspond to 36000 time step. The maximum iteration number was 5, indicating that the present model is stable.

The axisymmetry is shown clearly, which implies the obliquely incident wave as well as normally incident wave to the wall are treated properly in the numerical model. This symmetry can be an efficient way to check the possible coding error for the 2-dimensional model.

Also, we checked the conservative property of mass and energy. It is founded that there is no loss or gain of mass and energy.

5.6 Wave propagation over an elliptic shoal

We apply the 2D FEM model for the wave propagation over a shoal. The experiment conducted by Berkhoff *et al.* (1982) has been used by many researchers for verifying the accuracy of their numerical models. The conventional Boussinesq equation model cannot be applied to this case since the relatively deep water wave condition is used (kh=1.9).

The bathymetry is shown in Figure 16, which is a combination of an elliptic shoal and a plane beach with a constant slope 1 : 50 at an angle of 20^o to the y-axis. The computational domain is $[-10 \leq x \leq 10] \times [-15 \leq y \leq 25](m)$, in which a rectangular element of $\Delta x = \Delta y = 0.2(m)$, and nx = 100, ny = 200 is used. Detailed information of the geometry is shown below.

The slope-oriented coordinates (x', y') are related to the computational coordinate (x, y) in such a way that:

$$x' = cos(20)x - sin(20)y \tag{133}$$

$$y' = sin(20)x + cos(20)y \tag{134}$$

The origin $(x', y') = (0, 0)$ corresponds to the center of the shoal. The slope is defined as

$$h_{slope}(x, y) = \begin{cases} 0.45 & : \quad y' \leq -5.82 \\ 0.45 - 0.02(5.82 + y') & : \quad y' > -5.82 \end{cases}$$

the boundary of the elliptic shoal is given by,

$$\left(\frac{x'}{3}\right)^2 + \left(\frac{y'}{4}\right)^2 = 1 \tag{135}$$

and the depth in the shoal region is modified by,

$$h(x, y) = h_{slope}(x, y) + 0.3 - 0.5\left[1 - \left(\frac{x'}{5}\right)^2 - \left(\frac{y'}{3.75}\right)^2\right]^{\frac{1}{2}} \tag{136}$$

Wave maker boundary is located at $y = -15$, solid walls at $x = -10, 10$, and sponge layer at $17 \leq y \leq 25$. As a first step, to see the general pattern of wave refraction and focusing, a sinusoidal wave of amplitude 2.32cm, period 1 sec is given as an initial condition at x= -5 m. As we can see in Figure 17, wave transformation due to the shoal seems reasonable. A quantitative comparison between numerical results and experimental data will be performed.

6 Concluding Remarks

In this progress report, a new two-dimensional finite element method is formulated for the extended Boussinesq equations describing weakly nonlinear and weakly dispersive waves. The choice of the auxiliary variable for the treatment of the third order spatial variables in the governing equations is decided with the consideration of computational cost, boundary treatment and the possibility of extension to include higher order nonlinear terms. Several different types of boundary conditions have been considered, including the perfect reflecting boundary, total absorbing boundary (sponge layer) and the incident wave boundary condition. Several numerical examples have been presented and good agreements between present numerical results and existing analytical and other numerical solutions are obtained. Future work will be forced on the treatment of other types of boundary conditions, such as the partially reflective boundary, and different dissipative mechanism. The future investigations will also be focused on the harbor oscillations with different geometry.

References

[1] Alfeld, P., Piper, B., and Schumaker, L. L. 1987 "An explicit basis for C^1 quartic bivariate splines." *SIAM J. Numer. Anal.*, **24**(4): 891-911.

[2] Beji, S. and Nadaoka, K. 1996 "A formal derivation and numerical modeling of the improved Boussinesq equations for varying depth," *Ocean Engng.*, 23(8), pp. 691-704.

[3] Berkhoff, J. C. W., Booy, N. and Radder, A.C., 1982, "Verification of numerical wave propagation models for simple harmonic linear water waves", *Coastal Engng.* 6, pp.255-279

[4] Bowers, E. C. 1977 "Harbor resonance due to set-down beneath wave groups," *J. Fluid Mech.*, 79, pp. 71-92.

[5] Carrier, G. F., Shaw, R. P. and Miyata, M. 1971 "The response of narrow mouthed harbors in a straight coastline to periodic incident waves," *J. Appl. Mech.*, 38E-2, pp. 335-344.

[6] Chen, Y. and Liu, P. L.-F. 1995 "Modified Boussinesq equations and associated parabolic models for water wave propagation," *J. Fluid Mech.*, 288, pp. 351-381.

[7] Chen, Q., Madsen, P. A., Schaffer, H. A. and Basco, D. R., 1998 Wave-current interaction based on an enhanced Boussinesq approach", *Coastal Engng.*, 33, 11-39.

[8] Elgar, S. and Guza, R. T. 1985 "Shoaling gravity waves: comparisons between field observations, linear theory and a nonlinear model", *J. Fluid Mech.*, 158, 47-70.

[9] Engelman, M. S., Sani, J. L. and Gresho, P. M. 1982 "The implementation of normal and/or tangential boundary condition in finite element codes for incompressible fluid flow", *Int. J. Numer. Methods fluids*, 2, 225-238.

[10] Gardner, L. R. T. and Gardner, G. A. 1995 " A two dimensional bi-cubic B-spline finite element: used in a study of MHD-duct flow." *Comput. Methods Appl. Mech. Engrg.*, 124, 365-375.

[11] Goring, D. G. 1978 "Tsunamis - the propagation of long waves onto a shelf", Ph.D. dissertation, California Institute of Technology, Pasadena, CA.

[12] Grilli, S. T., Subramanya, R., Svendsen, I. A. and Veeramony, J. 1994 "Shoaling of solitary waves on plane beaches",*J. Waterway, Port, Coastal and Ocean Engineering*, ASCE, 120, pp. 609-628.

[13] Israeli, M., and Orszag, S.A. 1981 "Approximation of radiation boundary conditions" J. Comp. Phys., Vol.41, No.1, pp.115-135

[14] Lapidus L., Seinfeld J. 1971 "Numerical solution of ordinary differential equations" Academic Press.

[15] Li, Y. S., Liu, S.-X., Yu, Y.-X., Lai, G.-Z. 1999 "Numerical modeling of Boussinesq equations by finite element method" *Coastal Engng.*, 37, pp. 97-122.

[16] Liu, P. L.-F., 1994 "Model equations for wave propagations from deep to shallow water," in *Advances in Coastal and Ocean Engineering*, (ed. by P. L.-F. Liu), Vol. 1, pp. 125-157.

[17] Liu, P. L.-F., Yoon, S. B. and Kirby, J. T. 1985 "Nonlinear refraction-diffraction of waves in shallow water," *J. Fluid Mech.*, 163, 185-201.

[18] Longuet-Higgins, M. S. and Stewart, R. W. 1962 "Radiation stress and mass transport in gravity waves, with applications to surf beats," *J. Fluid Mech.*, 79, pp. 71-92.

[19] Madsen, P. A., Murray, R. and Sorensen, O. R. 1991 "A new form of the Boussinesq equations with improved linear dispersion characteristics," *Coastal Engineering*, 15, pp. 371-388.

[20] Mei, C. C. and Agnon, Y. 1989 "Long-period oscillations in a harbour induced by incident short waves," *J. Fluid Mech.*, 208, pp. 595-608.

[21] Munk, W. H. 1949 "Surf beats," *Eos Trans. American Geophysical Union*, 30(6), pp. 849-54.

[22] Nwogu, O. 1993 "An alternative form of the Boussinesq equations for nearshore wave propagation," *J. Waterway, Port, Coastal and Ocean Engrg.*, 119(6), pp. 618-638.

[23] Okihiro, M. and Guza, R. T. 1996 "Observation of seiche forcing and amplification in three small harbors," *J. Waterways, Port, Coastal and Ocean Engineering*, 122, No. 5, pp. 233-238.

[24] Okihiro, M., Guza, R. T. and Seymour, R. 1993 "Excitation of seiche observed in a small harbor," *J. Geophys. Res.*, 98 (C10), pp. 18201-18211.

[25] Peregrine, D. H. 1967 "Long waves on a beach" *J. Fluid Mech.*, 27, 815-882.

[26] Pinder, G. F. and Gray, W. G. 1977 "Finite element simulation in surface and subsurface hydrology ", *Academic, New York*

[27] Sabin, M.A. 1997 "Spline finite elements." *Ph.D Thesis, University of Cambridge.*

[28] Walkley, M. and Berzins, M. 1999 "Finite element method for Boussinesq wave analysis," *Int. J. Numer. Methods Fluids*, 29, pp. 143-157.

[29] Wei, G., Kirby, J.T. 1995 "Time-dependent numerical code for extended Boussinesq equations." *ASCE J. Waterw., Port, Coast., Ocean Engr.* , 121, pp 251-261.

[30] Wei, G., Kirby, J. T., Grilli, S. T., and Subramanya, R. 1995 "A fully nonlinear Boussinesq model for surface waves. Part 1. Highly nonlinear unsteady waves," *J. Fluid Mech.*, 294, pp. 71-92.

[31] Witting, J. M. 1984 "A unified model for the evolution of nonlinear water waves", *J. Comp. Phys.*, 56, 203-236.

[32] Woo, S.-B. and Liu, P. L.-F. 2000 "A Petrov-Galerkin finite element model for one-dimensional fully nonlinear and weakly dispersive wave propagation," (submitted).

[33] Wu, J.-K. and Liu, P. L.-F. 1990 "Harbor excitations by incident wave groups," *J. Fluid Mech.*, 217, pp. 595-613.

Appendix

Let us introduce the following notations:

$$\Psi^d_{(1)j} := \frac{\partial^d \psi_j}{\partial x^d} \tag{A.1}$$

$$\Psi^d_{(2)j} := \frac{\partial^d \psi_j}{\partial y^d} \tag{A.2}$$

The superscript means the order of derivative. When d is zero, $\Psi^0_{(1)j} = \frac{d^0\psi_j}{\partial x^0} := \psi_j$ is implied. Therefore the subscript 0 and the subscript in the parenthesis will be omitted. In the following equations, $\langle\cdot\rangle$ denotes $\iint_\Omega \cdot dxdy$ and summation over the repeated index k, ℓ, and m from 1 to ND is implied. Let us define the mass matrix in (80) and (81) such as:

$$[M^u]_{ij} = [M^u_1]_{ij} + \mu^2[M^u_2]_{ij} \tag{A.3}$$

$$[M^v]_{ij} = [M^v_1]_{ij} + \mu^2[M^v_2]_{ij} \tag{A.4}$$

Then,

$$[M^\eta]_{ij} = [M^u_1]_{ij} = [M^v_1]_{ij} = [M^P]_{ij} = \langle \Psi_i \Psi_j \rangle \tag{A.5}$$

$$\begin{aligned}[M^u_2]_{ij} = &-C_4\langle \Psi_i \Psi^1_{(1)k} \Psi^1_{(1)j} \rangle (\{h\}_k)^2 - \beta \langle \Psi_i \Psi^1_{(1)k} \Psi^1_{(1)\ell} \Psi_j \rangle \{h\}_k \{h\}_\ell \\ &-C_5\langle \Psi^1_{(1)i} \Psi_k \Psi^1_{(1)j} \rangle (\{h\}_k)^2 - \frac{\beta}{2}\langle \Psi^1_{(1)i} \Psi^1_{(1)k} \Psi_j \rangle (\{h\}_k)^2\end{aligned} \tag{A.6}$$

$$\begin{aligned}[M^v_2]_{ij} = &-C_4\langle \Psi_i \Psi^1_{(2)k} \Psi^1_{(2)j} \rangle (\{h\}_k)^2 - \beta \langle \Psi_i \Psi^1_{(2)k} \Psi^1_{(2)\ell} \Psi_j \rangle \{h\}_k \{h\}_\ell \\ &-C_5\langle \Psi^1_{(2)i} \Psi_k \Psi^1_{(2)j} \rangle (\{h\}_k)^2 - \frac{\beta}{2}\langle \Psi^1_{(2)i} \Psi^1_{(2)k} \Psi_j \rangle (\{h\}_k)^2\end{aligned} \tag{A.7}$$

The forcing vectors have the following expressions:

$$\{f^\eta\}^n_i = \{f^\eta_1\}^n_i + \varepsilon\{f^\eta_2\}^n_i + \mu^2\{f^\eta_3\}^n_i \tag{A.8}$$

$$\{f^u\}^n_i = \{f^u_1\}^n_i + \varepsilon\{f^u_2\}^n_i + \mu^2\{f^u_3\}^n_i \tag{A.9}$$

$$\{f^v\}^n_i = \{f^v_1\}^n_i + \varepsilon\{f^v_2\}^n_i + \mu^2\{f^v_3\}^n_i \tag{A.10}$$

in which

$$\{f_1^\eta\}_i^n = \langle\Psi^1_{(1)i}\Psi_k\rangle\{h\}_k\{u\}_k^n + \langle\Psi^1_{(2)i}\Psi_k\rangle\{h\}_k\{v\}_k^n \tag{A.11}$$

$$\{f_2^\eta\}_i^n = \langle\Psi^1_{(1)i}\Psi_k\rangle\{\eta\}_k^n\{u\}_k^n + \langle\Psi^1_{(2)i}\Psi_k\rangle\{\eta\}_k^n\{v\}_k^n \tag{A.12}$$

$$\begin{aligned}\{f_3^\eta\}_i^n = {} & C_1\langle\Psi^1_{(1)i}\Psi_k\Psi^1_{(1)\ell}\rangle(\{h\}_k)^3\{P\}_\ell^n \\ & +C_3\Big\{\langle\Psi^1_{(1)i}\Psi_k\Psi^1_{(1)\ell}\rangle(\{h\}_k)^2\{h\}_\ell\{P\}_\ell^n \\ & \quad +\frac{1}{3}\langle\Psi^1_{(1)i}\Psi^1_{(1)k}\Psi^1_{(1)\ell}\rangle(\{h\}_k)^3\{u\}_\ell^n \\ & \quad +\langle\Psi^1_{(1)i}\Psi_k\Psi_\ell\rangle(\{h\}_k)^2\{u\}_\ell^n\{R_1\}_\ell \\ & \quad +\frac{1}{3}\langle\Psi^1_{(1)i}\Psi^1_{(2)k}\Psi^1_{(1)\ell}\rangle(\{h\}_k)^3\{v\}_\ell^n \\ & \quad +\langle\Psi^1_{(1)i}\Psi_k\Psi_\ell\rangle(\{h\}_k)^2\{v\}_\ell^n\{R_3\}_\ell\Big\} \\ & +C_1\langle\Psi^1_{(2)i}\Psi_k\Psi^1_{(2)\ell}\rangle(\{h\}_k)^3\{P\}_\ell^n \\ & +C_3\Big\{\langle\Psi^1_{(2)i}\Psi_k\Psi^1_{(2)\ell}\rangle(\{h\}_k)^2\{h\}_\ell\{P\}_\ell^n \\ & \quad +\frac{1}{3}\langle\Psi^1_{(2)i}\Psi^1_{(1)k}\Psi^1_{(2)\ell}\rangle(\{h\}_k)^3\{u\}_\ell^n \\ & \quad +\langle\Psi^1_{(2)i}\Psi_k\Psi_\ell\rangle(\{h\}_k)^2\{u\}_\ell^n\{R_3\}_\ell \\ & \quad +\frac{1}{3}\langle\Psi^1_{(2)i}\Psi^1_{(2)k}\Psi^1_{(2)\ell}\rangle(\{h\}_k)^3\{v\}_\ell^n \\ & \quad +\langle\Psi^1_{(2)i}\Psi_k\Psi_\ell\rangle(\{h\}_k)^2\{v\}_\ell^n\{R_2\}_\ell\Big\}\end{aligned} \tag{A.13}$$

$$\{f_1^u\}_i^n = \langle\Psi^1_{(1)i}\Psi_k\rangle\{\eta\}_k^n \tag{A.14}$$

$$\{f_2^u\}_i^n = \frac{1}{2}\langle\Psi^1_{(1)i}\Psi_k\rangle((\{u\}_k^n)^2 + (\{v\}_k^n)^2) \tag{A.15}$$

$$\{f_3^u\}_i^n = \langle\Psi^1_{(1)i}\Psi_k\Psi^1_{(2)\ell}\rangle(C_2(\{h\}_k)^2\{\dot{v}\}_\ell^n + \beta\{h\}_k\{h\}_\ell\{\dot{v}\}_\ell^n) \tag{A.16}$$

$$\{f_1^v\}_i^n = \langle\Psi^1_{(2)i}\Psi_k\rangle\{\eta\}_k^n \tag{A.17}$$

$$\{f_2^v\}_i^n = \frac{1}{2}\langle\Psi^1_{(2)i}\Psi_k\rangle((\{u\}_k^n)^2 + (\{v\}_k^n)^2) \tag{A.18}$$

$$\{f_3^v\}_i^n = \langle\Psi^1_{(2)i}\Psi_k\Psi^1_{(1)\ell}\rangle(C_2(\{h\}_k)^2\{\dot{u}\}_\ell^n + \beta\{h\}_k\{h\}_\ell\{\dot{u}\}_\ell^n) \tag{A.19}$$

$$\{f^P\}_i^n = \langle\Psi_i\Psi^1_{(1)k}\rangle\{u\}_k^n + \langle\Psi_i\Psi^1_{(2)k}\rangle\{v\}_k^n \tag{A.20}$$

Finally, the boundary vectors can be expressed as:

$$
\begin{aligned}
\{q^{\eta}\}_i^n &= -\mu^2 \int_\Gamma n_x \Big[(\Psi_i\Psi_k)(\{h\}_k + \{\eta\}_k^n)\{u\}_k^n + C_1(\Psi_i\Psi_k\Psi^1_{(1)\ell})(\{h\}_k)^3\{P\}_\ell^n \\
&\quad + C_3 \Big\{ (\Psi_i\Psi_k\Psi^1_{(1)\ell})(\{h\}_k)^2\{h\}_\ell\{P\}_\ell^n \\
&\quad + \frac{1}{3}(\Psi_i\Psi^1_{(1)k}\Psi^1_{(1)\ell})(\{h\}_k)^3\{u\}_\ell^n \\
&\quad + (\Psi_i\Psi_k\Psi_\ell)(\{h\}_k)^2\{u\}_\ell^n\{R_1\}_\ell \\
&\quad + \frac{1}{3}(\Psi_i\Psi^1_{(2)k}\Psi^1_{(1)\ell})(\{h\}_k)^3\{v\}_\ell^n \\
&\quad + (\Psi_i\Psi_k\Psi_\ell)(\{h\}_k)^2\{v\}_\ell^n\{R_3\}_\ell \Big\} \Big] \\
&\quad + n_y \Big[(\Psi_i\Psi_k)(\{h\}_k + \{\eta\}_k^n)\{v\}_k^n + C_1(\Psi_i\Psi_k\Psi^1_{(2)\ell})(\{h\}_k)^3\{P\}_\ell^n \\
&\quad + C_3 \Big\{ (\Psi_i\Psi_k\Psi^1_{(2)\ell})(\{h\}_k)^2\{h\}_\ell\{P\}_\ell^n \\
&\quad + \frac{1}{3}(\Psi_i\Psi^1_{(1)k}\Psi^1_{(2)\ell})(\{h\}_k)^3\{u\}_\ell^n \\
&\quad + (\Psi_i\Psi_k\Psi_\ell)(\{h\}_k)^2\{u\}_\ell^n\{R_3\}_\ell \\
&\quad + \frac{1}{3}(\Psi_i\Psi^1_{(2)k}\Psi^1_{(2)\ell})(\{h\}_k)^3\{v\}_\ell^n \\
&\quad + (\Psi_i\Psi_k\Psi_\ell)(\{h\}_k)^2\{v\}_\ell^n\{R_2\}_\ell \Big\} \Big] d\Gamma \qquad \text{(A.21)}
\end{aligned}
$$

$$
\begin{aligned}
\{q^{u}\}_i^n &= -\int_\Gamma n_x \Big[(\Psi_i\Psi_k)\{\eta\}_k^n + \varepsilon\frac{1}{2}(\Psi_i\Psi_k)((\{u\}_k^n)^2 + (\{v\}_k^n)^2) \\
&\quad + \mu^2(\Psi_i\Psi_k\Psi^1_{(1)\ell})(C_2(\{h\}_k)^2\{\dot{u}\}_\ell^n + \beta\{h\}_k\{h\}_\ell\{\dot{u}\}_\ell^n) \\
&\quad + \mu^2(\Psi_i\Psi_k\Psi^1_{(2)\ell})(C_2(\{h\}_k)^2\{\dot{v}\}_\ell^n + \beta\{h\}_k\{h\}_\ell\{\dot{v}\}_\ell^n) \Big] d\Gamma \qquad \text{(A.22)}
\end{aligned}
$$

$$
\begin{aligned}
\{q^{v}\}_i^n &= -\int_\Gamma n_y \Big[(\Psi_i\Psi_k)\{\eta\}_k^n + \varepsilon\frac{1}{2}(\Psi_i\Psi_k)((\{u\}_k^n)^2 + (\{v\}_k^n)^2) \\
&\quad + \mu^2(\Psi_i\Psi_k\Psi^1_{(1)\ell})(C_2(\{h\}_k)^2\{\dot{u}\}_\ell^n + \beta\{h\}_k\{h\}_\ell\{\dot{u}\}_\ell^n) \\
&\quad + \mu^2(\Psi_i\Psi_k\Psi^1_{(2)\ell})(C_2(\{h\}_k)^2\{\dot{v}\}_\ell^n + \beta\{h\}_k\{h\}_\ell\{\dot{v}\}_\ell^n) \Big] d\Gamma \qquad \text{(A.22)}
\end{aligned}
$$

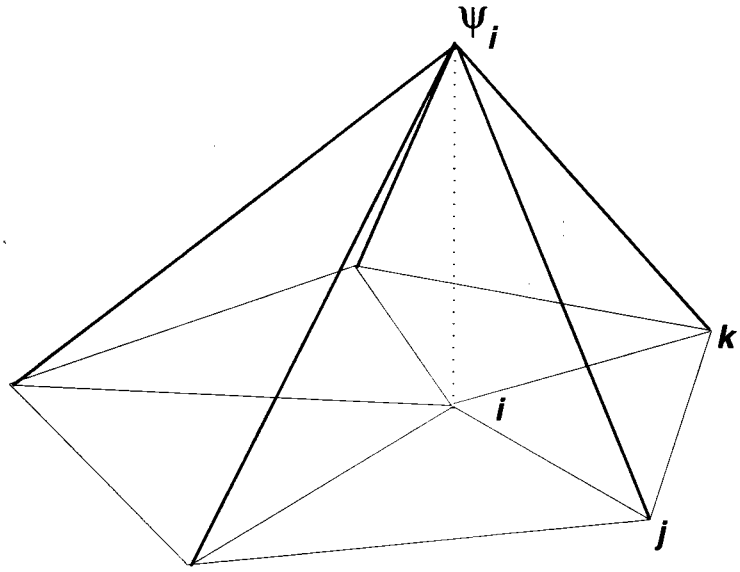

(a) Global shape function at node i

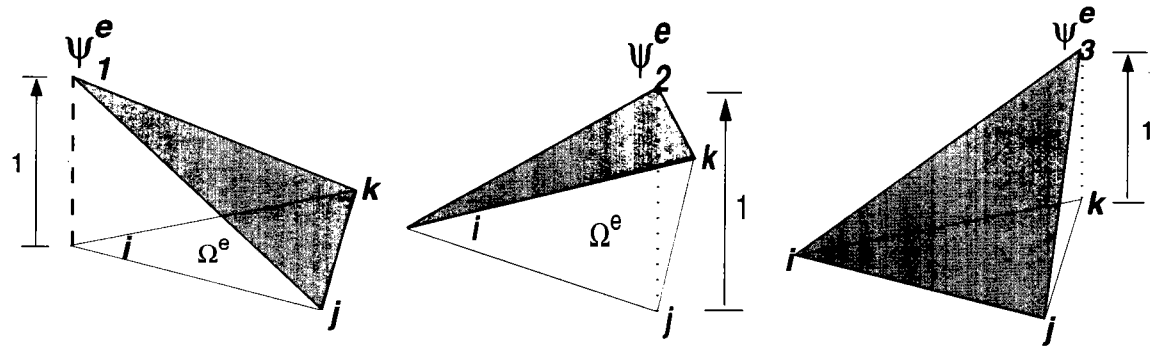

(b) Local shape function over an element Ω_e

Figure 1: Global and Local shape function

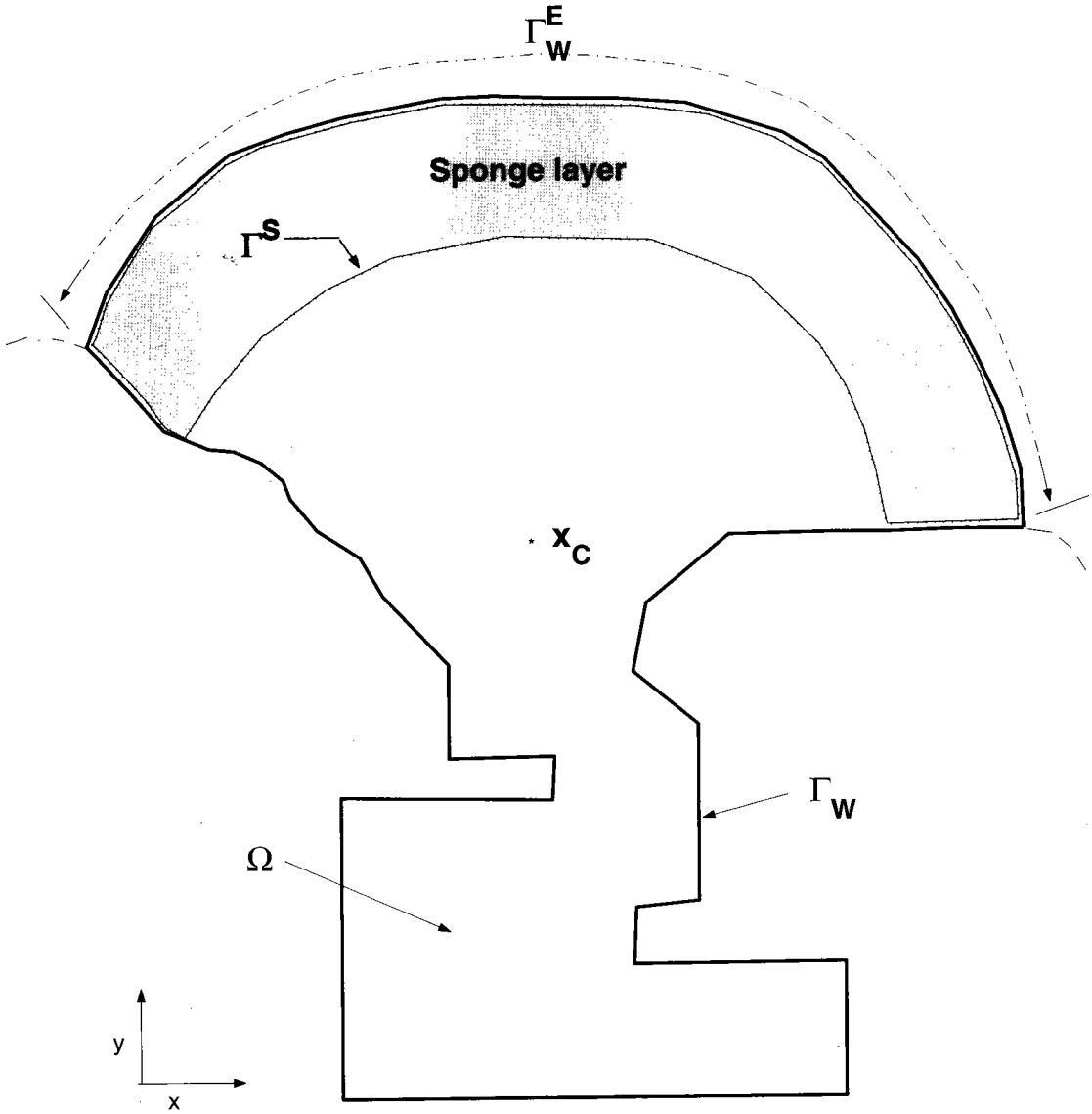

Figure 2: A rough sketch of computational domain and boundary

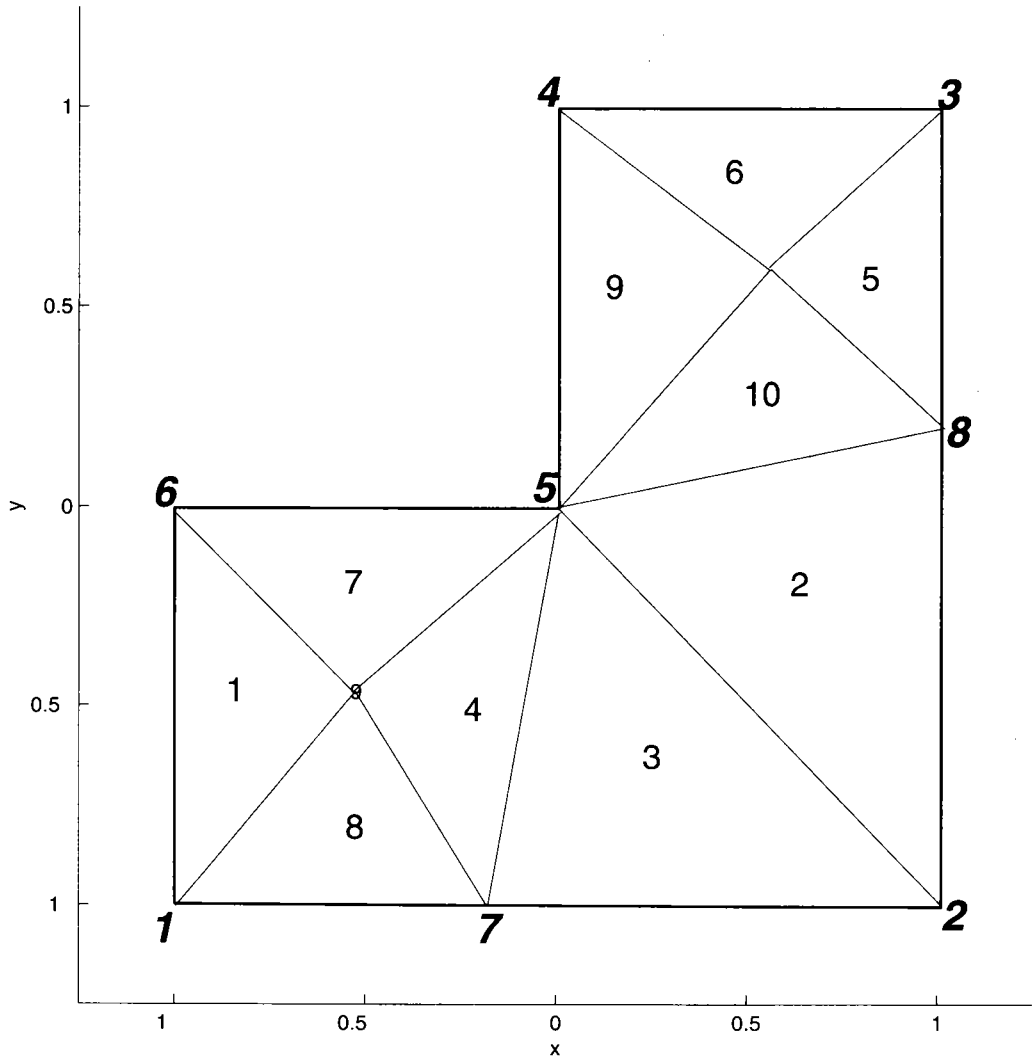

Figure 3: Example of unstructured triangular mesh

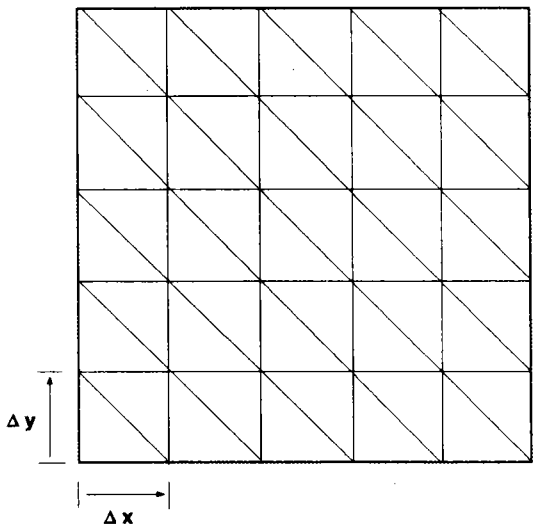

(a) Structured triangular mesh

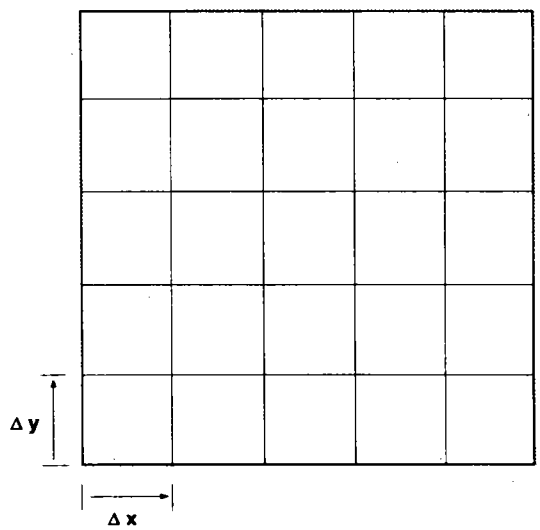

(b) Structured rectangular mesh

Figure 4: Different kind of meshes used in the model

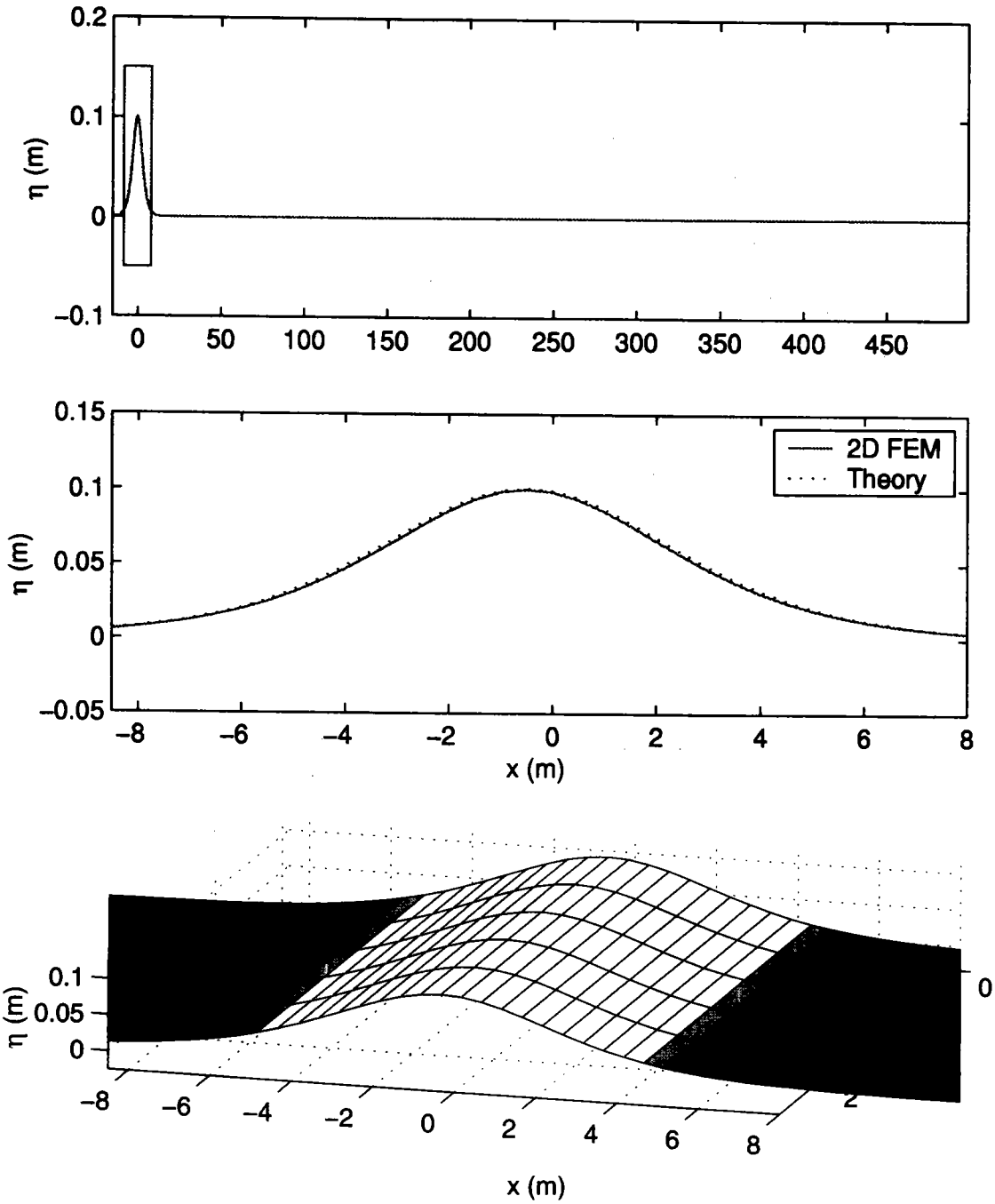

Figure 5: Comparison of numerical and theoretical solution of solitary wave propagating over constant depth at t = 0 (sec). (a/h= 0.1)

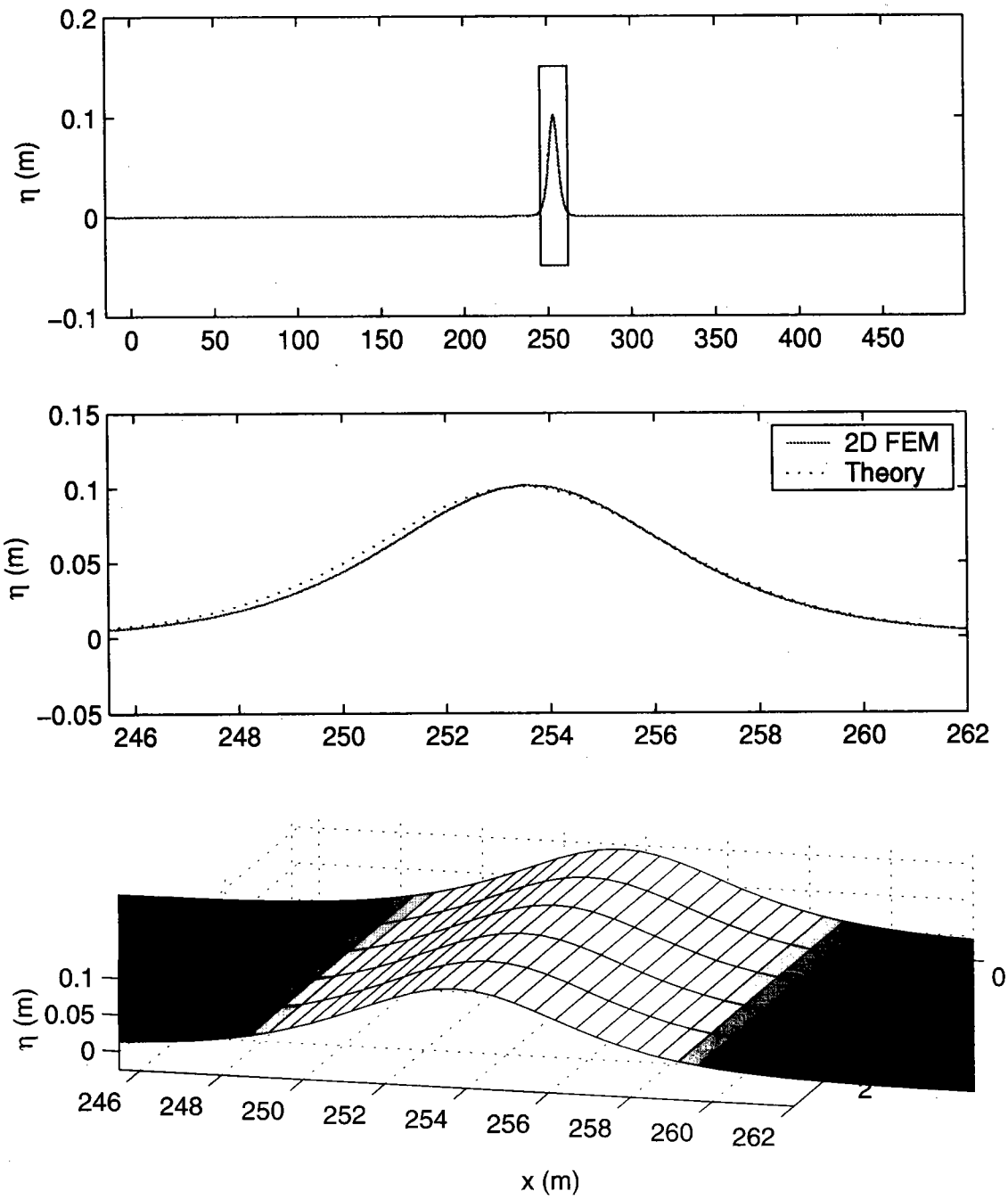

Figure 5: Comparison of numerical and theoretical solution of solitary wave propagating over constant depth at t = 77 (sec). (a/h= 0.1)

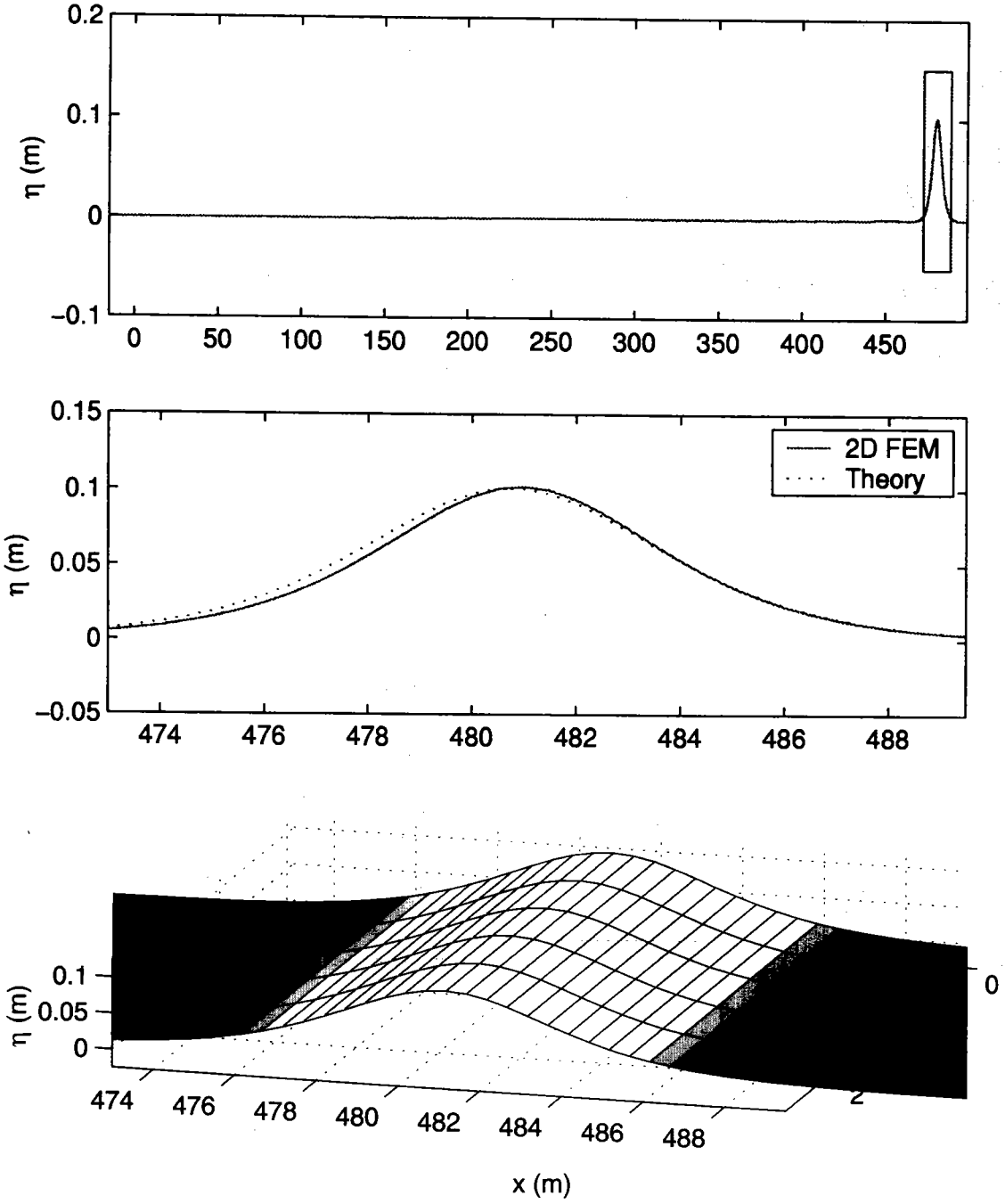

Figure 5: Comparison of numerical and theoretical solution of solitary wave propagating over constant depth at t = 146 (sec). (a/h= 0.1)

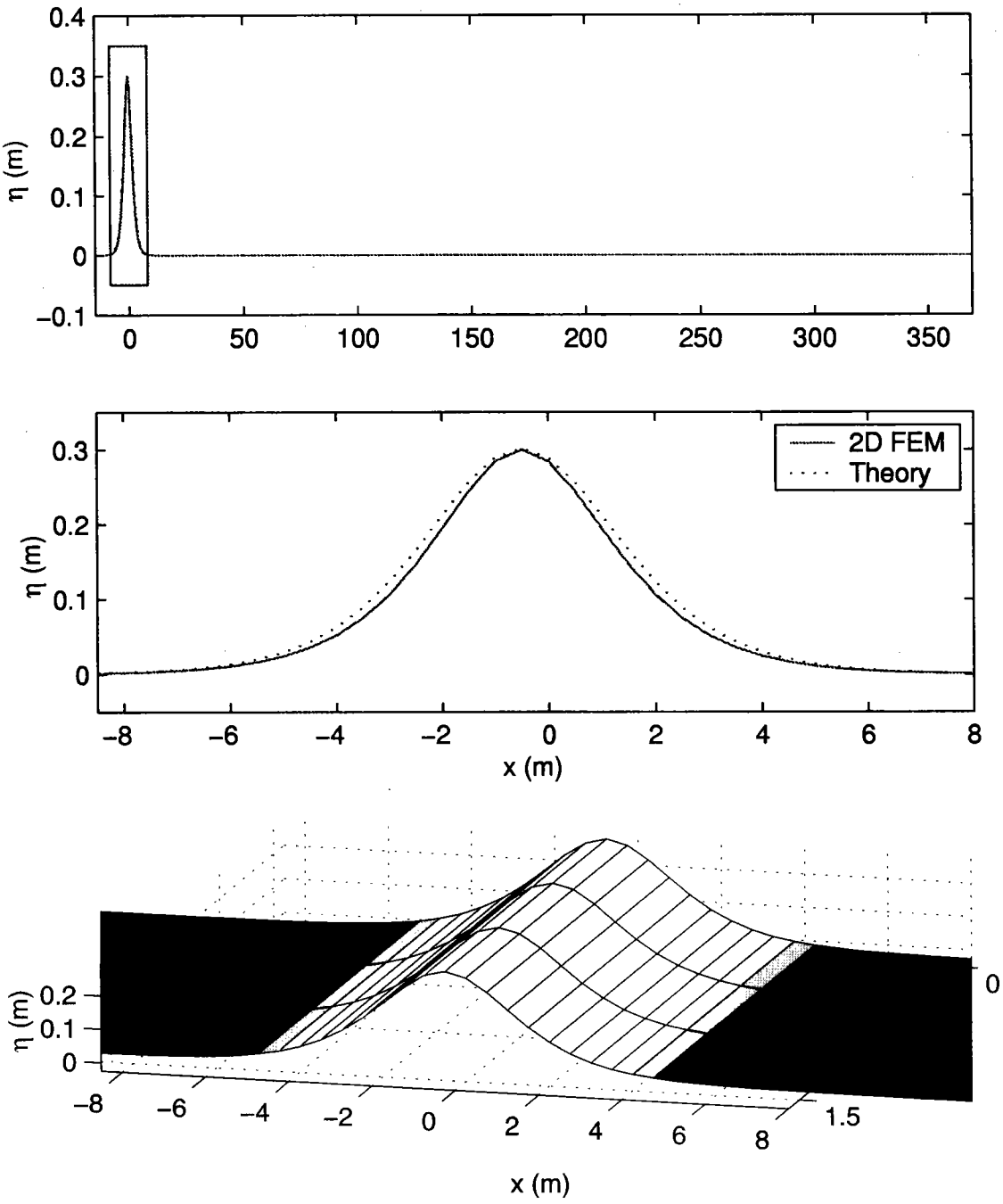

Figure 6: Comparison of numerical and theoretical solution of solitary wave propagating over constant depth at t = 0 (sec). (a/h= 0.3)

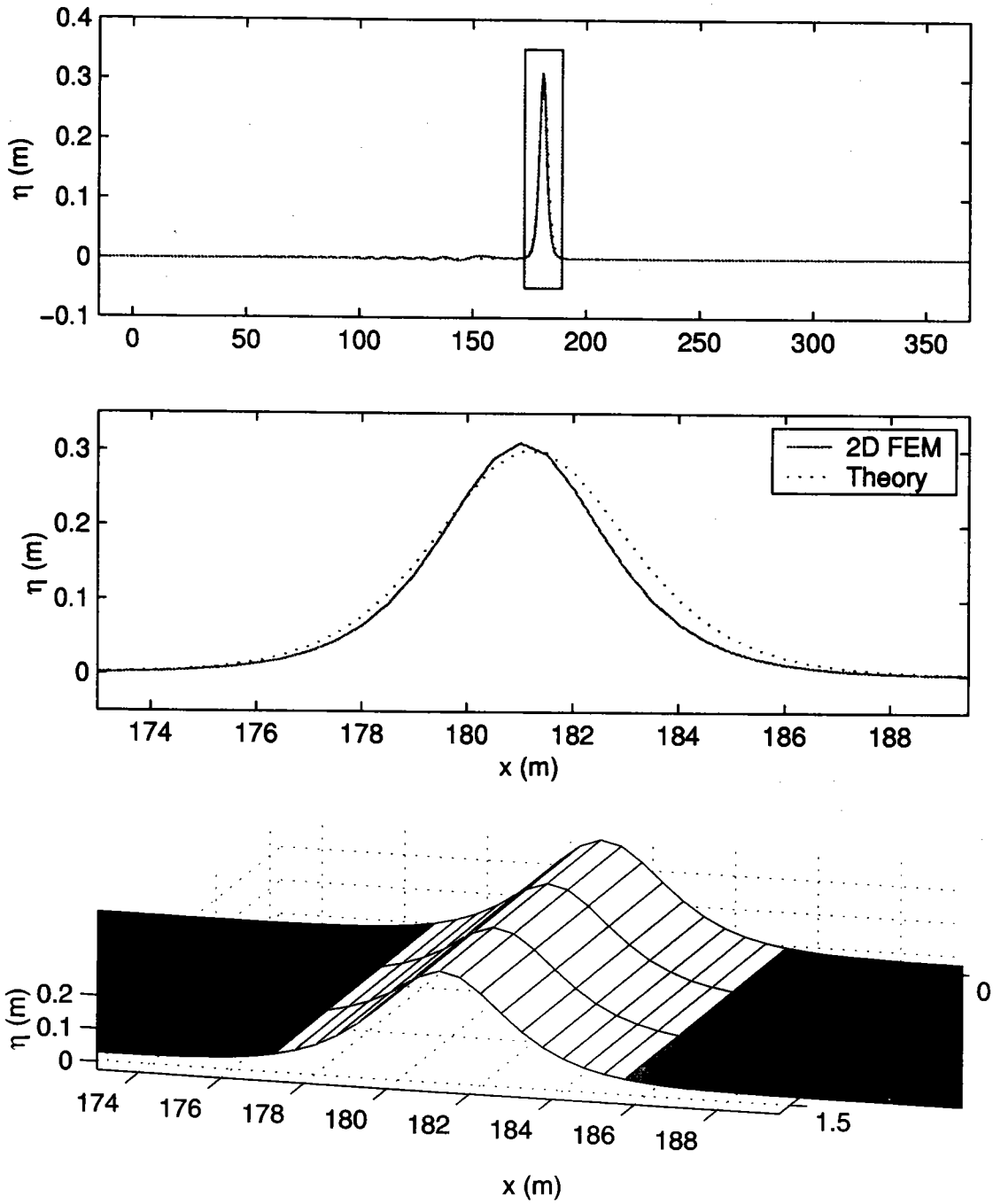

Figure 6: Comparison of numerical and theoretical solution of solitary wave propagating over constant depth at t = 50 (sec). (a/h= 0.3)

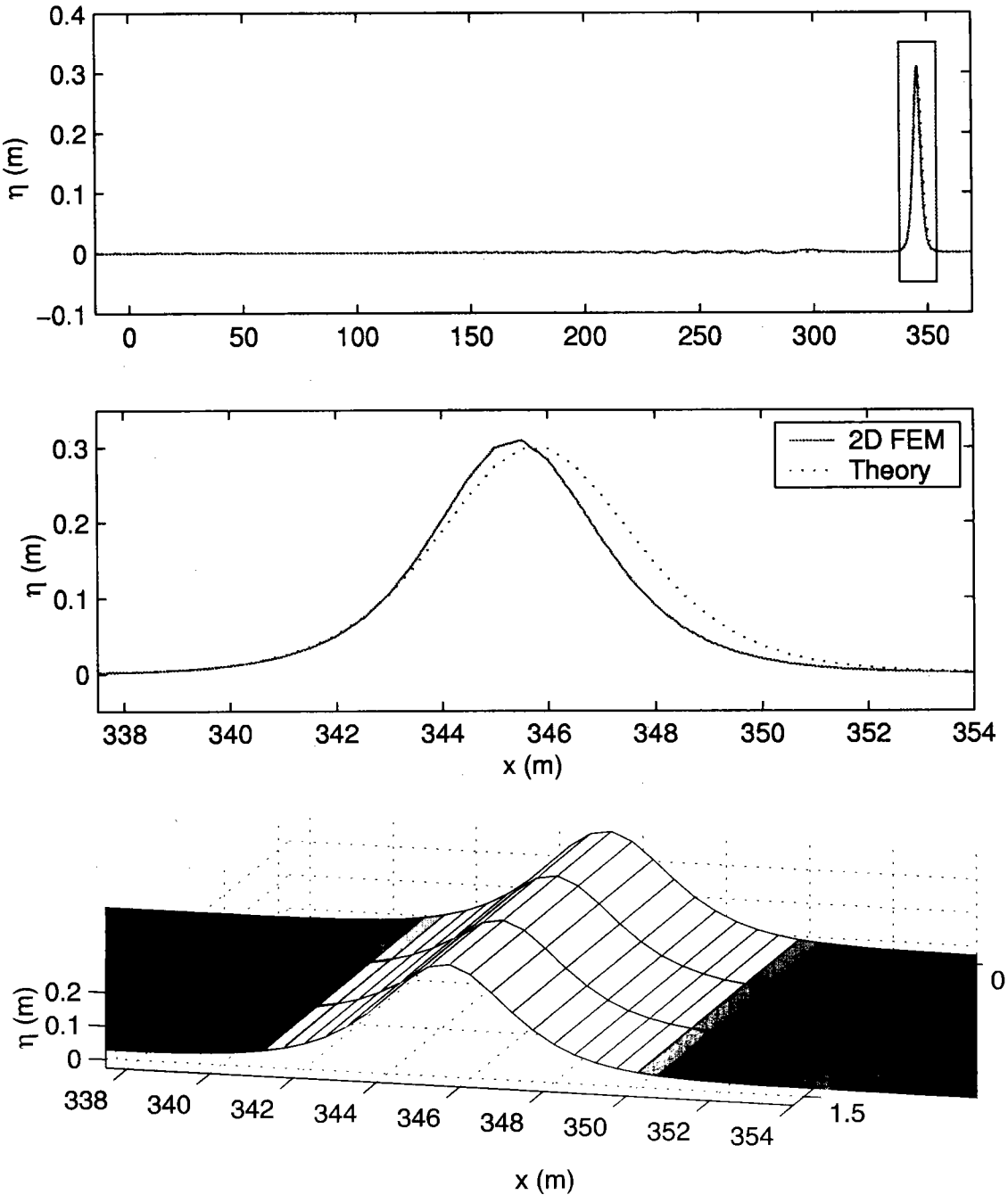

Figure 6: Comparison of numerical and theoretical solution of solitary wave propagating over constant depth at t = 97 (sec). (a/h= 0.3)

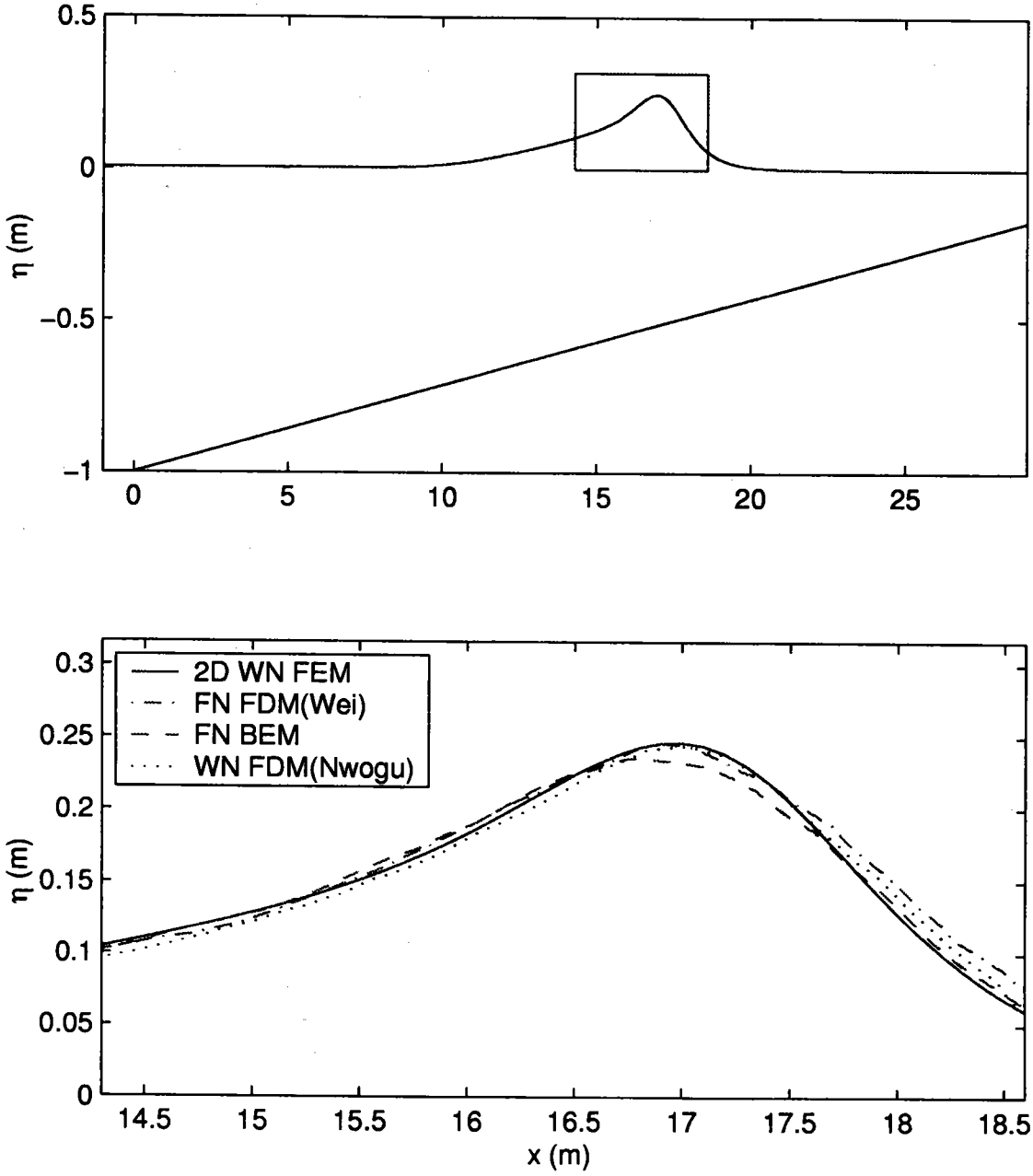

Figure 7: Numerical simulation of solitary wave shoaling on slope of 1:35 at time t = 5.18 (sec) 2D WN FEM: Present 2-dimensional FEM, FN FDM: Fully nonlinear FDM (Wei et al. 1995), FN BEM: Fully nonlinear BEM (Grilli et al. 1994), WN FDM: Weakly nonlinear FDM (Nwogu 1993)

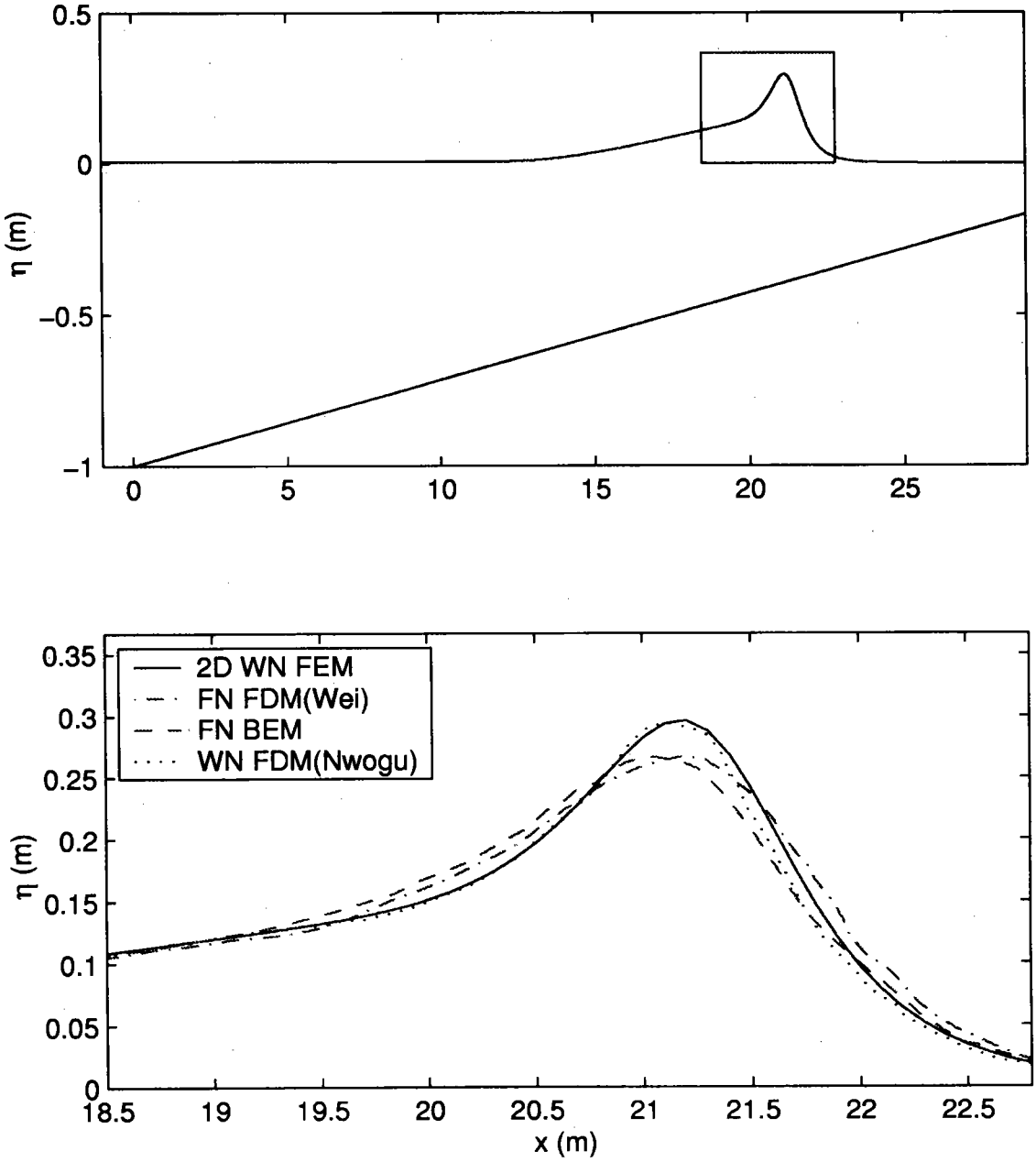

Figure 7: Numerical simulation of solitary wave shoaling on slope of 1:35 at time t = 6.59 (sec)

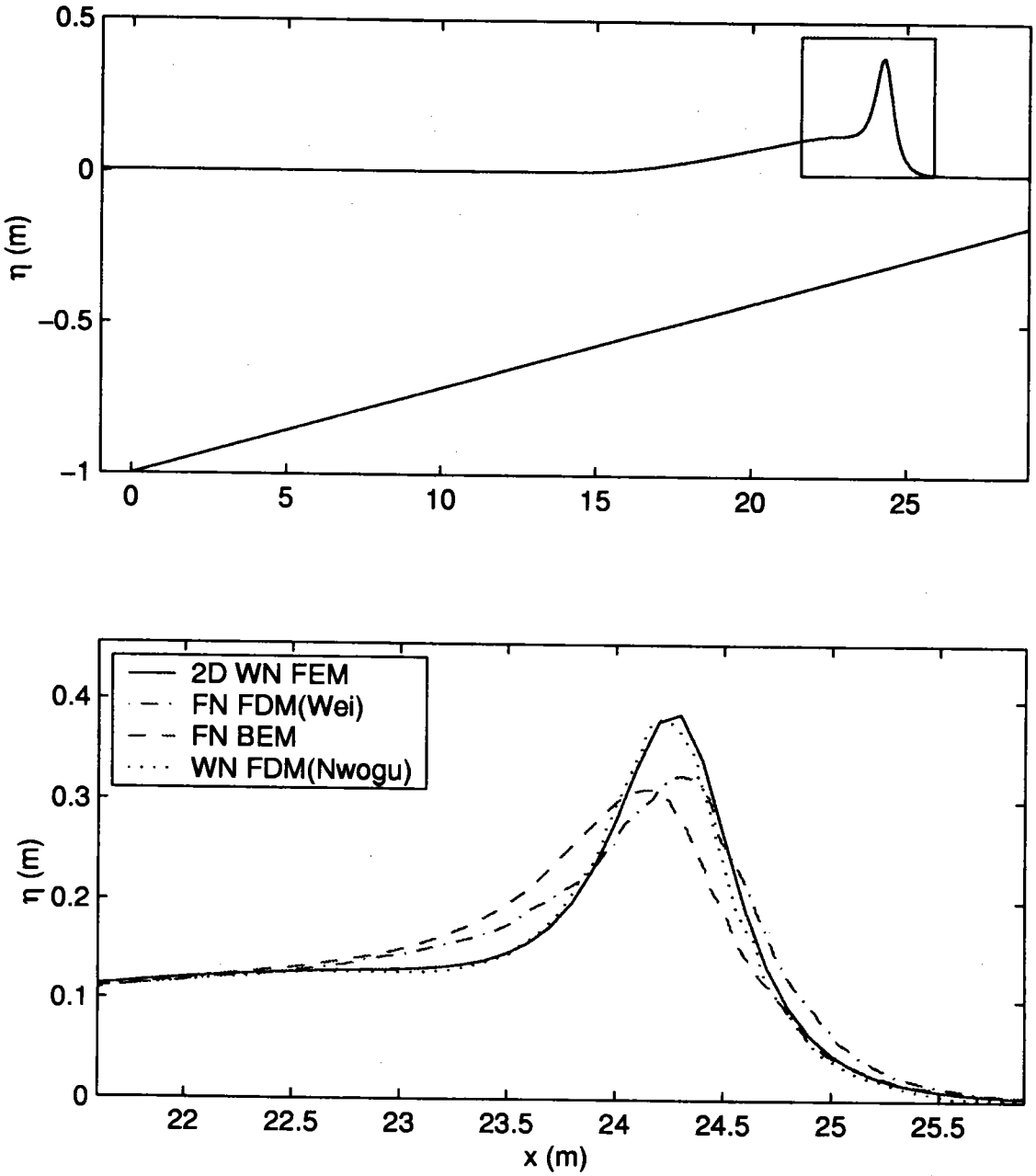

Figure 7: Numerical simulation of solitary wave shoaling on slope of 1:35 at time t = 7.68 (sec)

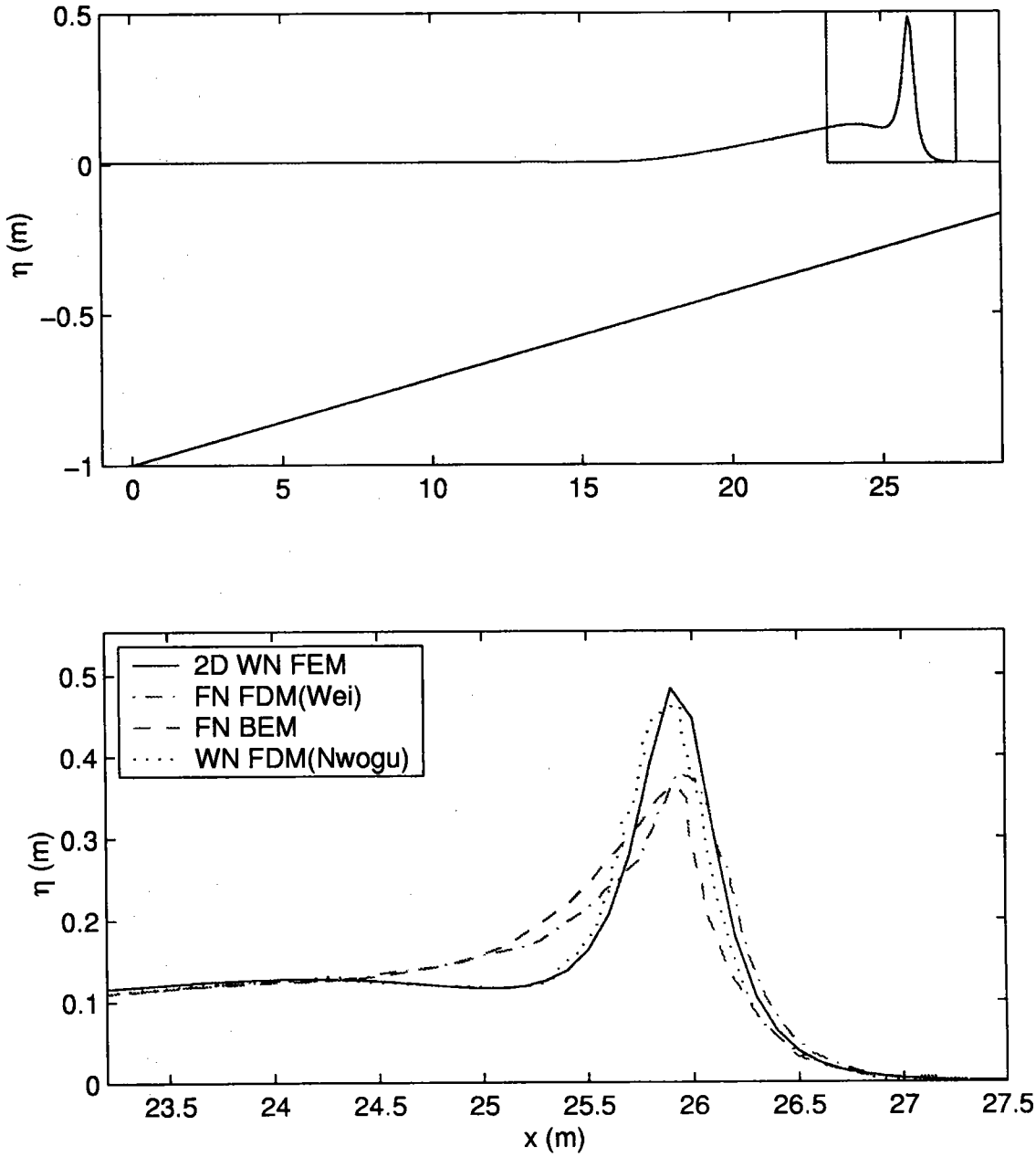

Figure 7: Numerical simulation of solitary wave shoaling on slope of 1:35 at time t = 8.28 (sec)

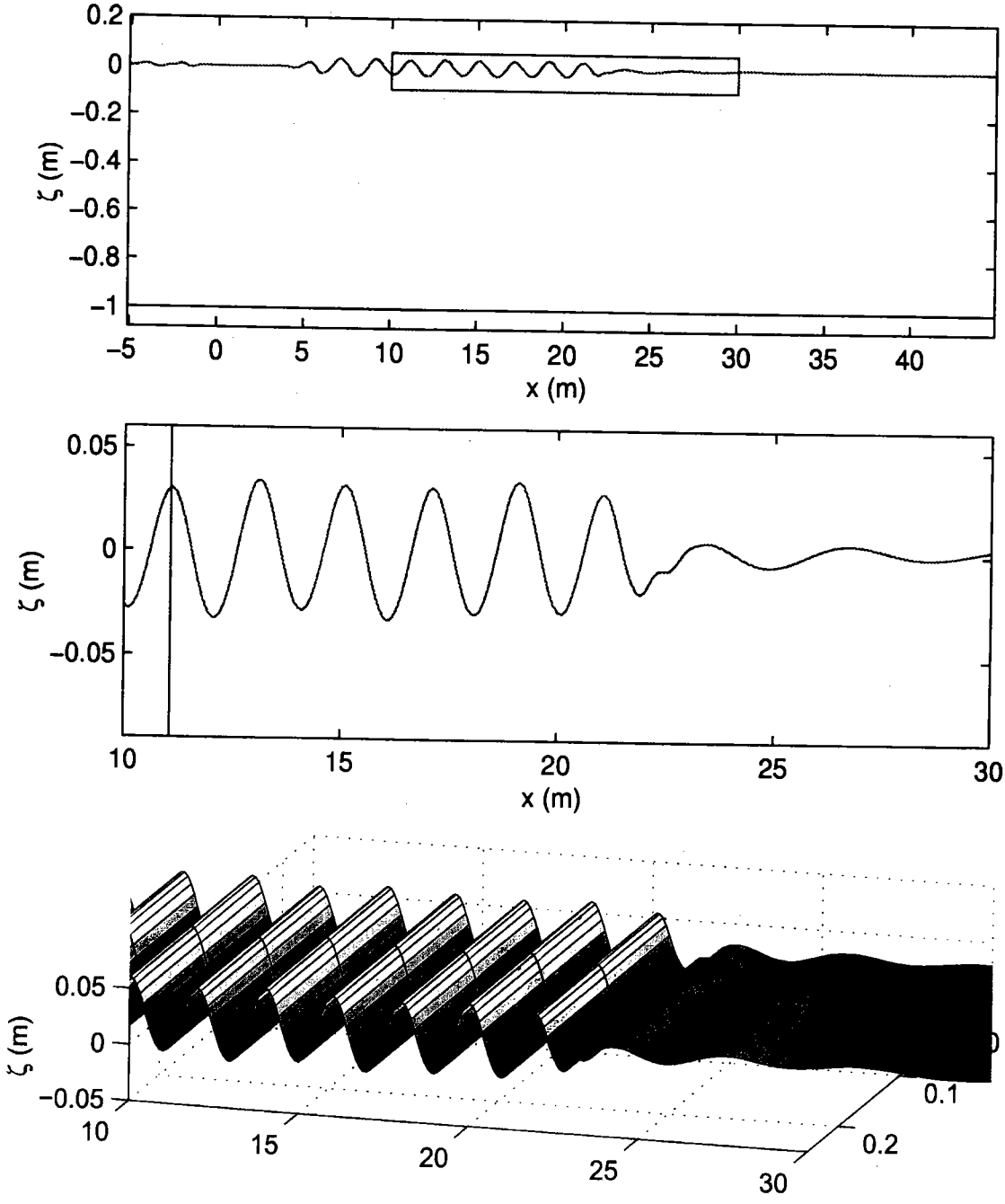

Figure 8: Propagation of deep water wave (kh = 3.14) at time t = 12 (sec)

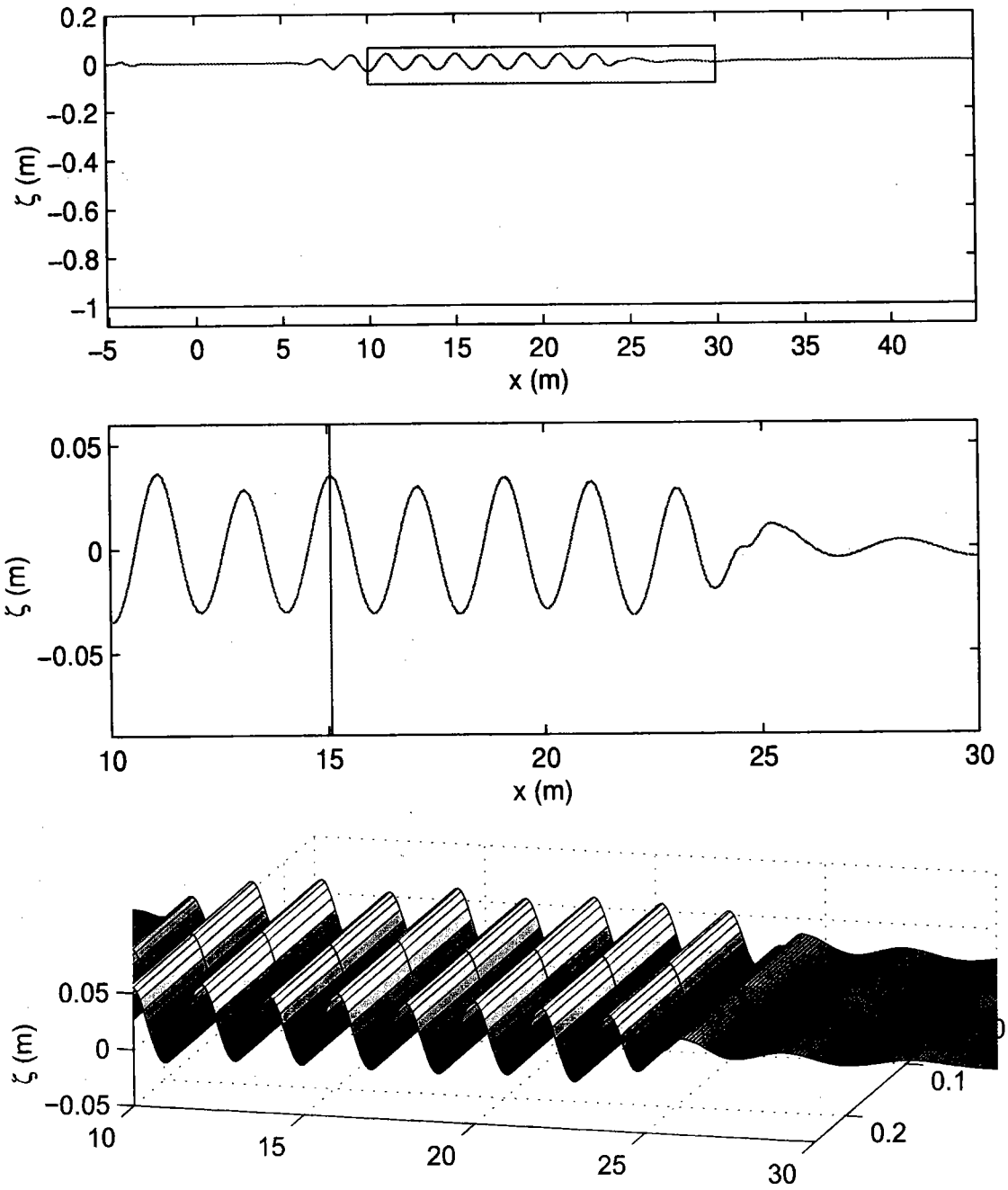

Figure 8: Propagation of deep water wave (kh = 3.14) at time t = 14.3 (sec)

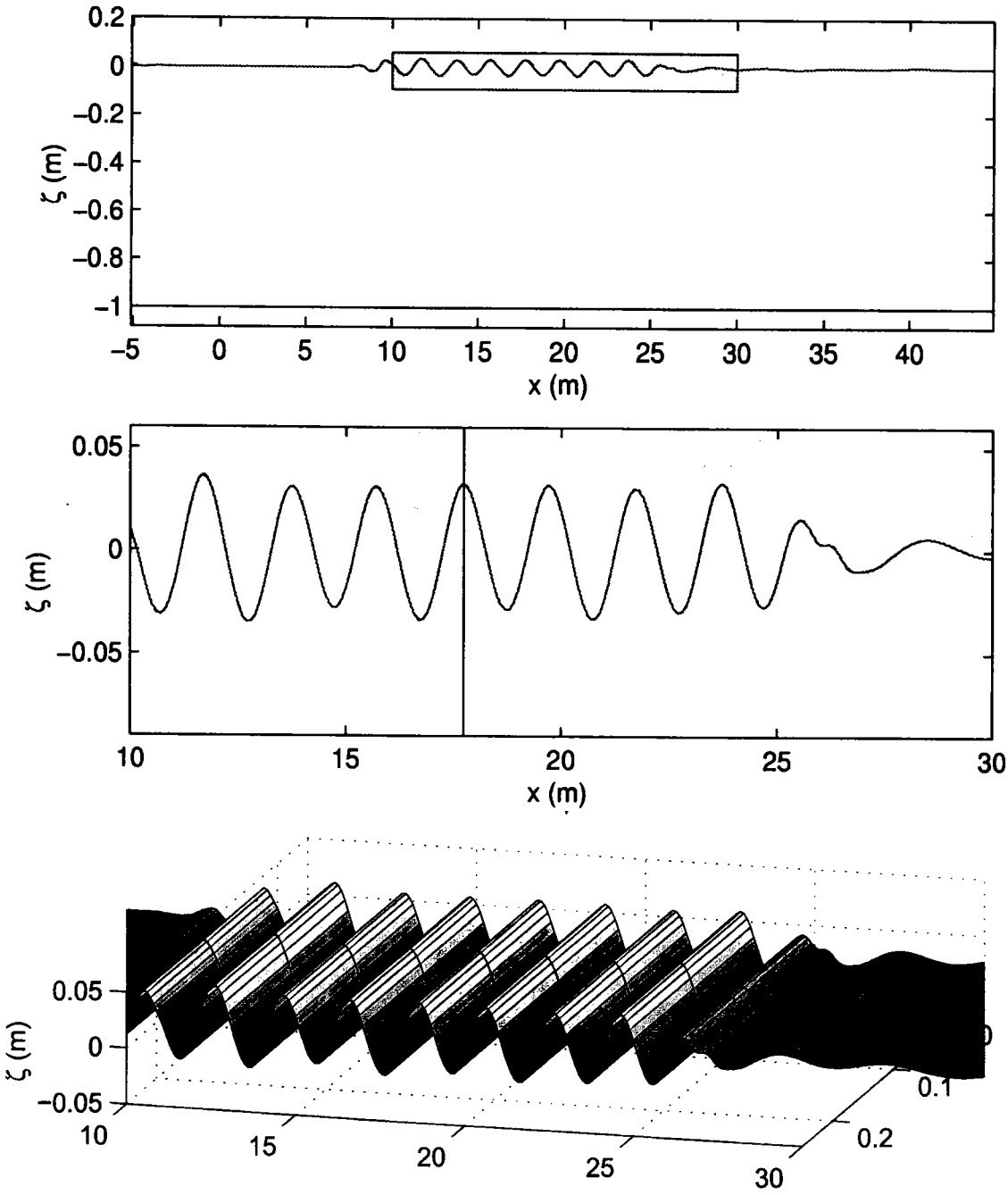

Figure 8: Propagation of deep water wave (kh = 3.14) at time t = 15.8 (sec)

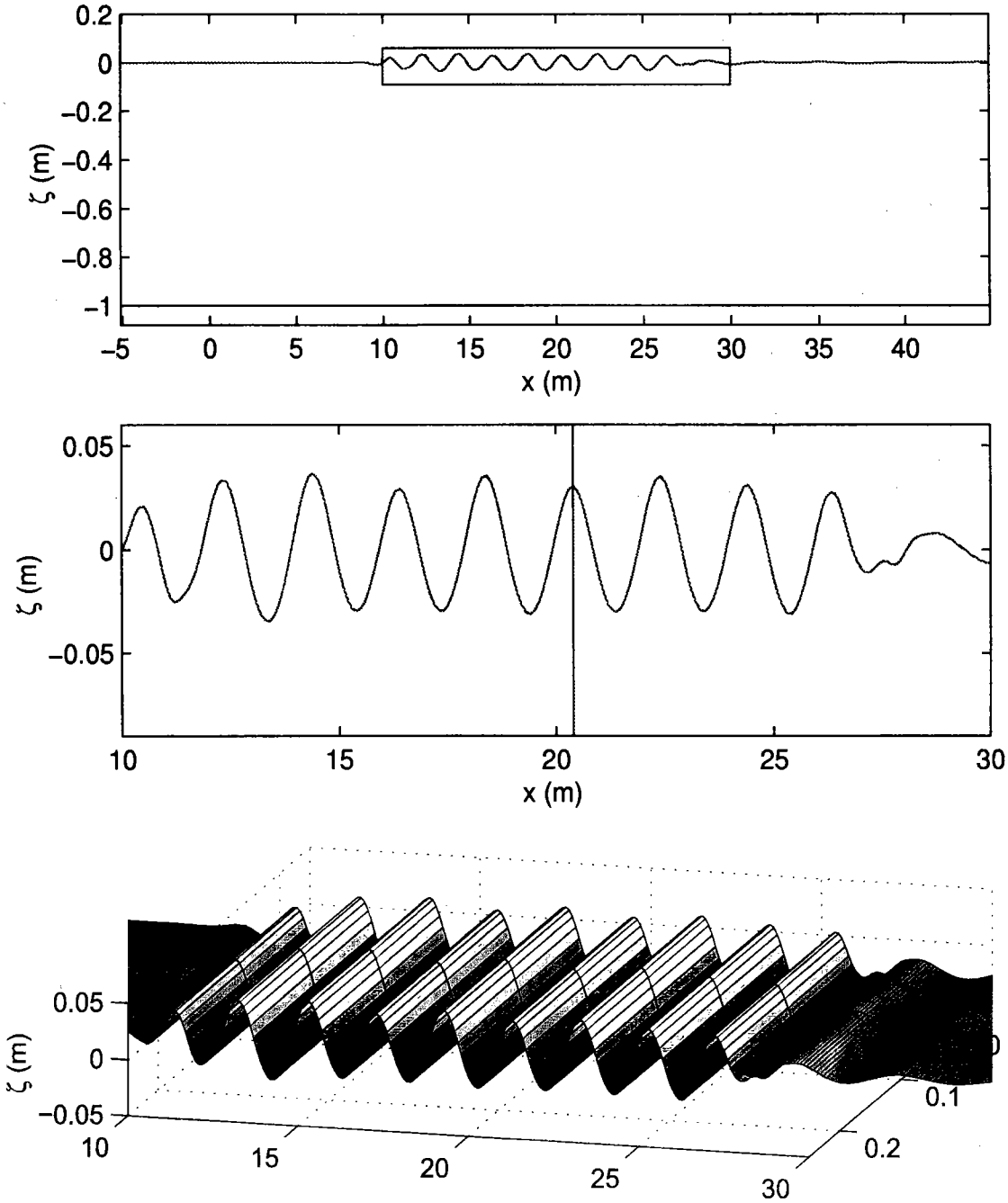

Figure 8: Propagation of deep water wave (kh = 3.14) at time t = 17.3 (sec)

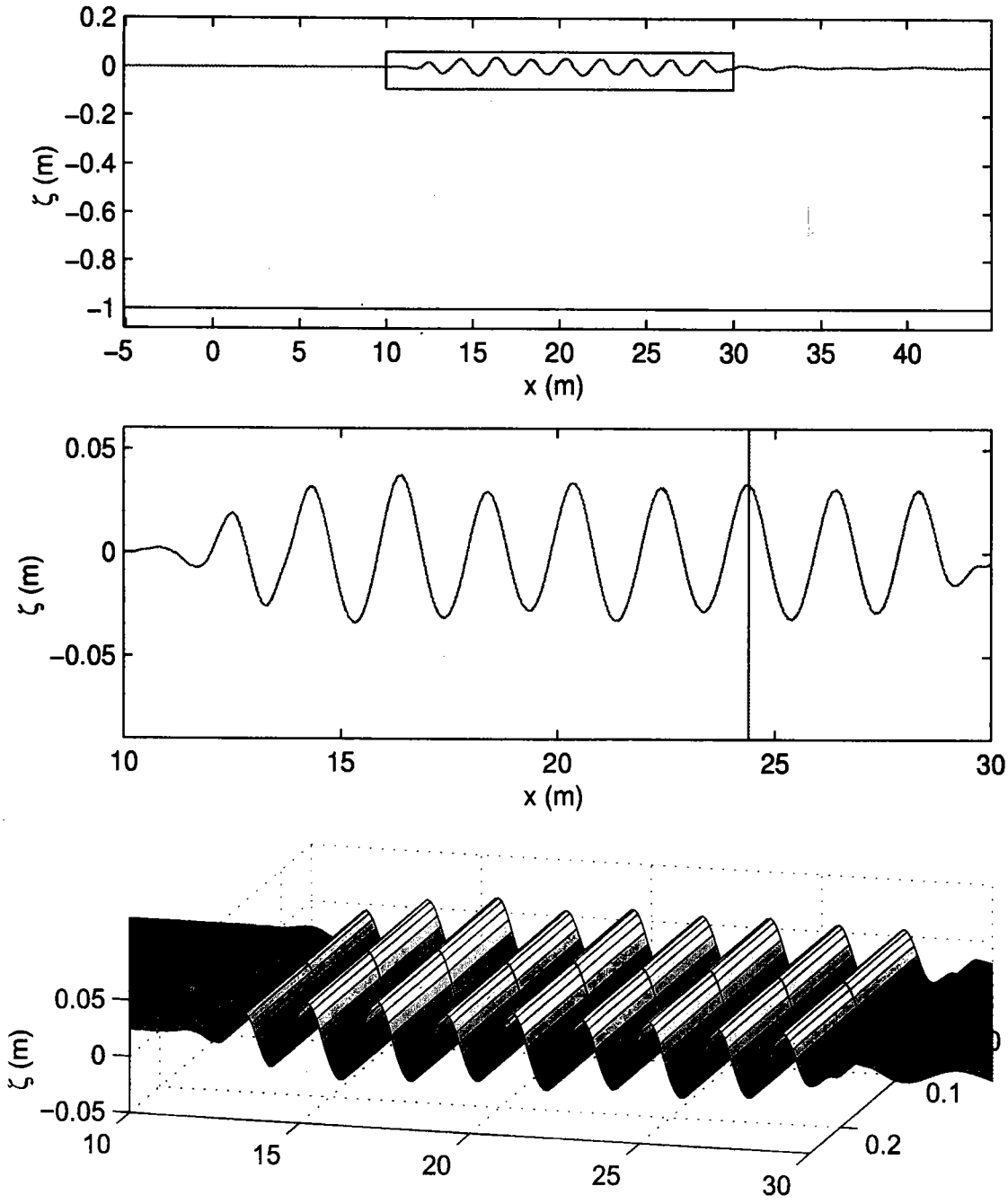

Figure 8: Propagation of deep water wave (kh = 3.14) at time t = 19.6 (sec)

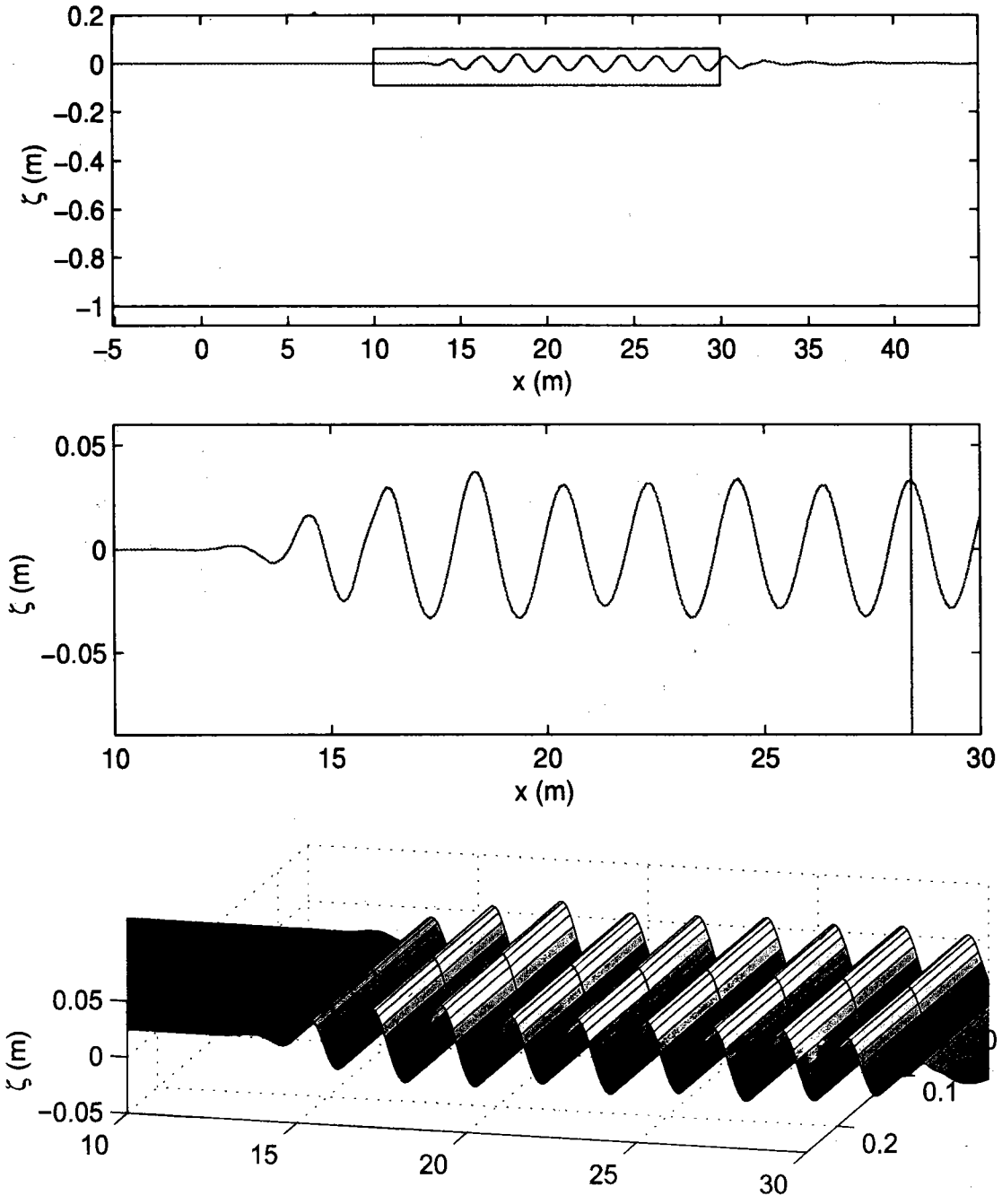

Figure 8: Propagation of deep water wave (kh = 3.14) at time t = 21.8 (sec)

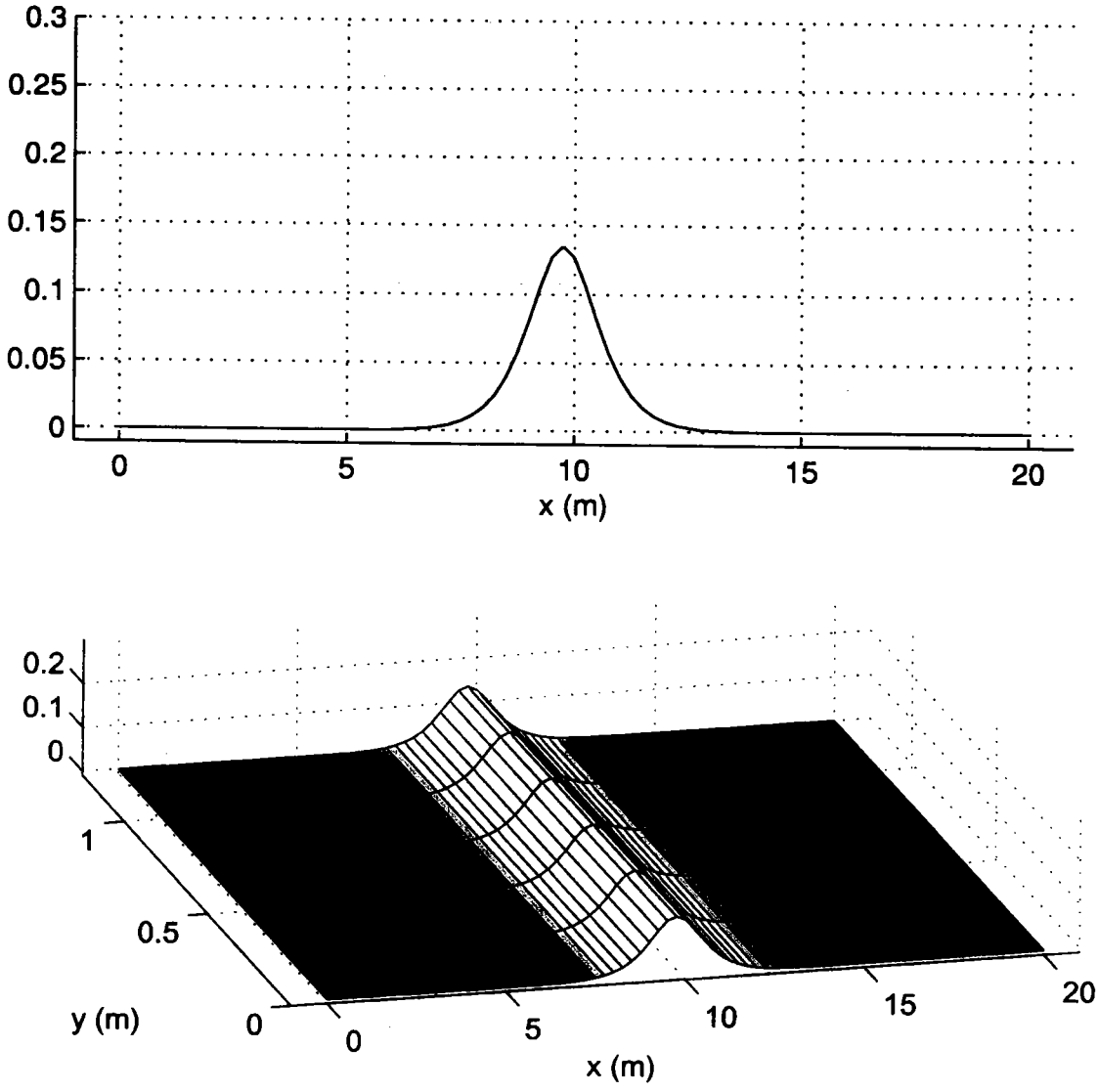

Figure 9: Snapshot of free surface elevation with two wall boundary condition at time t = 0 (sec)

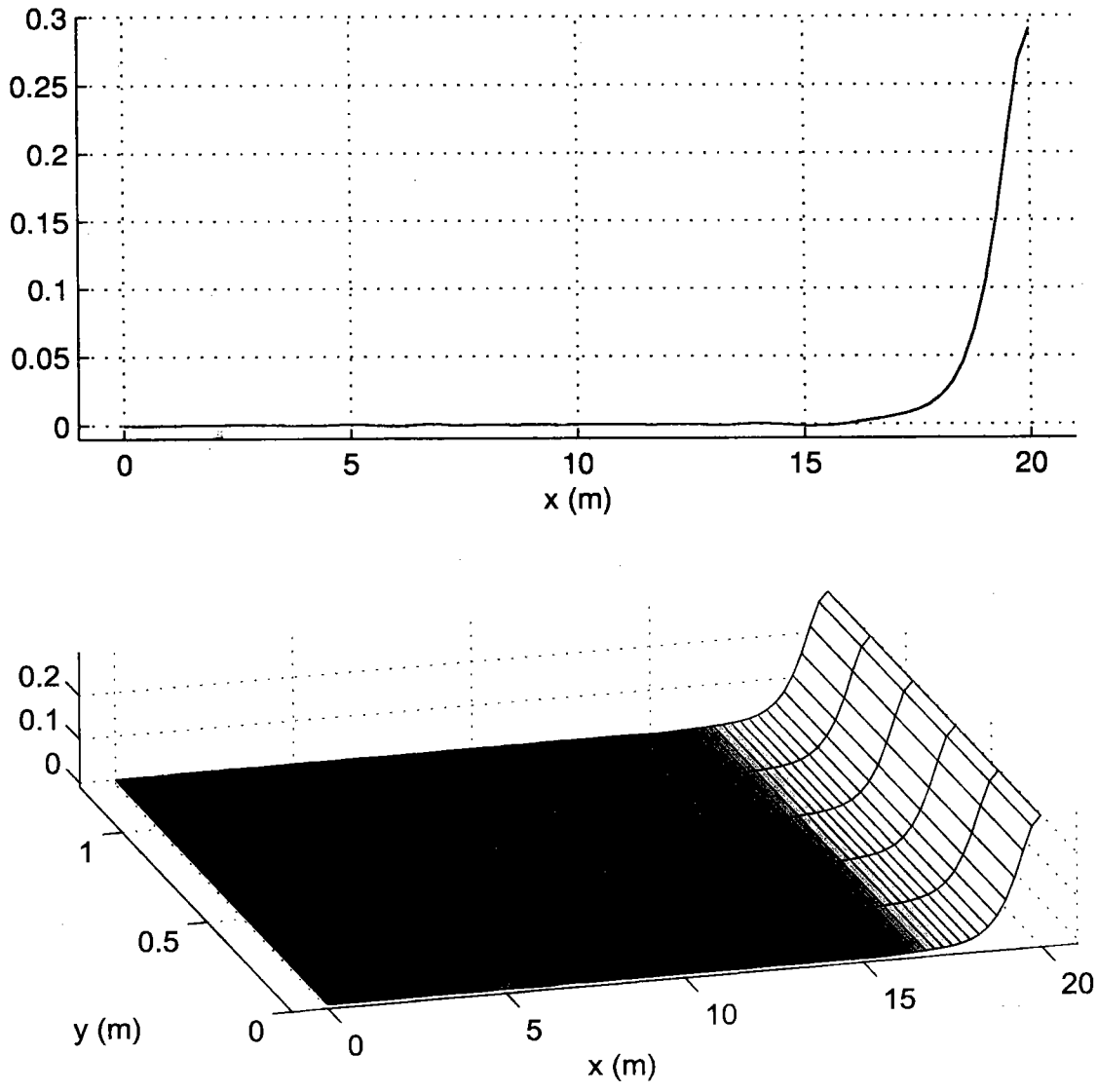

Figure 9: Snapshot of free surface elevation with two wall boundary condition at time t = 4.3 (sec)

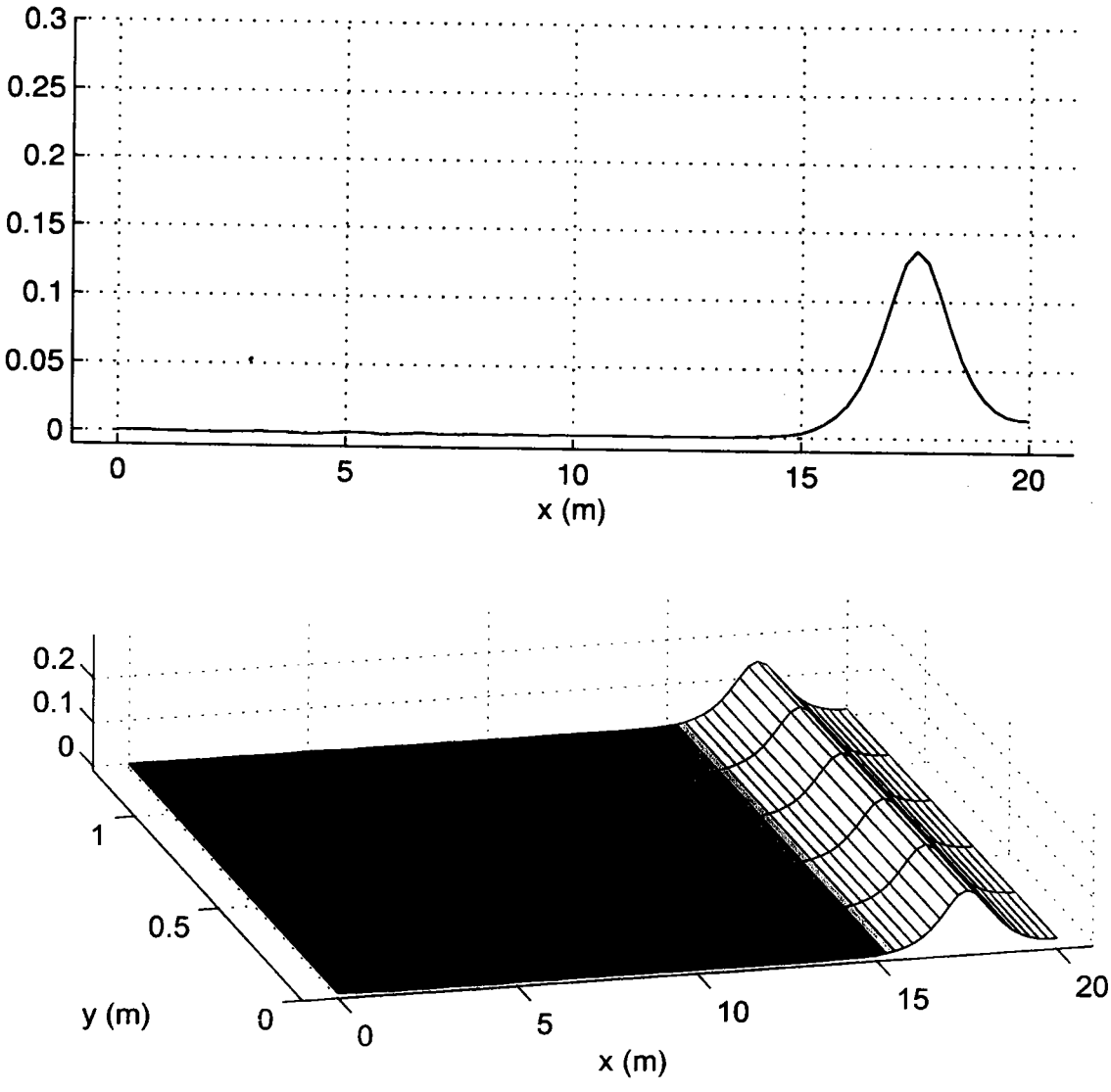

Figure 9: Snapshot of free surface elevation with two wall boundary condition at time t = 5.3 (sec)

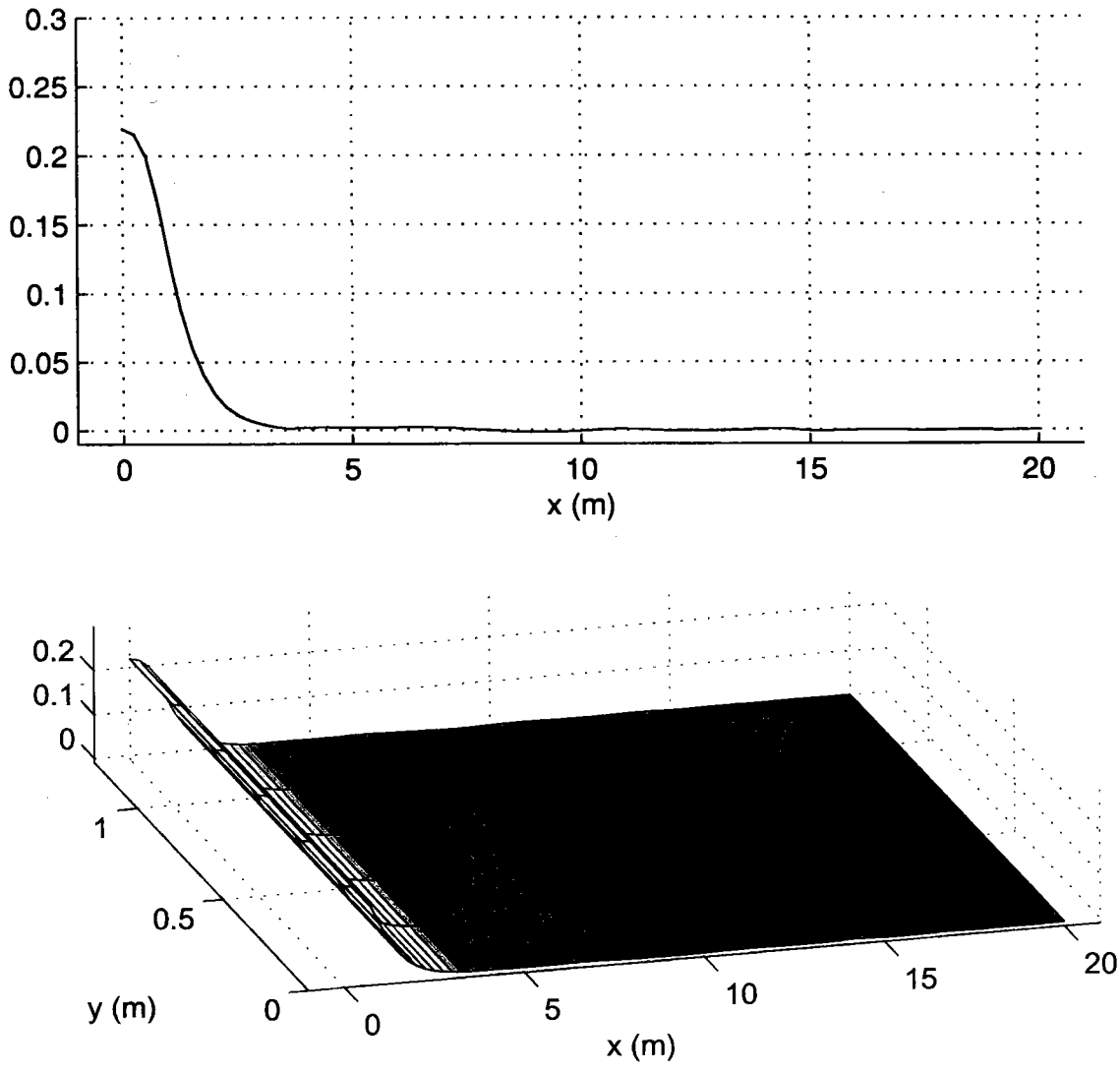

Figure 9: Snapshot of free surface elevation with two wall boundary condition at time t = 12.5 (sec)

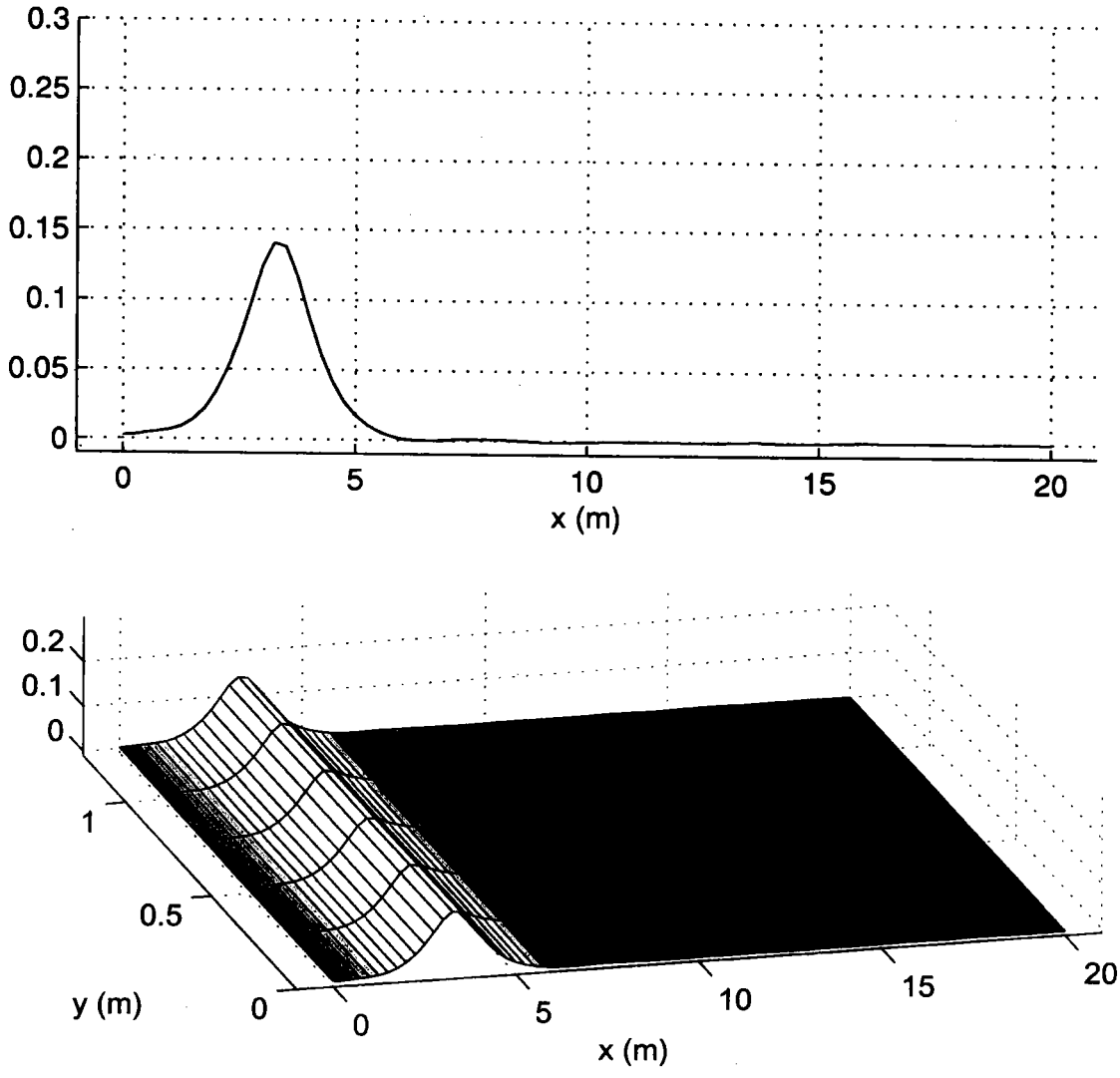

Figure 9: Snapshot of free surface elevation with two wall boundary condition at time t = 14 (sec)

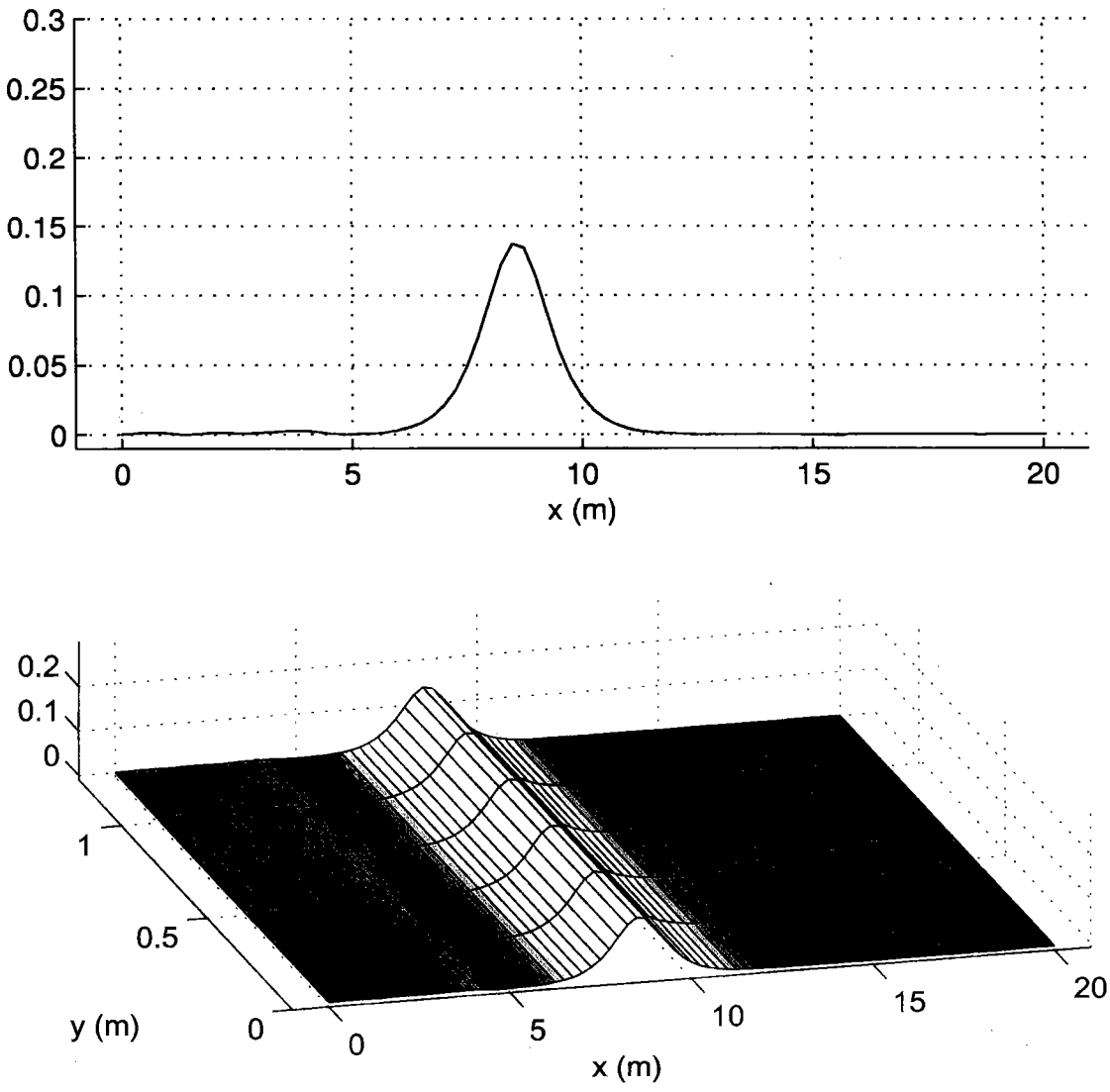

Figure 9: Snapshot of free surface elevation with two wall boundary condition at time t = 14 (sec)

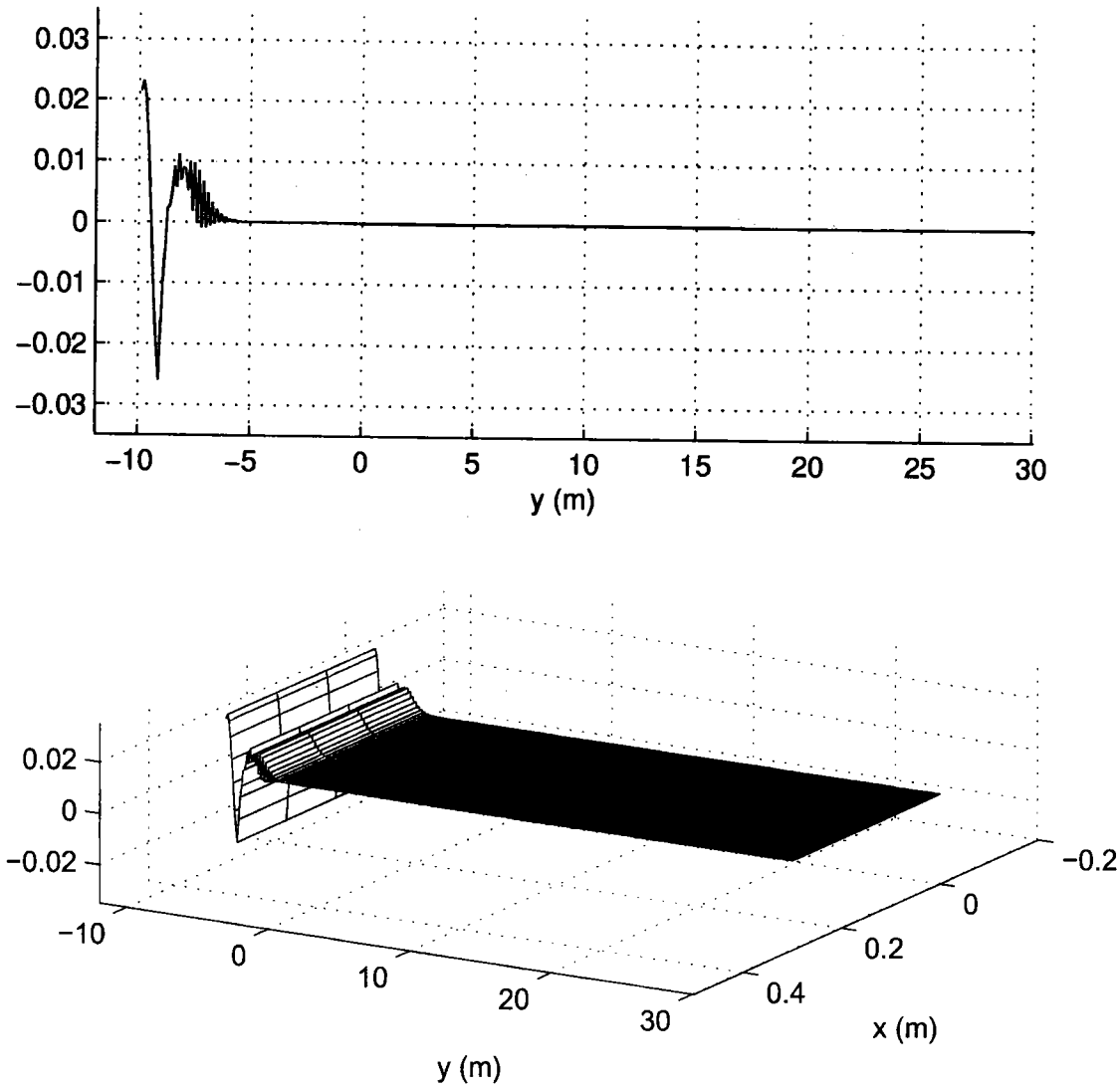

Figure 10: Snapshot of free surface elevation with wave maker on the left-hand side and sponge layer on the right-hand side boundary at time t = 4 (sec)

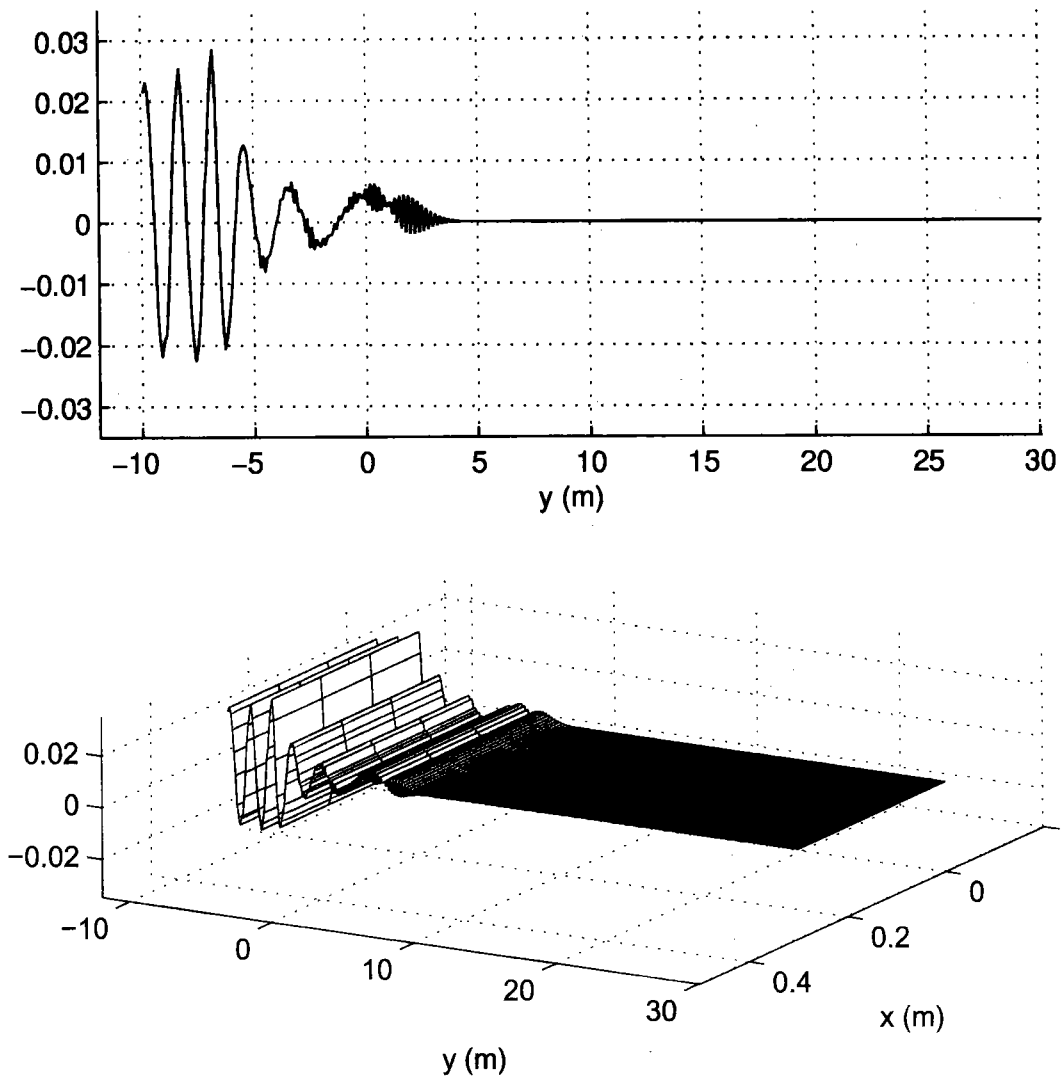

Figure 10: Snapshot of free surface elevation with wave maker on the left-hand side and sponge layer on the right-hand side boundary at time t = 8 (sec)

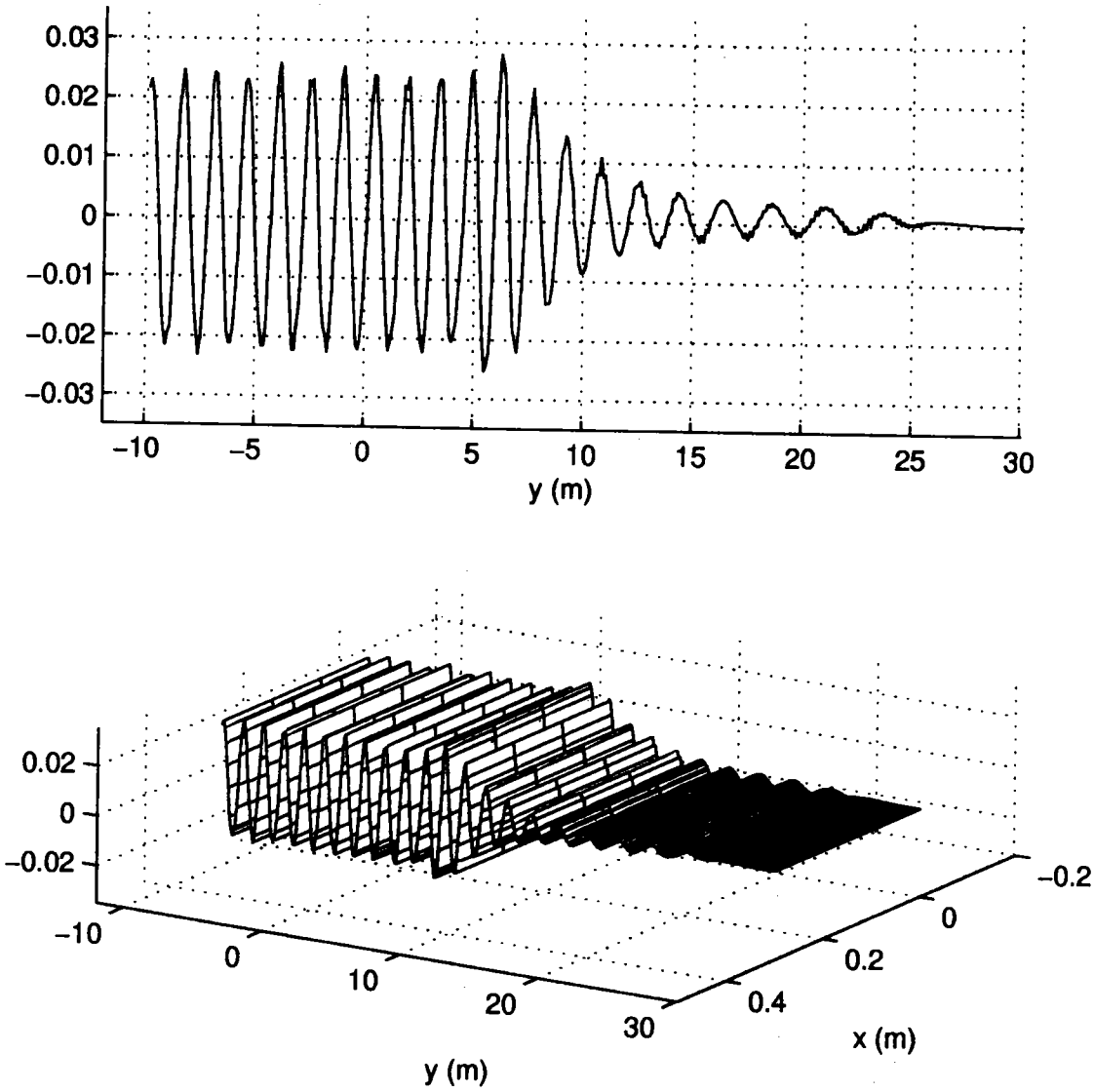

Figure 10: Snapshot of free surface elevation with wave maker on the left-hand side and sponge layer on the right-hand side boundary at time t = 26 (sec)

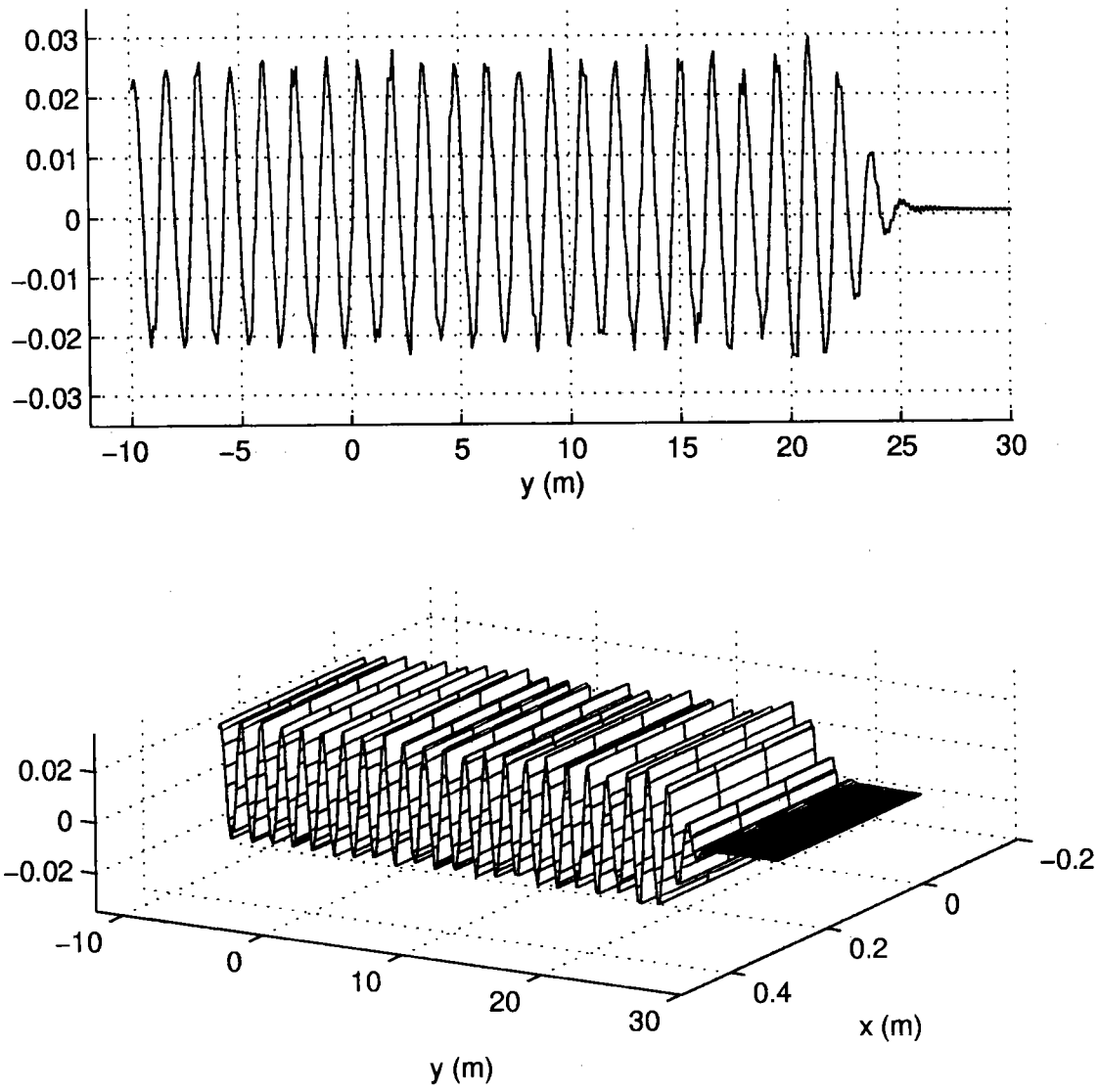

Figure 10: Snapshot of free surface elevation with wave maker on the left-hand side and sponge layer on the right-hand side boundary at time t = 46 (sec)

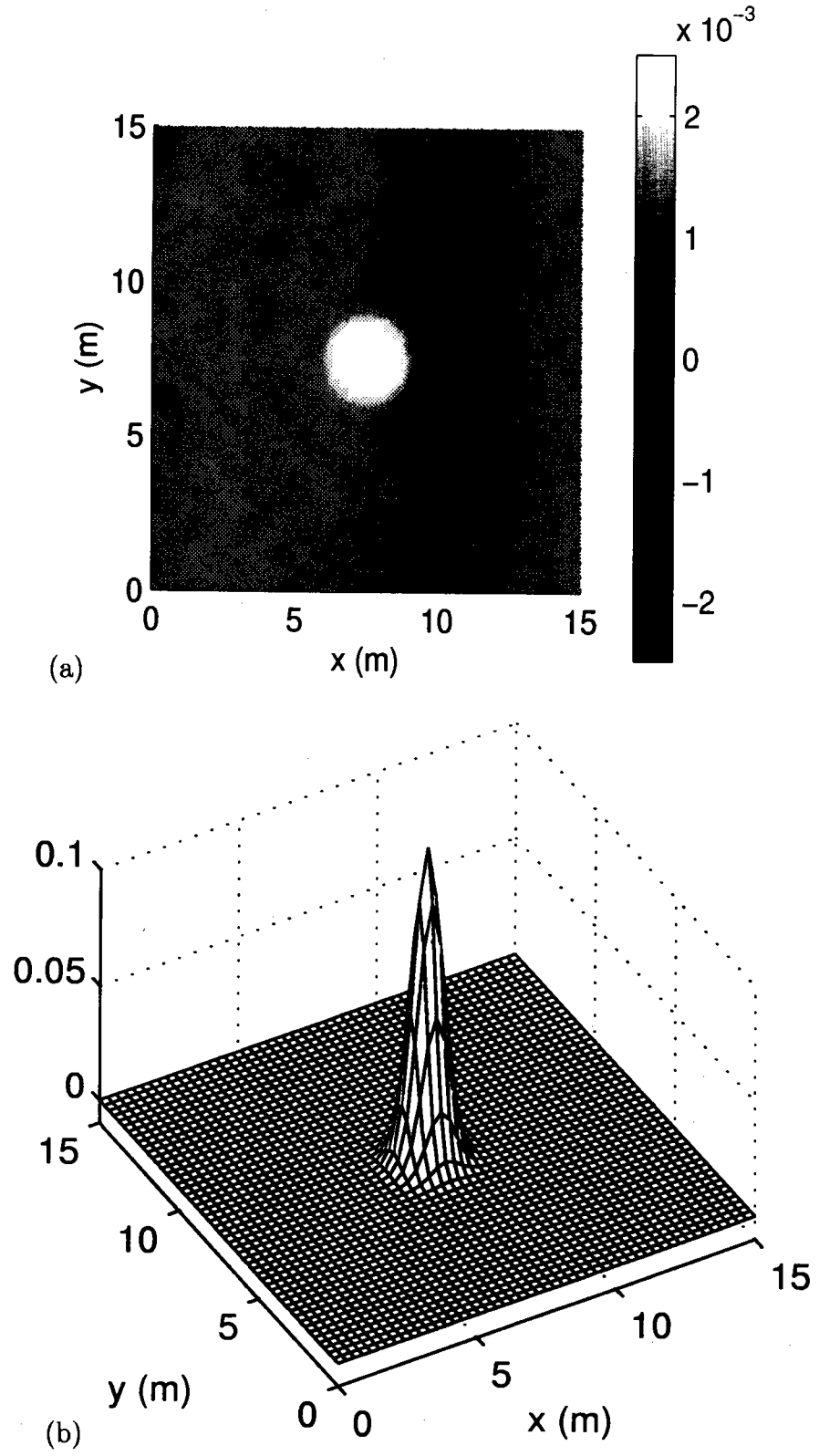

Figure 11: Snapshot of free surface elevation without interaction with boundary condition at time t = 0 (sec)

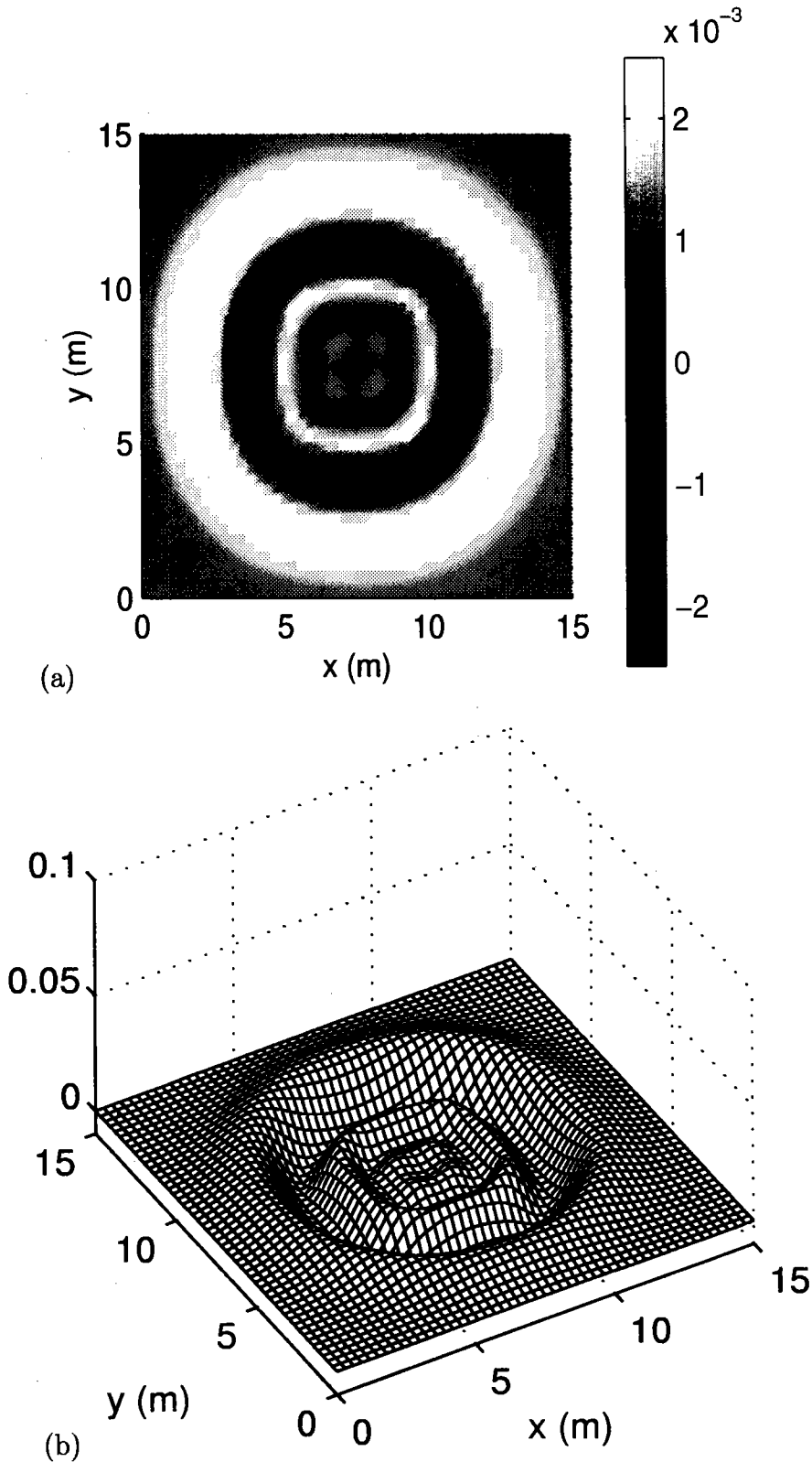

Figure 11: Snapshot of free surface elevation without interaction with boundary condition at time t = 2.7 (sec)

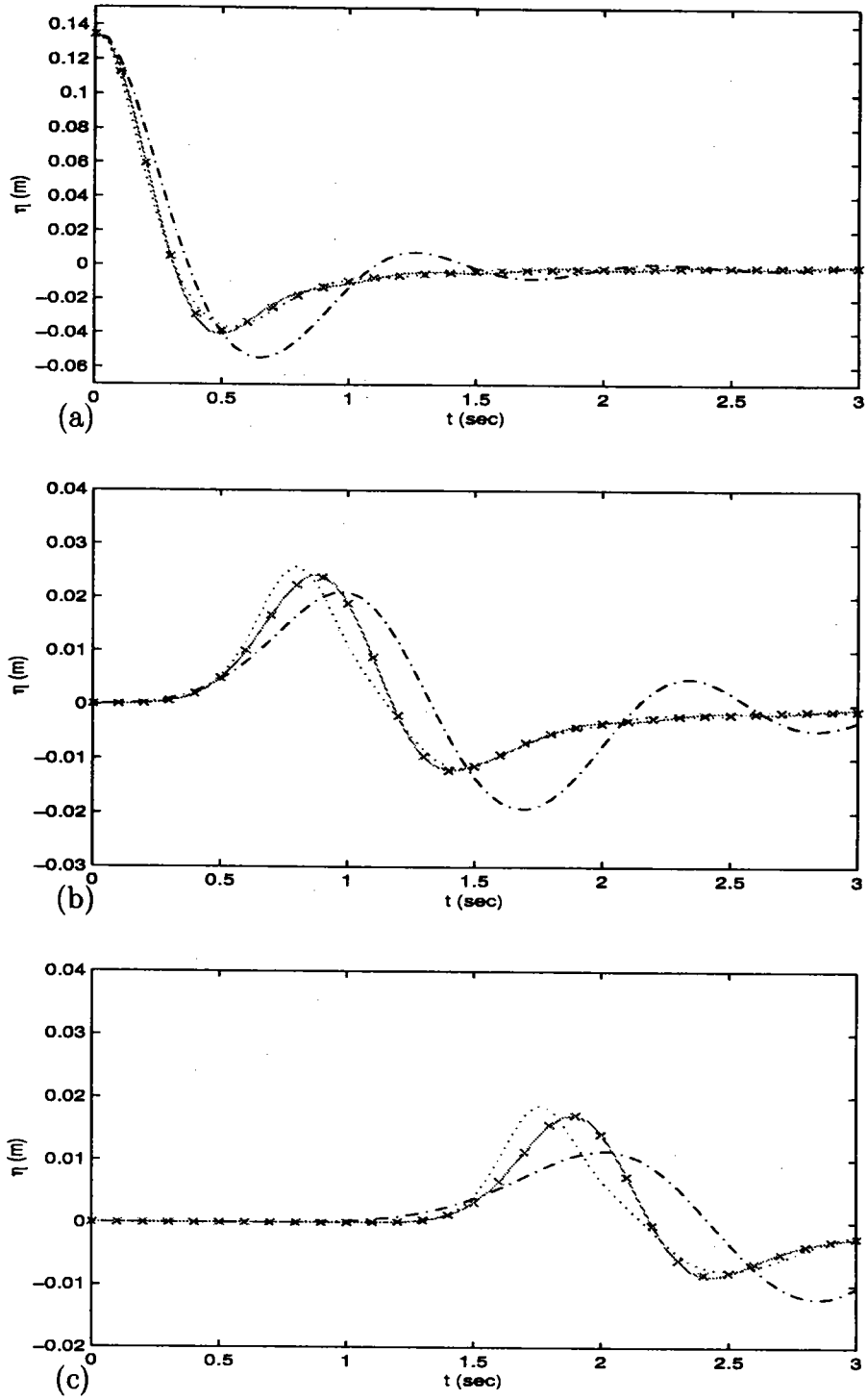

Figure 12: Comparison of time history of numerical and analytical solution at (a)x=y=7.5, (b)x=y=6.0, (c)x=y=4.5 (m). Mark (x x x): Analytic solution of linear shallow water equation, Full line (——): Linear shallow water model, dashed line (· · · · ·): Nonlinear shallow water model, dashed dot line (– · – · – ·): Boussinesq model.

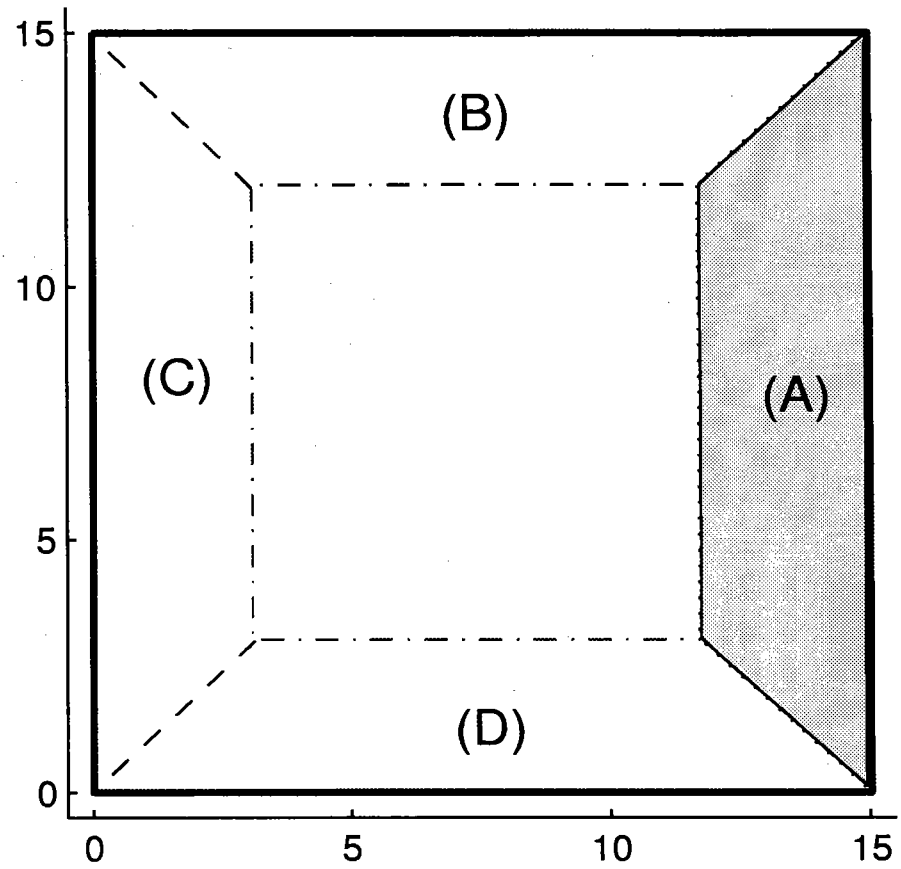

Figure 13: Computational domain and sponge layers for testing radiation boundary

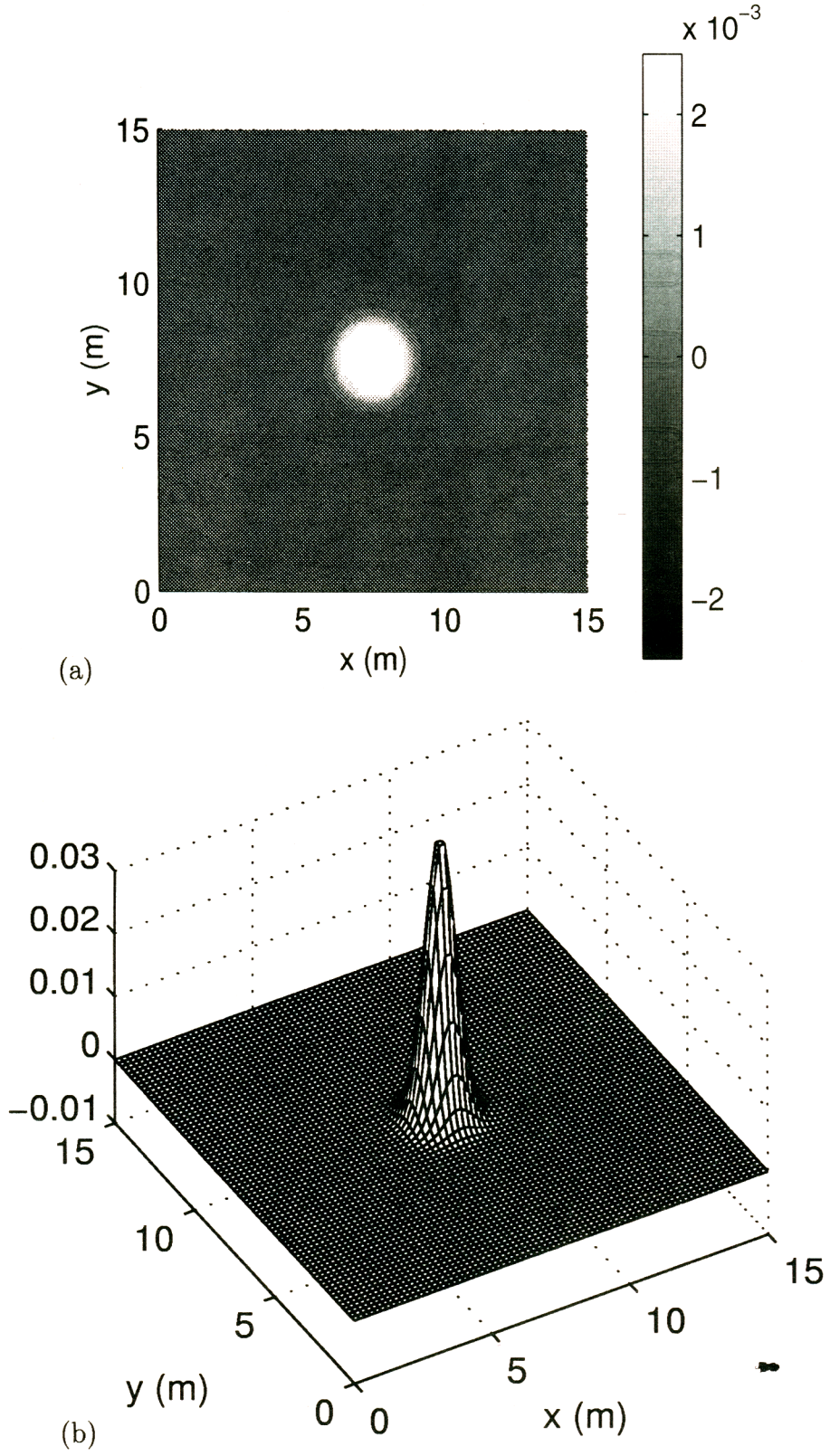

Figure 14: Snapshot of free surface elevation for testing radiation boundary condition at time t = 0 (sec)

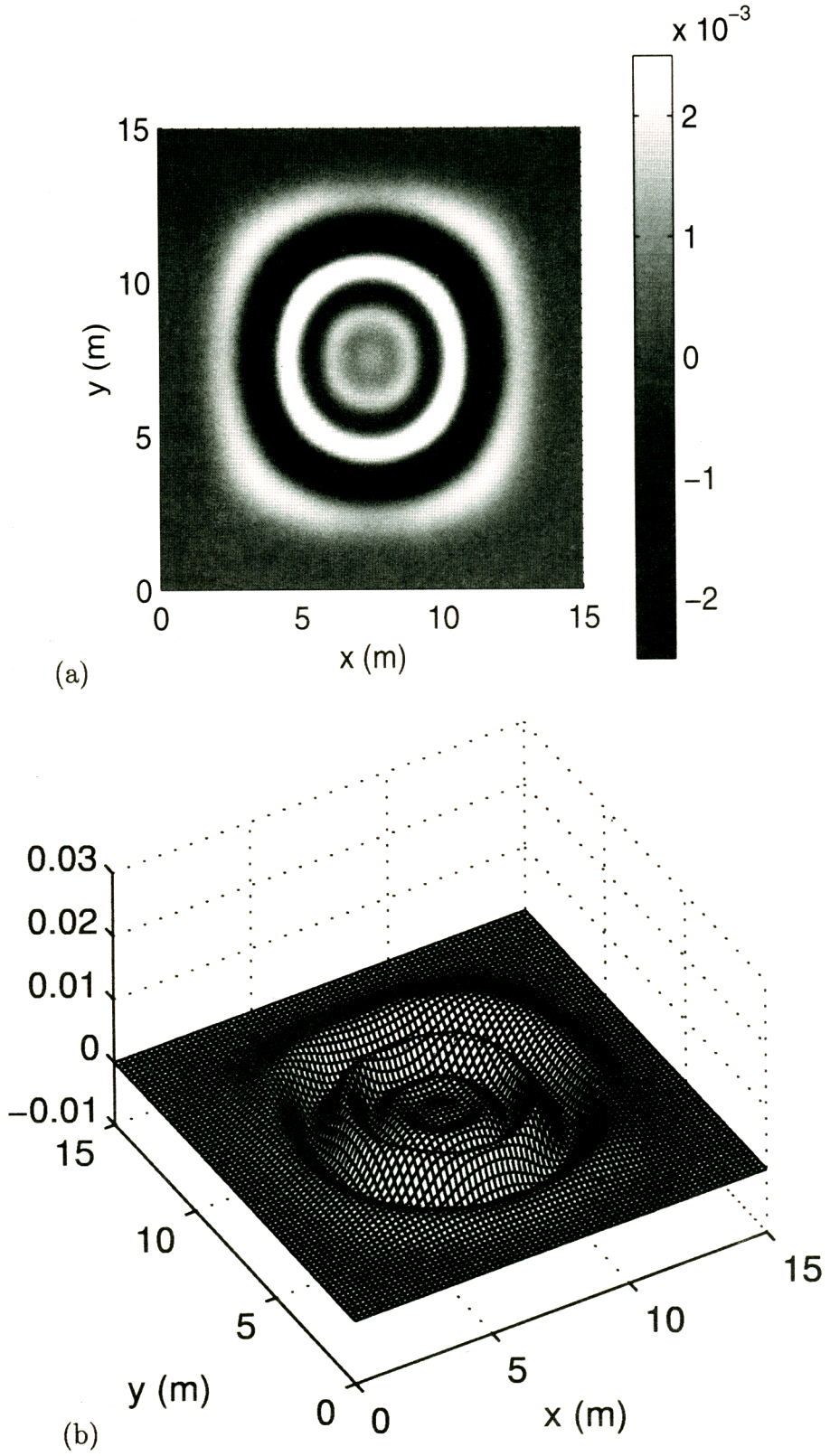

Figure 14: Snapshot of free surface elevation for testing radiation boundary condition at time t = 3 (sec)

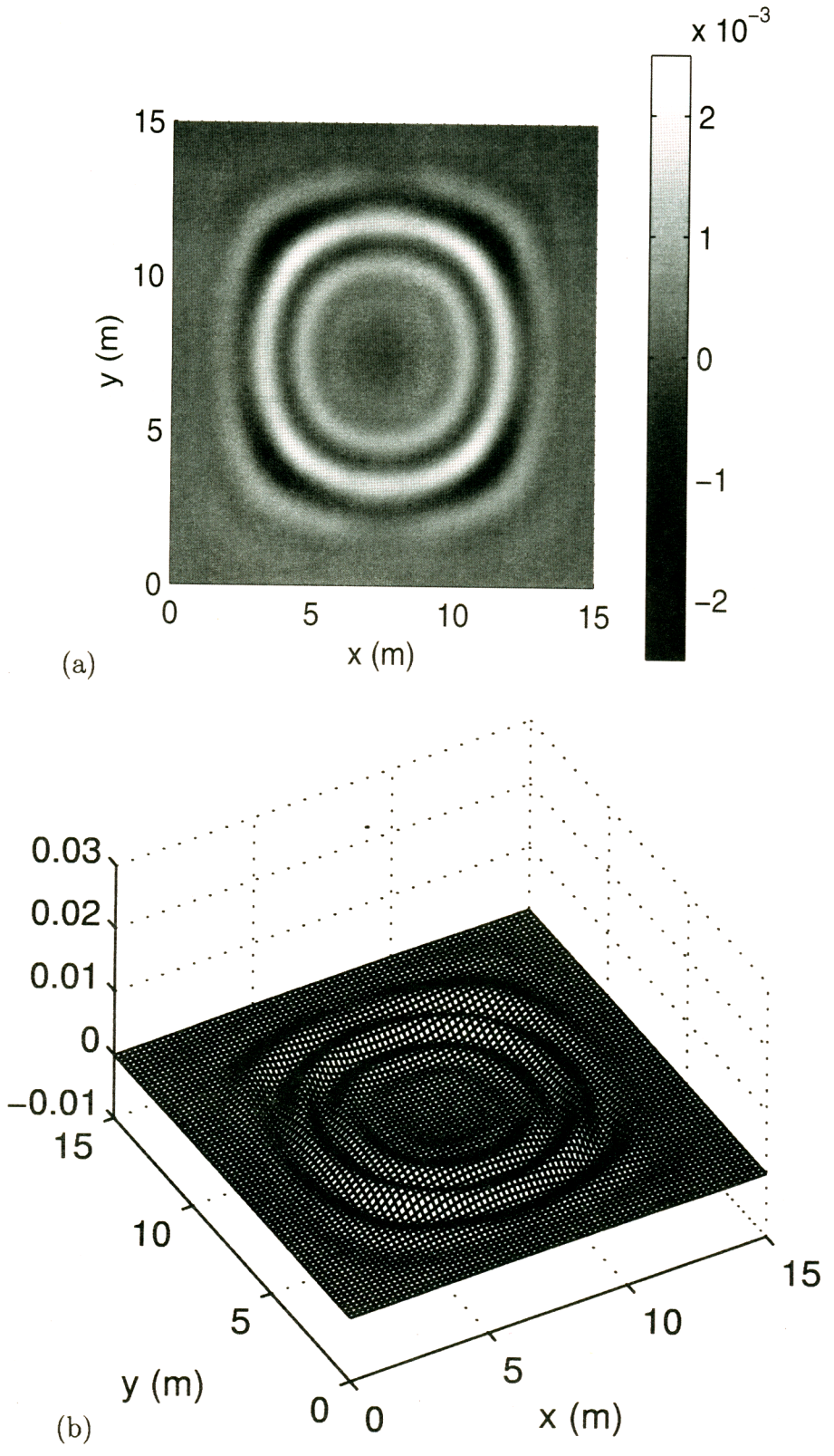

Figure 14: Snapshot of free surface elevation for testing radiation boundary condition at time t = 5 (sec)

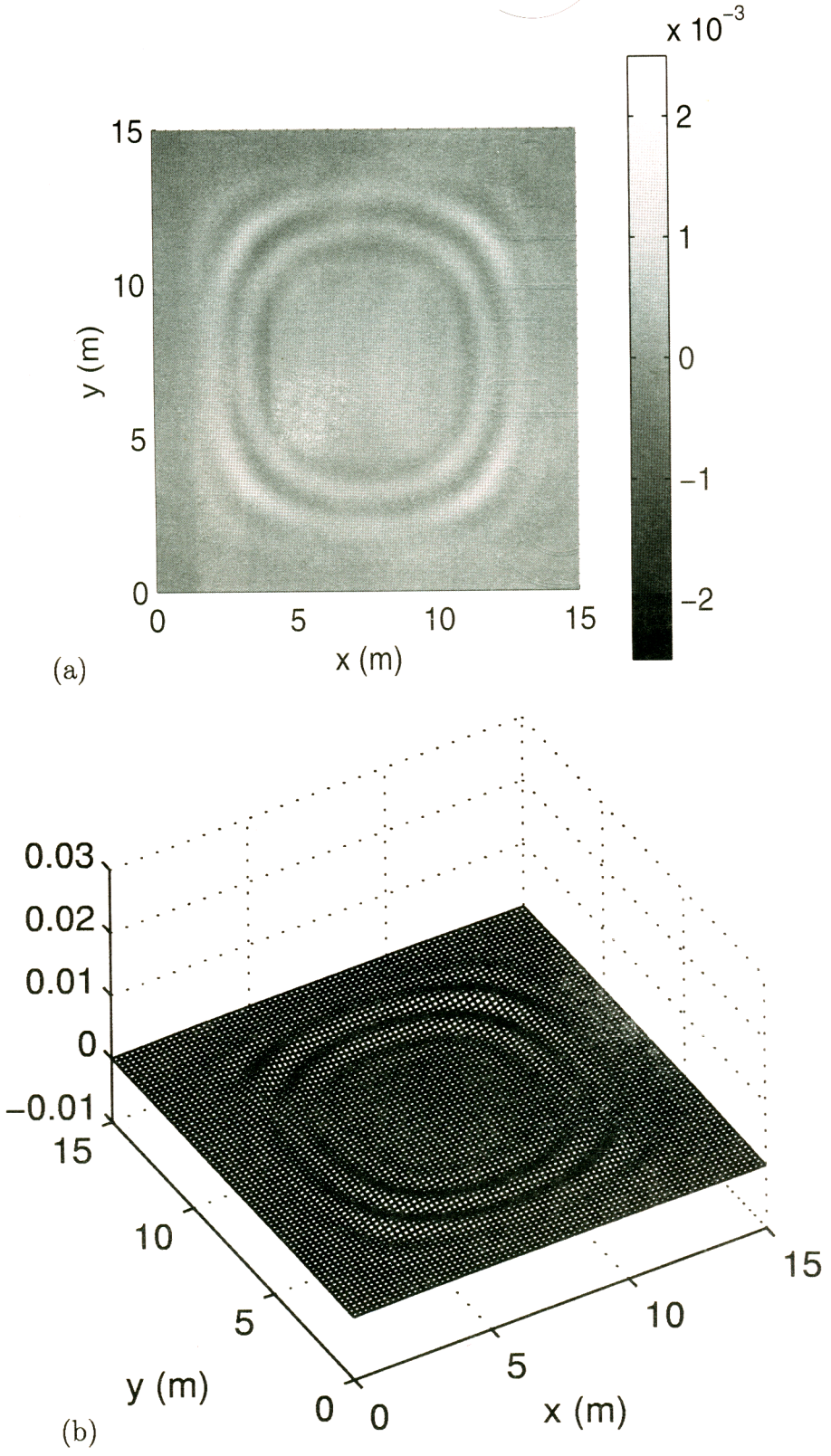

Figure 14: Snapshot of free surface elevation for testing radiation boundary condition at time t = 7 (sec)

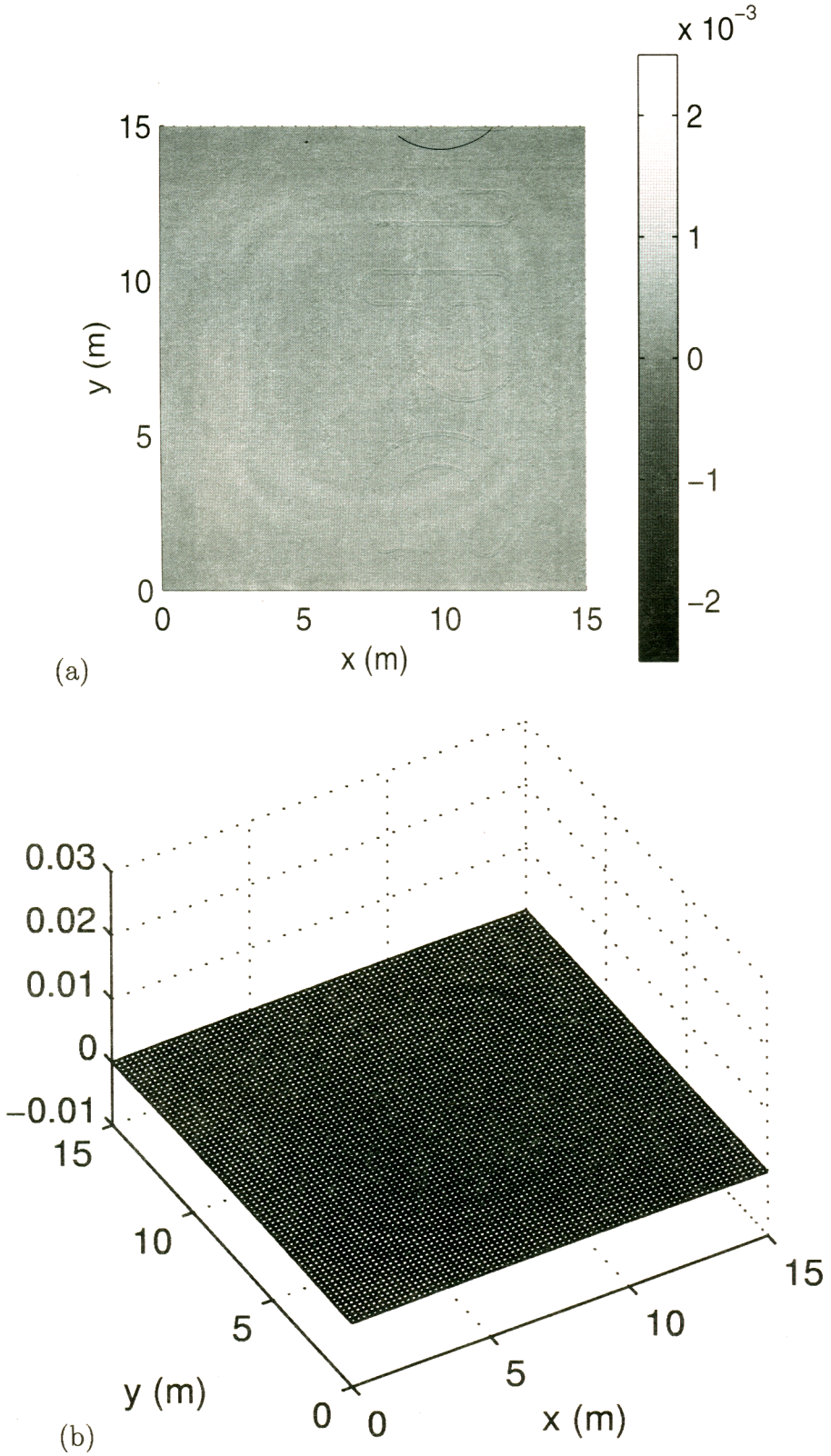

Figure 14: Snapshot of free surface elevation for testing radiation boundary condition at time t = 10 (sec)

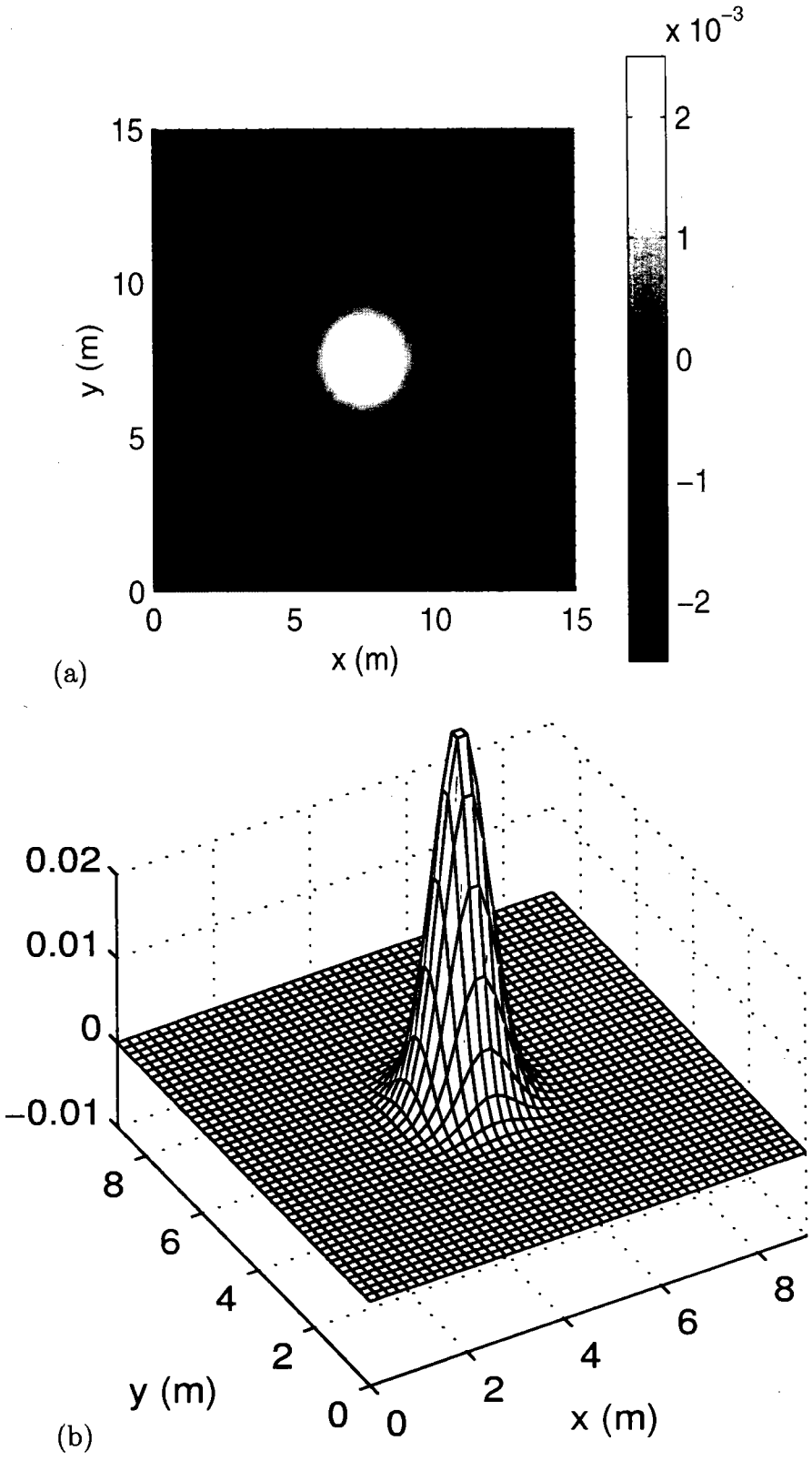

Figure 15: Snapshot of free surface elevation for testing reflective wall boundary condition at time t = 0 (sec)

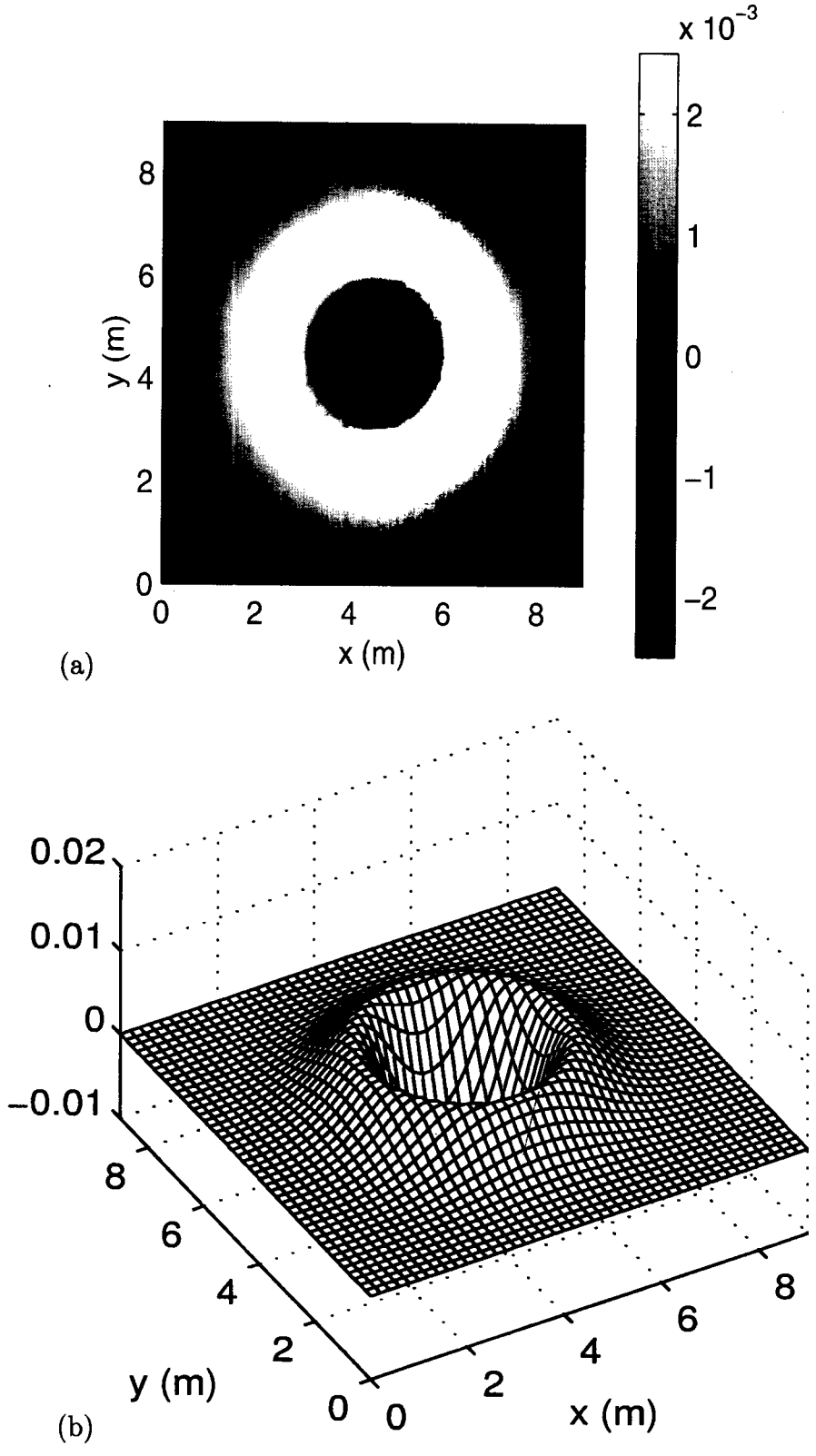

Figure 15: Snapshot of free surface elevation for testing reflective wall boundary condition at time t = 1 (sec)

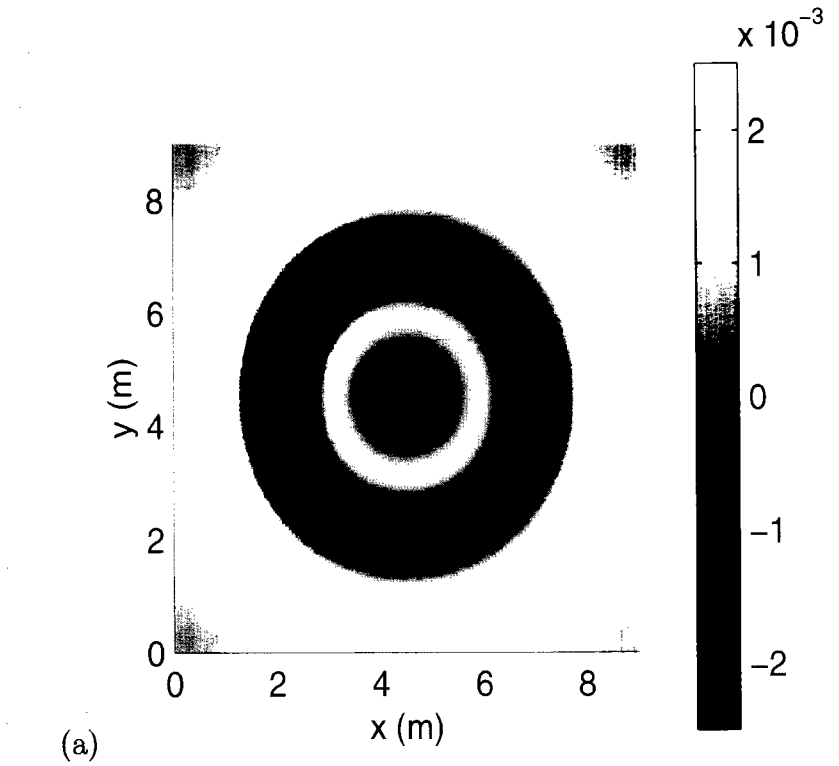

(a)

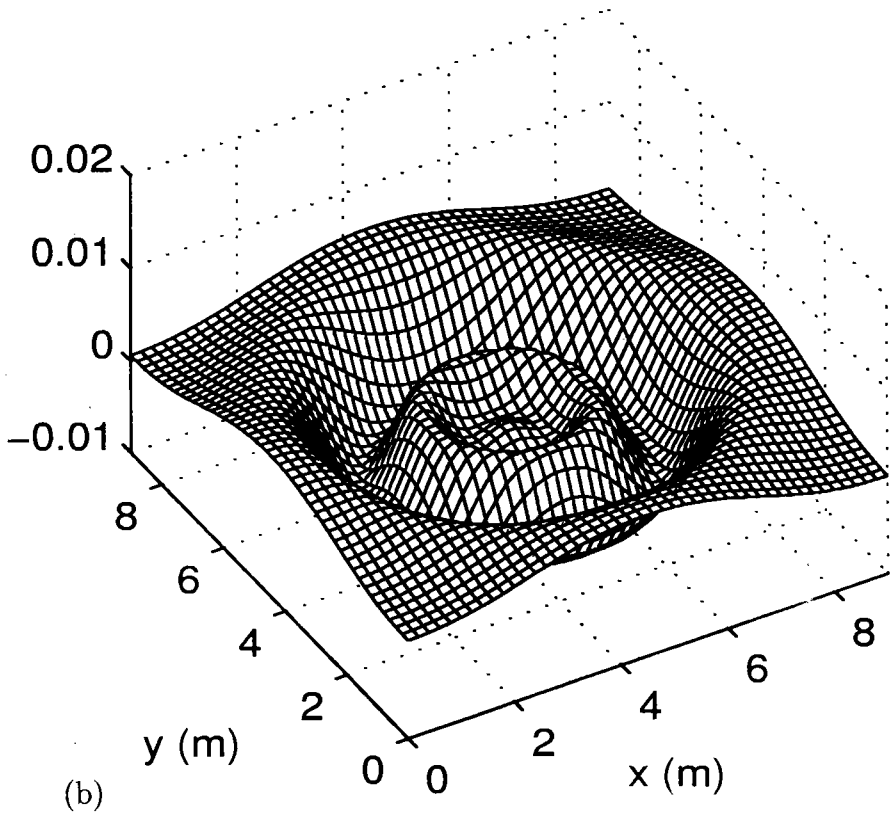

(b)

Figure 15: Snapshot of free surface elevation for testing reflective wall boundary condition at time t = 2 (sec)

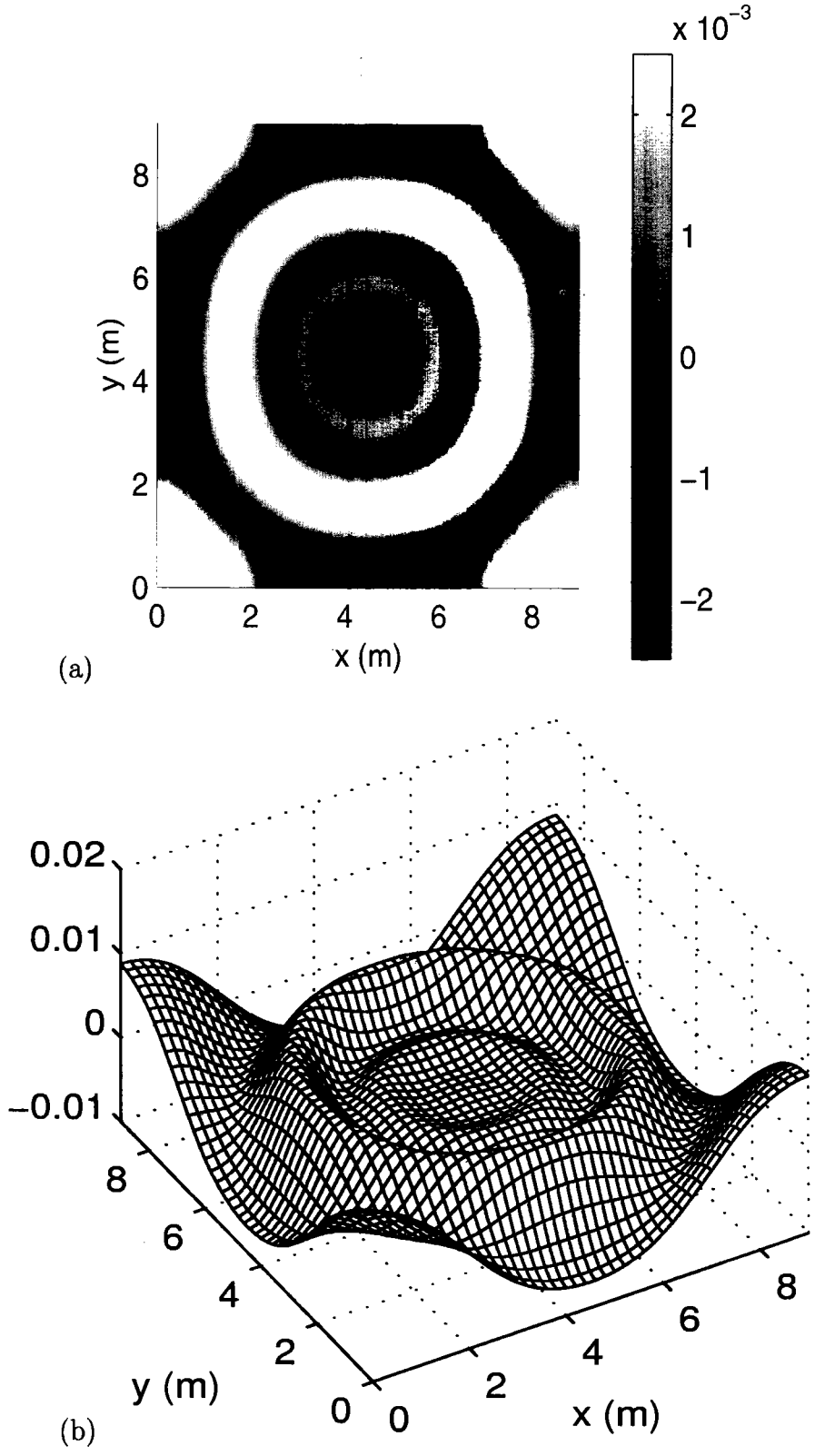

Figure 15: Snapshot of free surface elevation for testing reflective wall boundary condition at time t = 3 (sec)

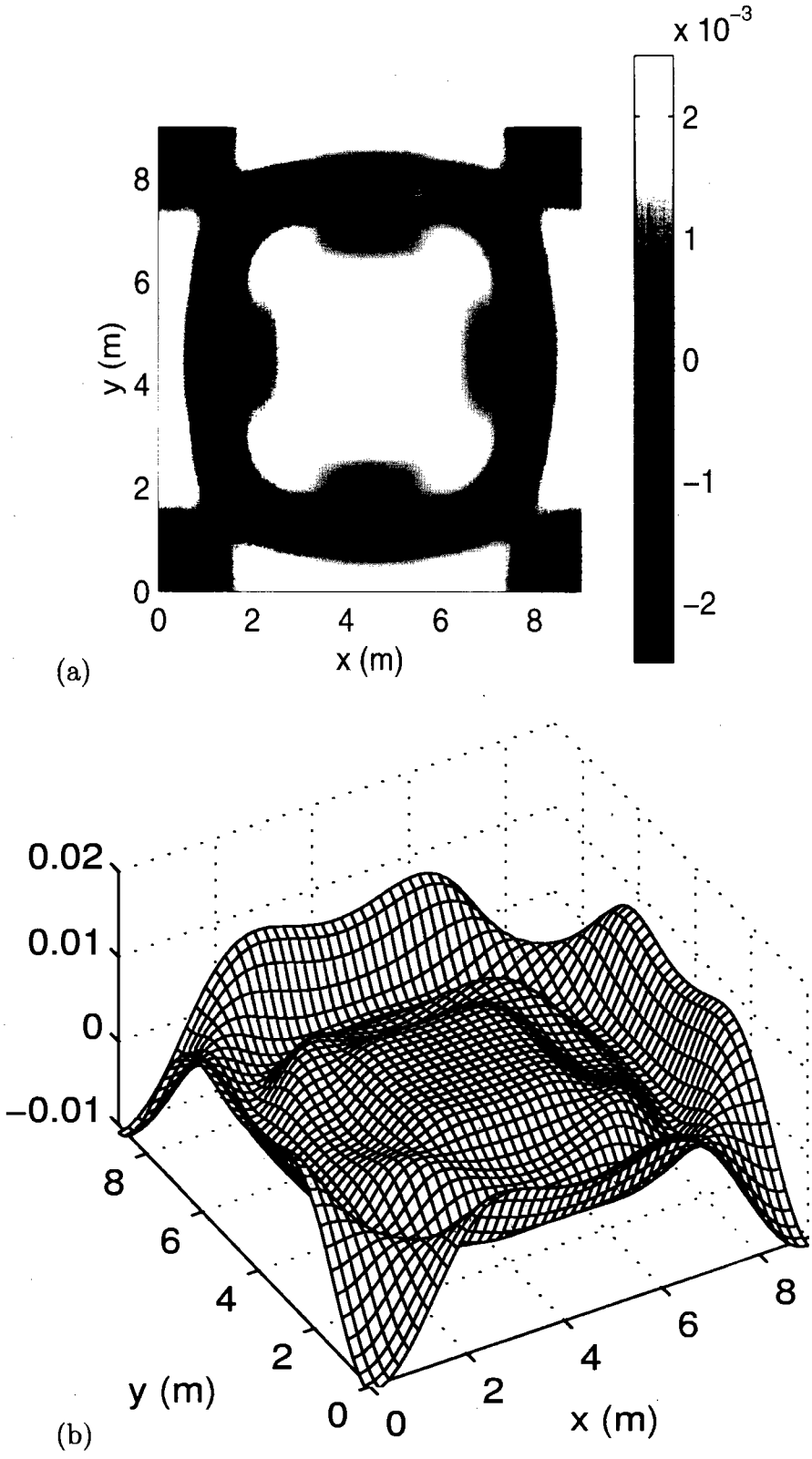

Figure 15: Snapshot of free surface elevation for testing reflective wall boundary condition at time t = 4 (sec)

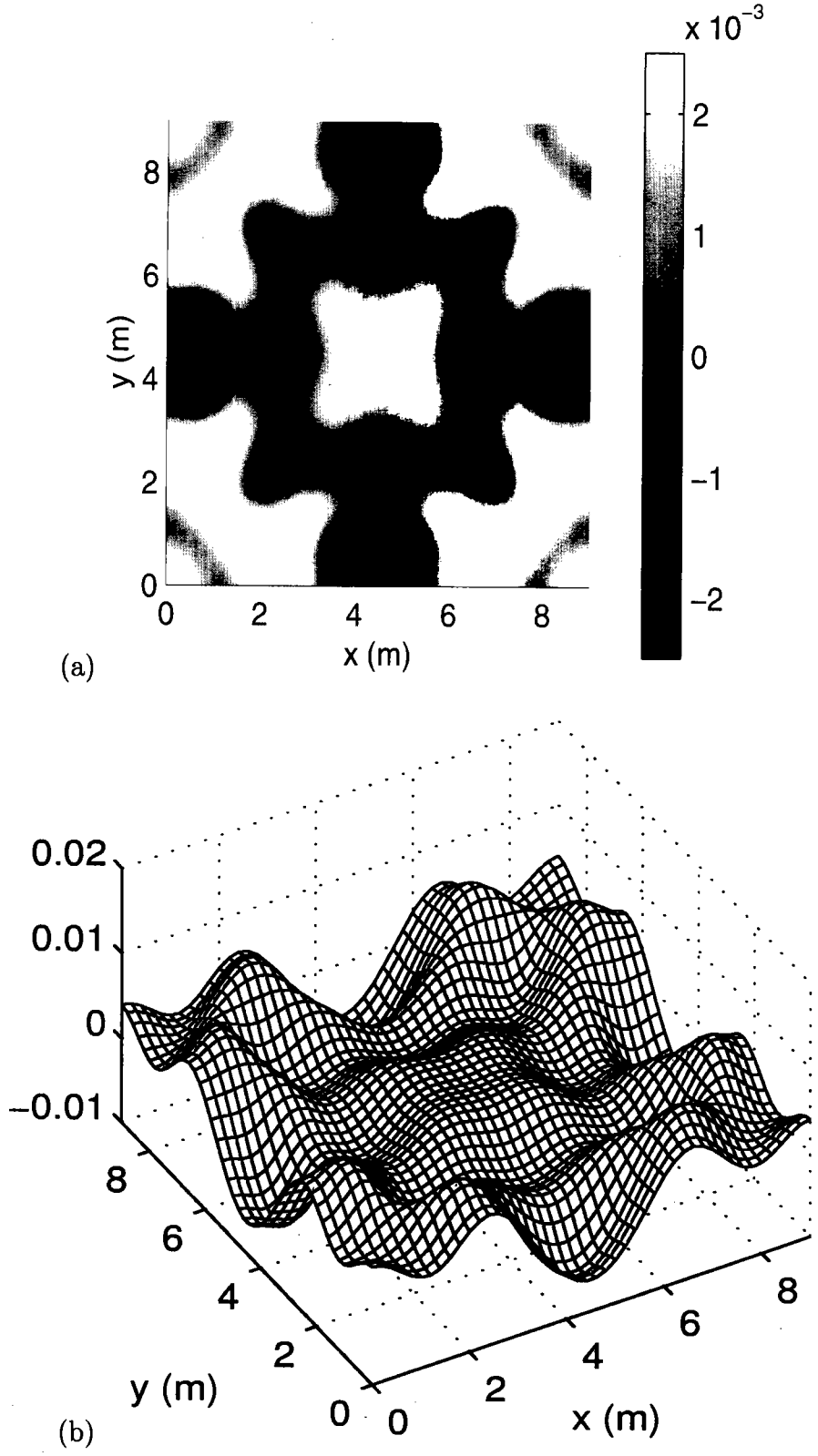

Figure 15: Snapshot of free surface elevation for testing reflective wall boundary condition at time t = 6 (sec)

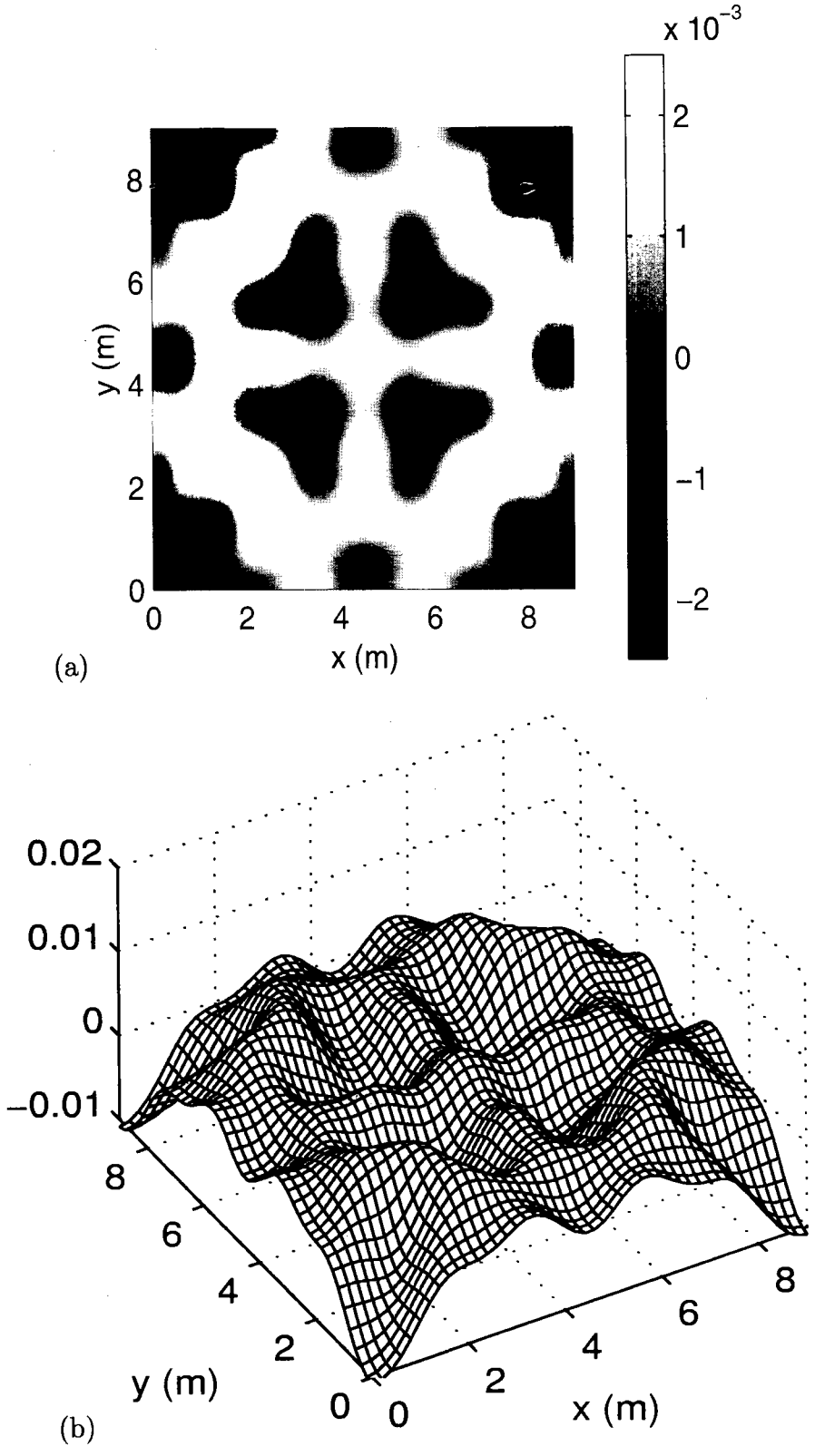

Figure 15: Snapshot of free surface elevation for testing reflective wall boundary condition at time t = 8 (sec)

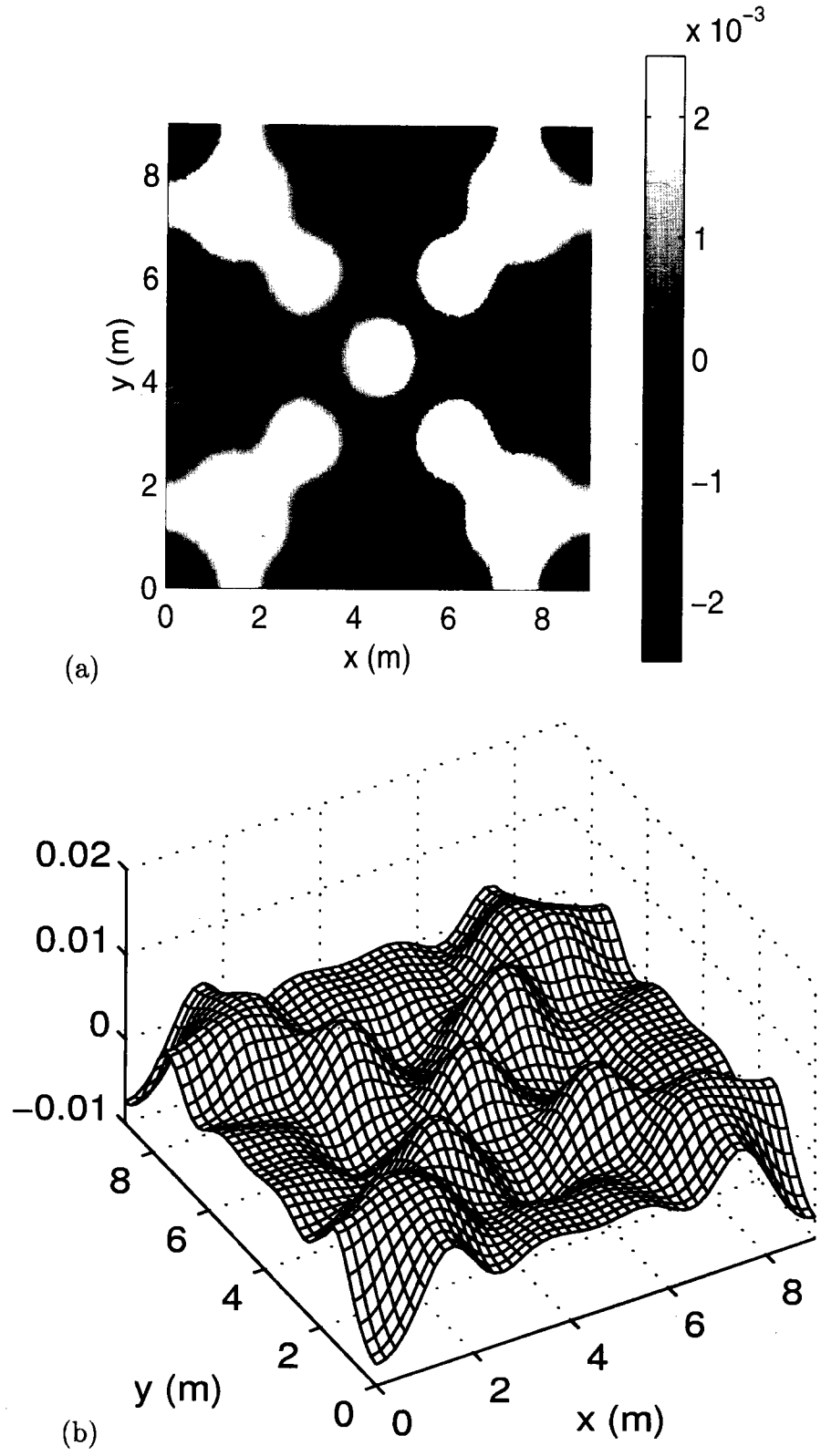

Figure 15: Snapshot of free surface elevation for testing reflective wall boundary condition at time t = 10 (sec)

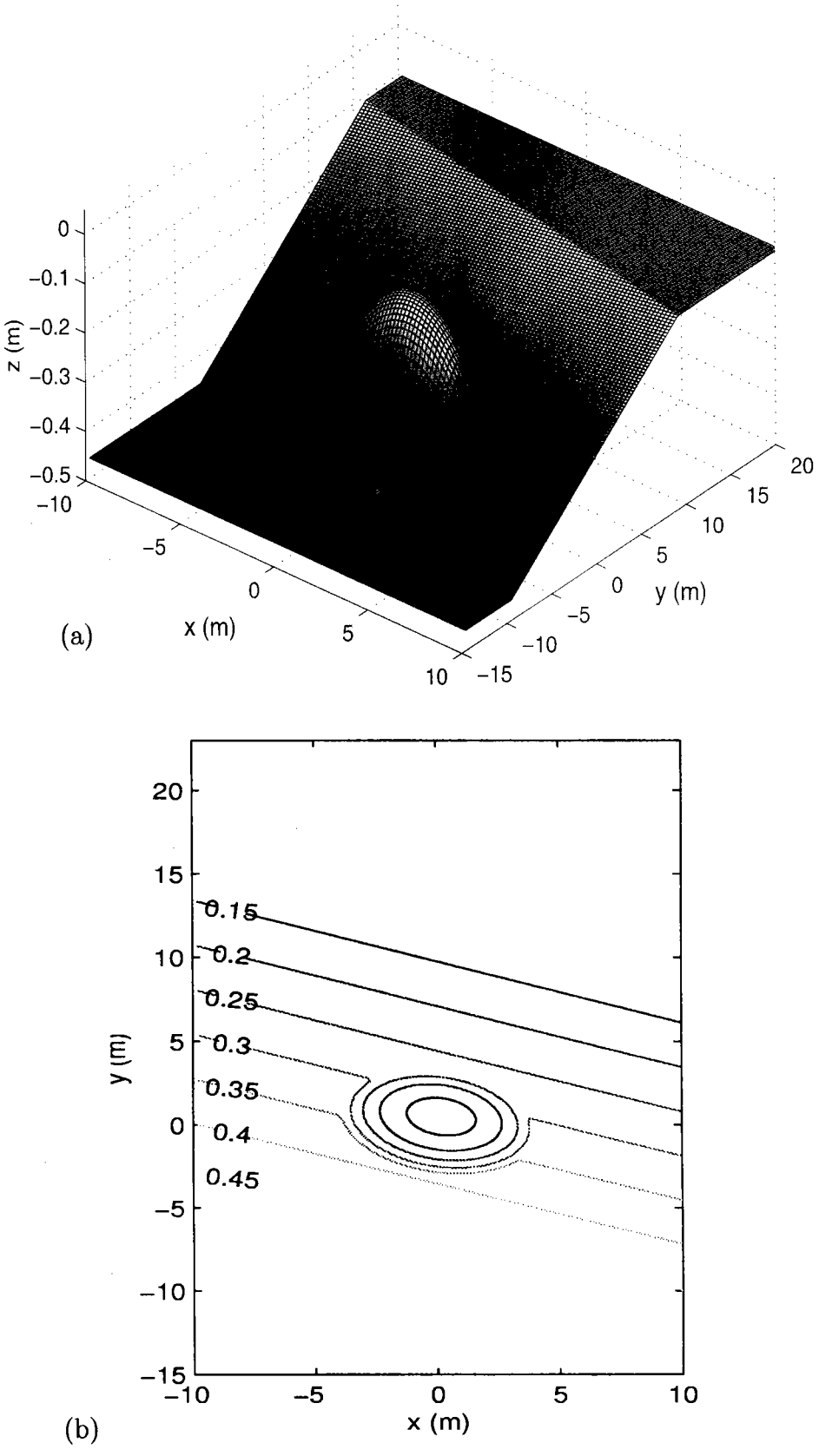

Figure 16: Bottom topography and computational domain for experiment of Berkhoff et al. (1982)

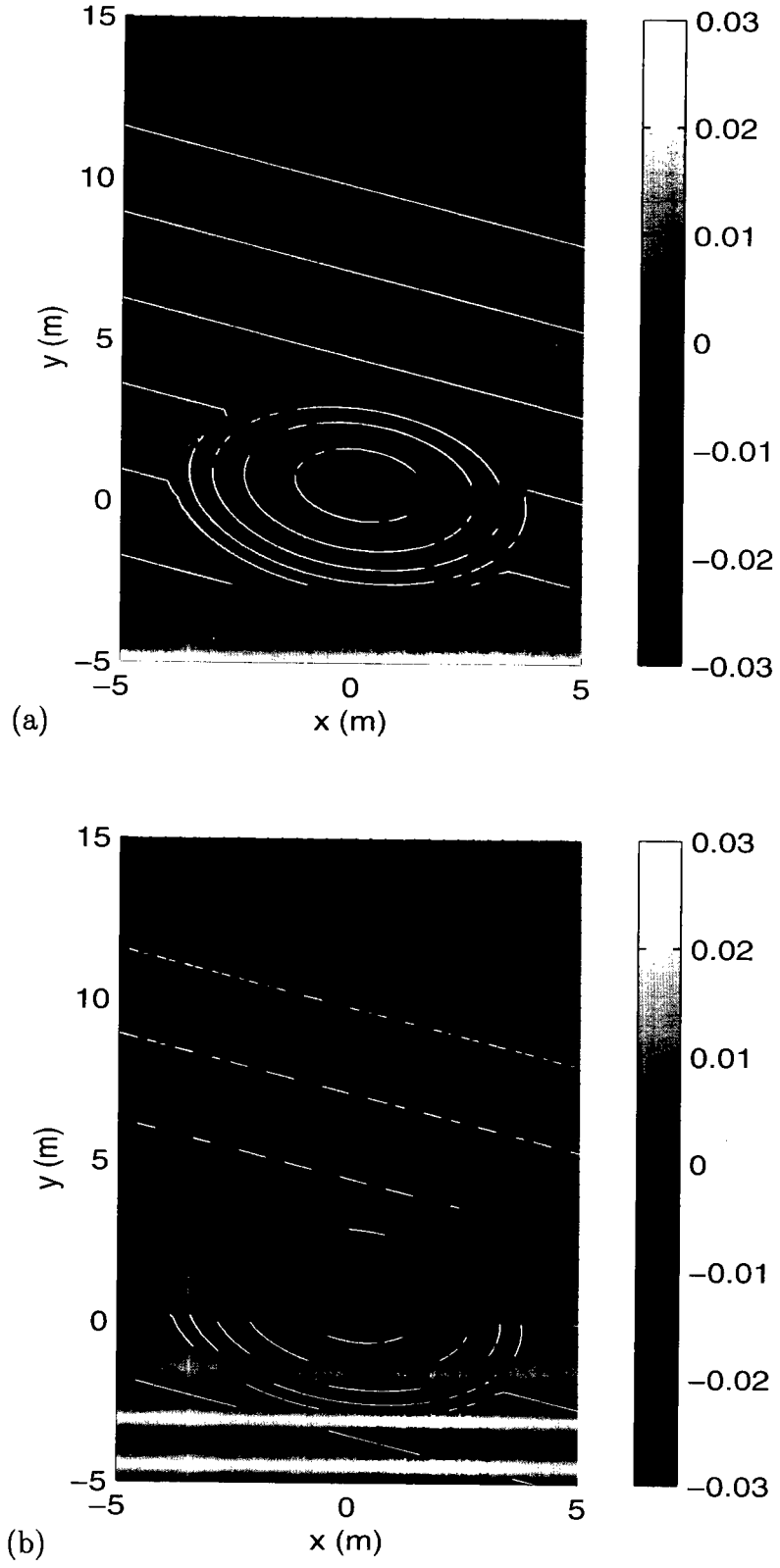

Figure 17: Snapshot of free surface elevation at time (a)t = 0, (b)t= 3.3 (sec)

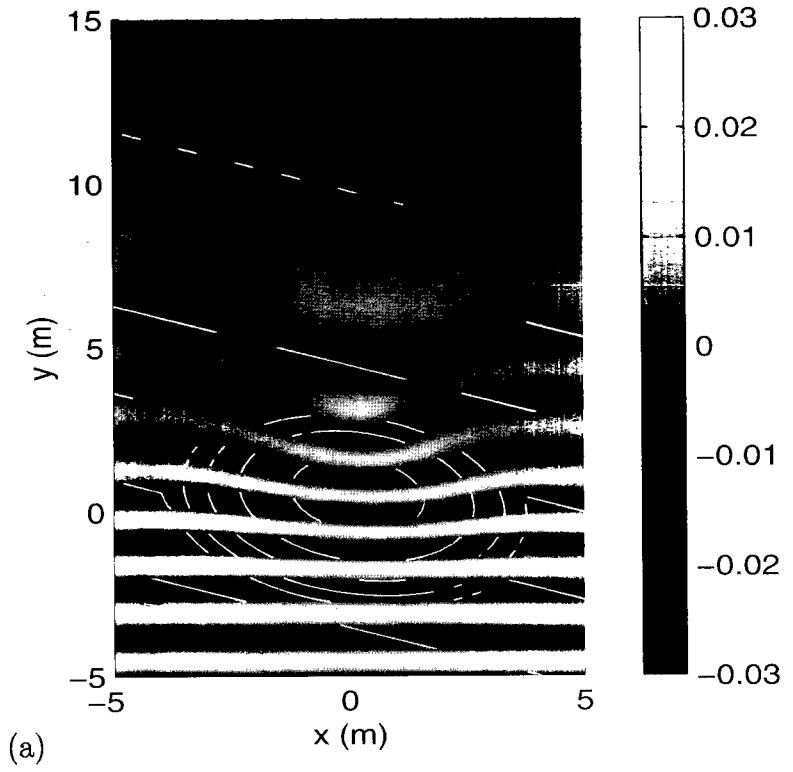

(a)

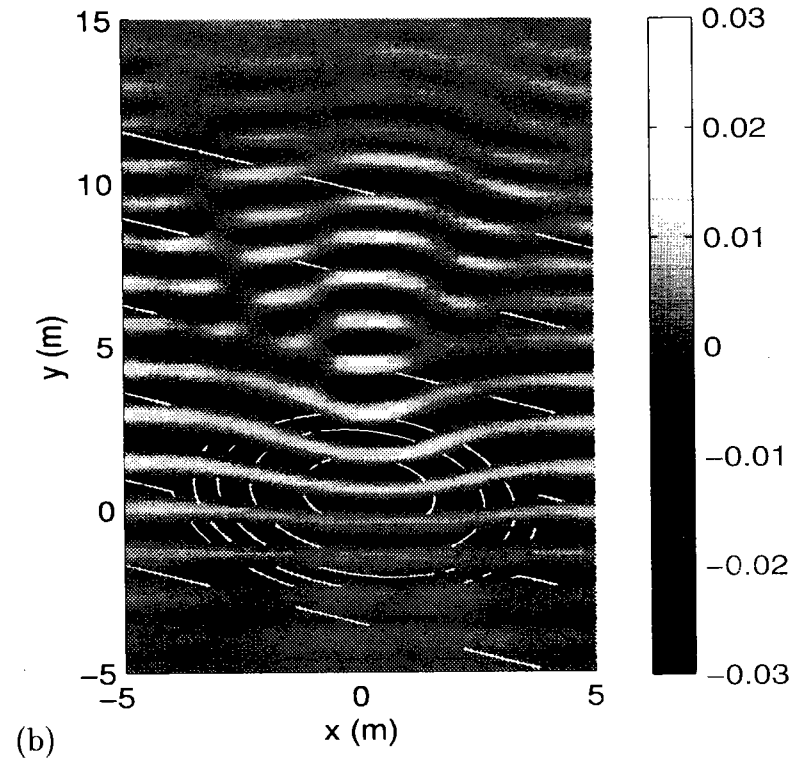

(b)

Figure 17: Snapshot of free surface elevation at time (a)t = 7.4, (b)t= 19.8 (sec)

Part II

Numerical Grid Generation Of an Irregular Region

Numerical Grid generation of an Irregular Region

Summary

A procedure of numerical conformal mapping is established to generate grids of a two-dimensional irregular region for further computations. The approach employs a sequence of Z^n transformations to map an irregular region into a quadralateral region with right angles at each of the four corners. This quadralateral region is then transformed into a rectangular domain by using the boundary integral element method to solve the Laplace mapping equations. Grids are generated in the transformed rectangular domain and are mapped inversely into the original irregular region. The present technique of grid generation is demonstrated and verified in two benchmark problems. For physical applications, steady-state temperature distributions in a circle and an area bounded by two triangles are caculated and verified, using the present techniques. The present technique of numerical conformal mapping can generate grids for the finite element method or boundary-fitted coordinates for the finite difference method.

不規則區域之網格分割數值方法

摘　要

本文建立一數值保角轉換方法，可針對不規則二維區域做網格分割，以提供各種數值計算之用。在利用一連串之 Z^n 轉換及邊界積分數值計算過程，可將不規則區域轉換爲一矩形，轉換後方形格點並與原格點做一對一的對應。爲印証模式之正確性，並以二個應用例子做測試及說明。本文建立之網格切割技術，將可提供有限元素法及有限差分法相關數值模式之應用。

Numerical Grid Generation of an Irregular Region

Contents

1. Introduction

Coordinate systems that are orthogonal, or at least nearly orthogonal near the boundary, make the application of boundary conditions more straightforward[4]. Errors of approximating boundary conditions could propagate toward the field and eventually deteriorate the solution. The error of approximations of the governing equations depends not only on the derivatives of the solution of the governing equations and the grid spacing, but also on the departure of the grids from orthogonality[3].

For a given grid spacing, smooth, orthogonal grids usually result in the smallest error in simple problems. It is desirable to generate grids where the spacing varies smoothly and the angles between grids lines do not become too small. It turns out that it is difficult to generate orthogonal grids for a wide range of problems[1].

The inherent smoothness and boundary slope discountinuities which do not propagate into the field are advantages found by using a system of elliptic partial differential equations as a means of coordinate system generation. However, a disadvantage is that a system of partial differential equation must be solved to generate the coordinate system[5]. Instead of solving the field problem to generate the coordinates, an efficient and accurate numerical method was developed by employing boundary integral element method to the Laplace equations. Boundary-fitted coordinate systems were generated to calculate wave propagation in coastal water when headlands and bays appear in the computational domain[6]. The boundary integral element method not only reduces the required solutions by one dimension to those on the boundaries, but also avoids the repetition of solving the Laplace equations if the generated coordinate system is not desirable. Furthermore, because the forward and inverse transformations were formulated by solving Laplace equations in their approach[6,7], the generated grid system are thus conformal and orthogonal. The application of this method was shown quite successful[6,7]. Such a method is limited to cases of a quadralateral region with four right corner angles to ensure the entire region before and after transformations is conformal and orthogonal. In other words, when the four corners are not right angles of a qualateral region, the conformal mapping by solving Laplace equations does not guarrantee an one-to-one transformation.

In the paper, a sequence of Z^n transformation is employed to map a region of arbitrary shape into a quadralateral region with four right corner angles and four smooth curvilinear boundary lines. It is to ensure the subsequent transformation into a rectangle from the quadralateral region is conformal everywhere in the region. The forward and inverse conformal tranformations are accomplished by using the boundary integral element method. To improve numerical accuracy of the generated grids, linear elements of normal boundary derivatives are used in the present approach instead of constant elements[6,7]. Examples of grid generations for complex geometry are illustrated and compared with analytical solutions. Steady-state temperature distribution for regions of complex geometry are calculated and compared with conformal analytical solutions.

2. Transformation into an orthogonal curvilinear system

It is known that an area with four orthogonal curvilinear boundaries can be mapped into a rectangular area without any difficulities[6,7]. To develop techniques for grid generation in a conformal and orthogonal system for regions of any arbitrary shape requires mappings of the arbitrary shape into an area bounded by four orthogonal, curvilinear boundaries. As shown in Fig. 1, a region between two straight lines with angle of α in the W plane is to be mapped into an area with a desired angle of β in Z plane.

$$\frac{dZ}{dW} = W^{A-1} \tag{1}$$

where

$$A = \frac{\beta}{\alpha}$$

After integration of eq.(1), one has

$$Z - Z_0 = \frac{1}{A}(W - W_0)^A$$

where Z_0, W_0 are the branch points in the complex planes of Z and W, respectively. The function of $(W - W_0)^A$ is a multi-value function. A branch cut with the argument $\theta, -\pi < \theta < \pi$, outside of the region is chosen so that the regions are continuous and the transformation function is limited to a single-value function.

The inverse transformation of a region with an angle of β in Z plane into the W plane with an angle α can be written as:

$$W - W_0 = [A(Z - Z_0)]^{\frac{1}{A}}$$

Transformation of a region of an arbitrary shape into a orthogonal, curvilinear region can be accomplished by first chosing four corner points on the boundaries of the region. The complex transformation, Z^n, is performed to obtain four right angles at the corners and elsewhere smooth curvilinear lines.

For physical computations, the derivatives of the transformation function can be shown as follows:

$$\frac{\partial U}{\partial X} = Re[A(Z - Z_0)]^{\frac{1}{A}-1} \tag{2}$$

$$\frac{\partial U}{\partial Y} = Re[iA(Z - Z_0)]^{\frac{1}{A}-1} \tag{3}$$

$$\frac{\partial V}{\partial X} = Im[A(Z - Z_0)]^{\frac{1}{A}-1} \tag{4}$$

$$\frac{\partial V}{\partial Y} = Im[iA(Z - Z_0)]^{\frac{1}{A}-1} \tag{5}$$

where $i = \sqrt{-1}$ is an imaginary number, U and V are the real and imaginary part of W, respectively.. It should be pointed out that eqs.(2), (3), (4), and (5) satisfy the Cauchy-Riemann conditions:

$$\frac{\partial U}{\partial X} = \frac{\partial V}{\partial Y}$$
$$\frac{\partial U}{\partial Y} = -\frac{\partial V}{\partial X}$$

The transformation is therefore conformal except at the boundary points where the transformation has been applied.

3. Transformation into a Rectangular Region

In this section, transformation of the orthogonal, curvilinear system into a rectangle is described for completeness of this paper. The detailed formaulation of boundary integral element method to solve Laplace equation can be found elsewhere[2,6,7]. As shown in Fig. 2, a conformal transformation of region $ABCD$ in $X-Y$ plane into $A'B'C'D'$ in $\xi-\eta$ plane can be achieved by solving the Laplace equations:

$$\frac{\partial^2\xi}{\partial X^2}+\frac{\partial^2\xi}{\partial Y^2}=0 \quad and \quad \frac{\partial^2\eta}{\partial X^2}+\frac{\partial^2\eta}{\partial Y^2}=0 \tag{6}$$

with the boundary conditions determined by the Cauchy-Riemann conditions:

$$\frac{\partial\eta}{\partial n}=0 \qquad on \quad \xi=0 \quad and \quad \xi=\xi_0 \tag{7}$$

$$\frac{\partial\xi}{\partial n}=0 \qquad on \quad \eta=0 \quad and \quad \eta=\eta_0 \tag{8}$$

where n is the outward normal direction of the boundaries.

Applying the Divergence theorem, eq.(6), can be written in the following form:

$$\alpha\phi(P)=\int_\Gamma[\phi\frac{\partial \ln r}{\partial n}-\ln r\frac{\partial\phi}{\partial n}]ds$$

where $\phi=\xi$ or η, Γ is the boundary of the region, r is the distance between a singular point to a point on the boundary, $\alpha=2\pi$ when the singular point is inside the region. α is the interior angle ($\frac{\pi}{2}$ or π in this case) when the singular point is located on the boundary. Discretizing the boundary and choosing the singular points as the boundary nodal points, a simultaneous equation system of the unknown function values or its derivatives can be formulated and solved.

The inverse transformation can be accomplished by solving the Laplace equations of X and Y with independent variables of ξ and η. It should be noted that the boundary condition is one of the Dirichlet type. In an approximate formulation[6,7], the derivatives of dependent variables can be estimated by employing the Cauchy-Riemann conditions. Therefore, the inverse transformation can be formulated without actually solving the Laplace equations. However, a constant element approximation of the derivatives of dependent variables does not yield accurate grids. It is

improved by allowing the derivatives of dependent variables to vary linearily along each boundary element. Taking into account the multiple normal derivatives at the four corners, the Laplace equations of X and Y are solved simultaneously with $2N+8$ unknown derivatives, where N is the total nodal points representing the boundaries. The formulation of the boundary integral element method produces $2N$ equations. Applying the Cauchy-Riemann contions to the four corners induces an additional 8 equations to complete the algebra of the simultaneous equation system. The price of more computational time has been paid to gain accuracy of the derivatives of dependent variables on the boundaries. Nevertheless, the accuracy of the final grid generation is then secured.

For physical computations, the derivatives of X and Y with respect to ξ and η are needed and shown as follows:

$$2\pi\frac{\partial\phi(P)}{\partial\xi} = \int_\Gamma [\phi\frac{\partial}{\partial\xi}(\frac{1}{r}\frac{\partial r}{\partial n}) - \frac{\partial \ln r}{\partial\xi}\frac{\partial\phi}{\partial n}]ds \tag{9}$$

$$2\pi\frac{\partial\phi(P)}{\partial\eta} = \int_\Gamma [\phi\frac{\partial}{\partial\eta}(\frac{1}{r}\frac{\partial r}{\partial n}) - \frac{\partial \ln r}{\partial\eta}\frac{\partial\phi}{\partial n}]ds \tag{10}$$

where ϕ represents X or Y.

Eqs.(9) and (10) can be evaluated in a similar manner of boundary integral element method[2]. In the case of Z^n transformations before the mapping of solving Laplace equations, chain rules are applied to obtain required derivatives. Therefore, the derivatives of dependent variables of the physical $X-Y$ domain with respect to the dependent variables, ξ, η, of the final mapped rectangle can be calculated without any difficulties.

4. Examples of grid generations

The final mapped rectangle is used to generate grids and then inversely transformed to find the coordinates in the physical domain. It should be pointed out that only the boundary information of function (i.e. the dependent variables) and its derivative are required in the boundary integral method. The choice of distribution of grid density is flexible. One can regenerate the grids when the grids are not satisfactory without re-solving the Laplace equations. Furthermore, it is also convenient when an embedding of grids is necessary. Adaptive grids are also easy to generate because the necessary information is exactly the same and on the boundaries. As a matter of fact, the accuracy of the grid generation is limited by those of the linear simulation of the boundary curves of physical domain.

The shape of rectangular meshes in the final mapped domain makes the employment of the finite difference method accurately feasible. In this section, grid generation of a semi-annulus and an area bounded by two triangles is demonstrated and compared with analytical solutions and previous results[6,7]. To verify the accuracy of present numerical conformal techniques, steady-state distribution of heat in a circular region and in an area bounded by two triangles are presented. It should be also pointed out that the boundary integral method becomes singular when a point is located on the boundary. Although it was reported[2] that the singularity can be avoided if one stays away from the boundary within a thickness of an element size, present computations do not encounter such a singular difficulty. All the boundary points on the boundary are approximated by points inside the domain within the distance of 10^{-6} away from the boundary, which is the order of roundoff error of the computational accuracy.

A region of semi-annulus is a curvilinear quadralateral region (Fig. 3). Four corner angles are right angles. The mapping into a rectangle can be performed analytically as:

$$\frac{\ln r - \ln r_1}{\ln r_2 - \ln r_1} = \frac{\eta}{\eta_0}$$

$$\frac{\theta}{\pi} = \frac{\xi}{\xi_0}$$

where r_1 and r_2 are inner and outer radius, respectively. (r, θ) is the polar coordinates within the semi-annulus. The transformed rectangle is bounded by $\xi = 0, \xi_0$, and $\eta = 0, \eta_0$. The grids of the physical domain and transformed region are shown in Figs. 3 and 4. The mapping of semi-annulus does not require Z^n transformation because of

the right angles at four corners. However, the improvement of linear distribution of normal derivatives on the boundaries in the present approach is illustrated in Table 1, which shows the largest numerical relative errors at four corner points have been significantly reduced from 0.015[6,7] to 10^{-5}.

In an area bounded by two triangles, ABCDEF, the angles following the sequence are $\frac{\pi}{4}, \frac{3\pi}{4}, \frac{3\pi}{2}, \frac{3\pi}{4}, \frac{\pi}{4}, \frac{\pi}{2}$, Fig. 5. The Z^n transformations are applied to these six points so that the angles become $\frac{\pi}{2}, \frac{\pi}{2}, \pi, \frac{\pi}{2}, \frac{\pi}{2}, \pi$. The inverse transformation after the grids are generated in the mapped rectangle are shown in Fig. 6. Previous results of Tsay, et al.[6,7] are shown in Fig. 7. It is obvious that the present technique maintains a one-to-one transformation for regions of a complex geometry.

It is well known that the differential operator of governing equations in a physical problem remains invariant under a conformal transformation. To further demonstrate the effectiveness of the present approach, the steady-state of heat distribution within a circular region and within a region bounded by two triangles are calculated. To calculate the heat distribution in the transformed domain, the Laplace equation of temperature, T, can be discretized for finite difference method in the order of accuracy of $O(\triangle\xi^2), O(\triangle\zeta^2)$, as:

$$\nabla^2 T_{i,j} = \frac{b^2+d^2}{\triangle\xi^2}(T_{i+1,j} - 2T_{i,j} + T_{i-1,j}) + \frac{a^2+c^2}{\triangle\zeta^2}(T_{i,j+1} - 2T_{i,j} + T_{i,j-1}) \tag{11}$$

where

$$a = \frac{1}{J}\frac{\partial X}{\partial \xi} = d = \frac{1}{J}\frac{\partial Y}{\partial \eta}$$

$$b = \frac{1}{J}\frac{\partial X}{\partial \eta} = -c = -\frac{1}{J}\frac{\partial Y}{\partial \xi}$$

with

$$J = \frac{\partial X}{\partial \xi}\frac{\partial Y}{\partial \eta} - \frac{\partial X}{\partial \eta}\frac{\partial Y}{\partial \xi}$$

For a circular region, the boundary conditions can be specified in the polar coordinate system as the following:

$$T(R,\theta) = 100, \qquad 0 < \theta < \pi$$

$$T(R,\theta) = 0, \qquad \pi < \theta < 2\pi$$

$$T(R,0) = 50$$

$$T(R,\pi) = 50$$

where $R = 100$ in present computations.

The analytical solutions of the steady-state distribution of temperature in a circular region can be found as:

$$T(r,\theta) = 50 + \frac{200}{\pi}\sum_{k=1}^{\infty}\frac{\sin(2k-1)\theta}{2k-1}(\frac{r}{R})^{2k-1} \tag{12}$$

In order to obtain finite-difference numerical solutions of temperature distribution in a circular region, this circular region is first forward transformed onto a rectangle are shown in Figs. 8a-8f, by choosing four points, A, B, C, and D, as the corner points. The numerical solutions are calculated by using finite difference method in the transformed domain (25×25 grids). Computational grids in the rectangular region are then transformed inversely into the physical domain are shown in Figs. 9a-9f. These numerical results of temperature distribution, Fig.10a, are compared with the analytical solutions (Fig.10b), eq.(12). The agreement between two results is very good within the relative error of 10^{-5}.

For an area bounded by two triangles, ABCDEF (Fig. 2), the grids are generated in the transformed rectangle and mapped inversely onto the physical domain, as shown in Fig. 6. Equally distributed grids are chosen in the transformed rectangle for numerical calculations of temperature distribution. The grid resolutions are not good near a concave corner in physical domain (Fig. 6), such as points, A, E and F. However, the grid resolution will be compensated by scaling factors of the transformation when physical quantities are calculated numerically. Because the Laplacian operator is unchanged in the transformations, the steady-state temperature distribution within this area can be found in the transformed domain very easily when the boundary conditions are specified.

For the case of heating from top AFE and cooling at BCD, the temperature distribution in the transformed rectangular is

$$T = \frac{\eta}{\eta_1}(T_1 - T_0) + T_0 \tag{13}$$

with no-flux boundary conditions on AB and DE, and $T_{BCD} = T_0; T_{AFE} = T_1$. Similarly, for the case of heating from DE and cooling at AB, the temperature distribution in the transformed rectangle is

$$T = \frac{\xi}{\xi_1}(T_1 - T_0) + T_0 \tag{14}$$

with no-flux boundary conditions on BCD and EFA, and $T_{AB} = T_0; T_{DE} = T_1$. The ξ_1 and η_1 are the width and height of the transformed domain. The temperature distribution is calculated in the transformed domain (25×25 grids) and equal-temperature contour lines are presented in the physical domain, Figs. 11 and 12. From eqs.(13) and (14), the contour lines are straight lines in the transformed domain and are functions of one independent variable, respectively. In other words, the equal-temperature contour lines coincide with the grid lines both within the transformed and physical domains. With their boundary conditions specified, two numerical results, Figs. 11 and 12, show excellent agreement with analytical solutions, eqs.(13) and (14), to a relative errors of 10^{-5}, respectively.

5. Conclusions

A numerical conformal mapping technique is developed in this paper for transformation of a two-dimensional region of a complex geometry into a rectangular area. The boundary of a two-dimensional region of a complex geometry can be divided into four parts with four corner points. A sequence of Z^n transformation map a region of any shape into a curvilinear quadralateral region with four right corner angles. A branch-cut has to be chosen so that the mapping remains continuous and unique. Such a curvilinear quadralateral region is then mapped into a rectangle by employing boundary integral element method to solve the Laplace transformation equation. Present conformal grid system provides more accurate numerical grids than those of Tsay et al[6,7]. It is found that the boundary points can be approximated by points inside the domain with a distance of 10^{-6} from the boundary. Suitability of finite difference method in the transformed rectangle is illustrated for steady-state temperature distribution in a circular region. Very accurate numerical solutions have been obtained. When a transformation is conformal, the grid lines are also equal-temperature lines when the boundary conditions and the corner points are chosen appropriately. The steady-state temperature distribution within an area bounded by two triangles is demonstrated and show excellent results. Present numerical conformal technique can be employed as a pre-processing to generate grids in the finite element method. Accuracy of grids generated of present approach depends on the approximation of the boundaries.

References

1. P. Knupp, and S. Steinberg, *Fundamentals of Grid Generation*, CRC Press, 3, 1994.
2. J.A. Liggett, and P.L.-F. Liu, *The Boundary Integral Element Method for Porous Media Flow*, Allen & Unwin, London, 23-26; 32-33, (1983).
3. C.W. Mastin, and J.F. Thompson, "Transformation of three-dimensional regions onto rectangular regions by elliptic systems", Numerical Mathematics, Vol.29, 397-407, (1978).
4. J.F. Thompson, Z.U.A. Warsi, and C.W. Mastin, "Boundary-fitted coordinate system for numerical solution of partial differential equations - a review", Journal of Computational Physics, Vol.47, 1-108, (1982).
5. J.F. Thompson, Z.U.A. Warsi, and C.W. Mastin, *Numerical Grid Generation, Foundation and Applications*, North-Holland, 190-191, (1985).
6. T.K. Tsay, B.A. Ebersole, and P.L.F. Liu, "Numerical modelling of wave propagation using parabolic approximation with a boundary-fitted coordinate system," International Journal of Numerical Methods for Engineering", Vol.27. 37-55, (1989).
7. T.K. Tsay, G.T. Yeh, G.V. Wilson, and L.E. Toran, *GRIDMAKER: a Grid Generator for Two – and Three – dimensional Finite Element Subsurface Flow Models*, ORNL-6613, Oak Ridge National Laboratory, Tennessee, (1990).

Table 1. Comparisons of Numerical Results between method of Tsay et al.[6,7] and Present Method.

Nodal Point	Exact Coord.	Previous Numerical Results(Tsay et al.[6,7])	Present Numerical Results
A	(-2,0)	(-2.0013,-0.0095)	(-1.99998,1.32E -5)
B	(-1,0)	(-1.0152,0.0023)	(- 1.000006,6.5 E-6)
C	(1,0)	(1.0152,0.0023)	(1.0 00006,6.5E-6)
D	(2,0)	(2.0013,-0.0095)	(-1.99998,1.32E-5)

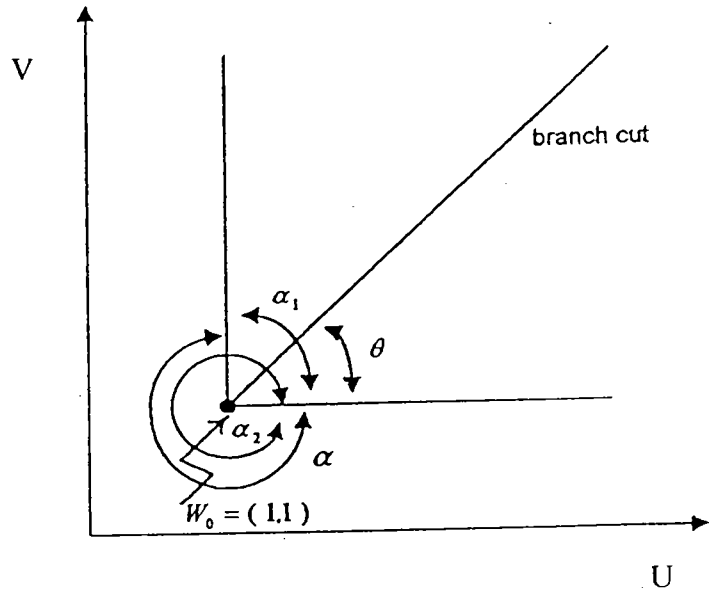

W - plane

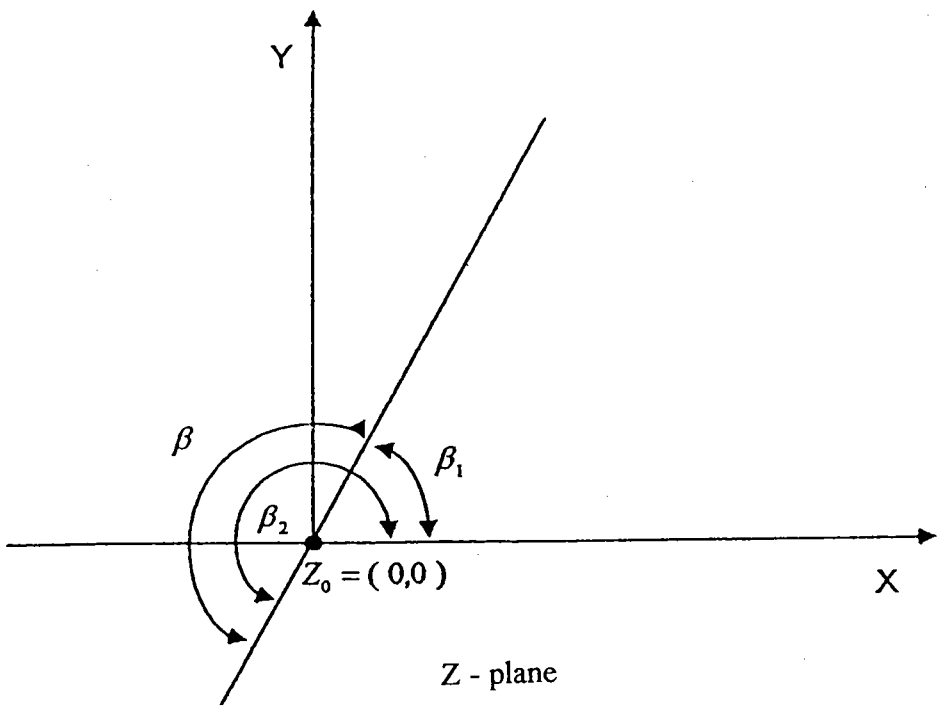

Z - plane

Fig.1 Z^n transformation

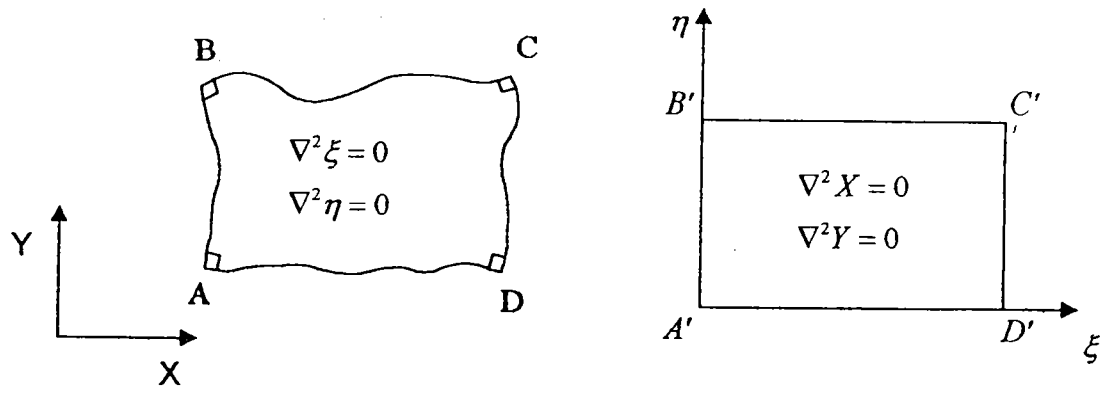

Fig.2 Conformal mapping from ABCD onto A'B'C'D'

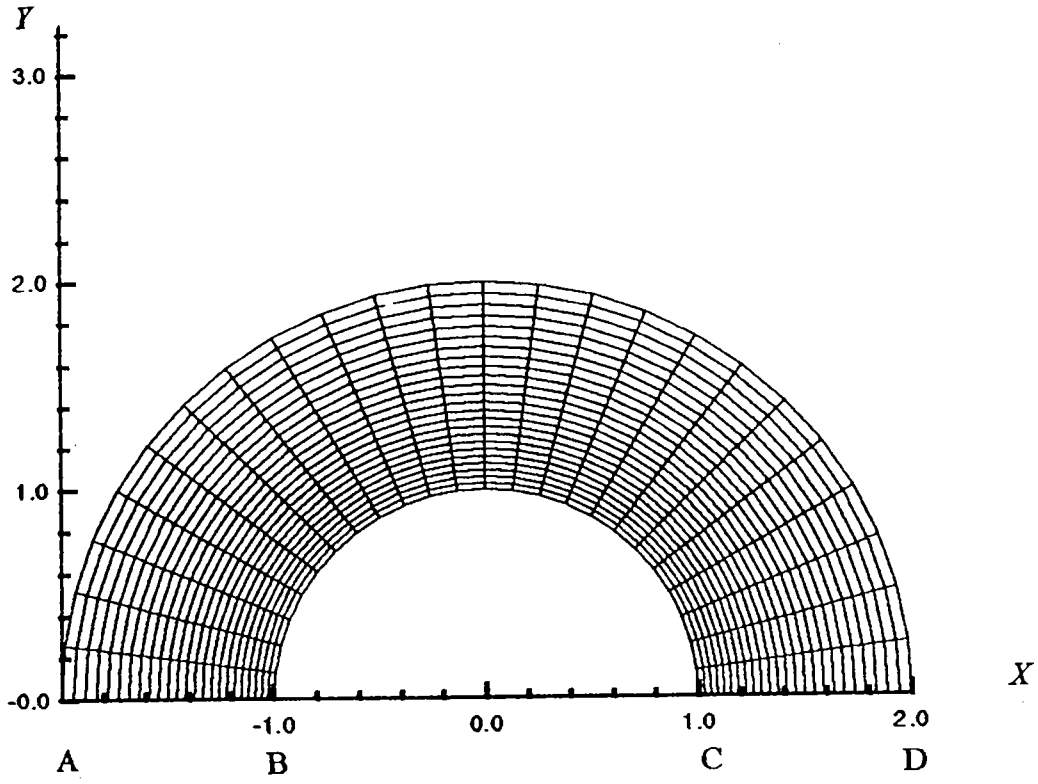

FIg.3 Grid generation of a semi-annulus

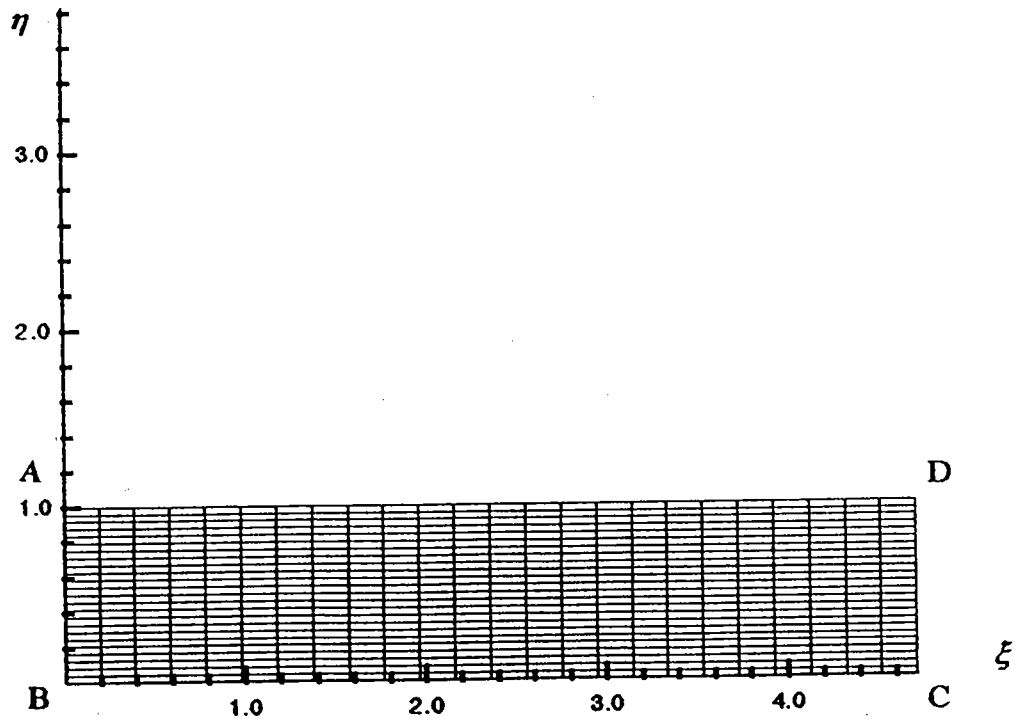

Fig.4 Grid generation of a transformed rectangle

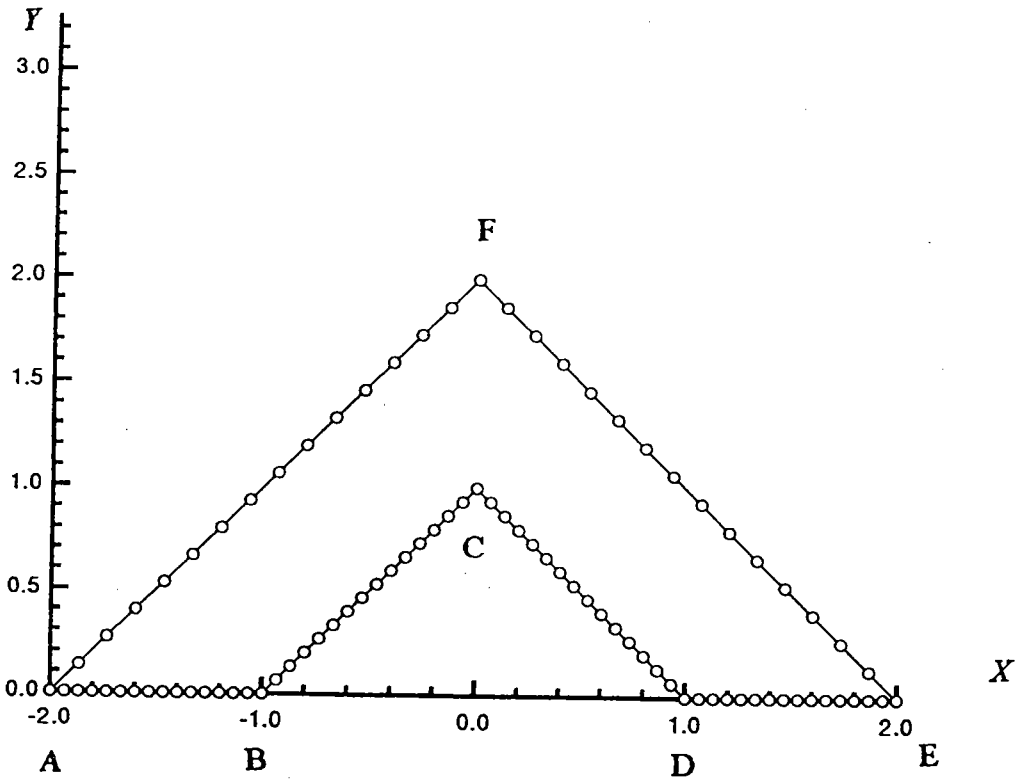

Fig.5 An area bounded by two triangles

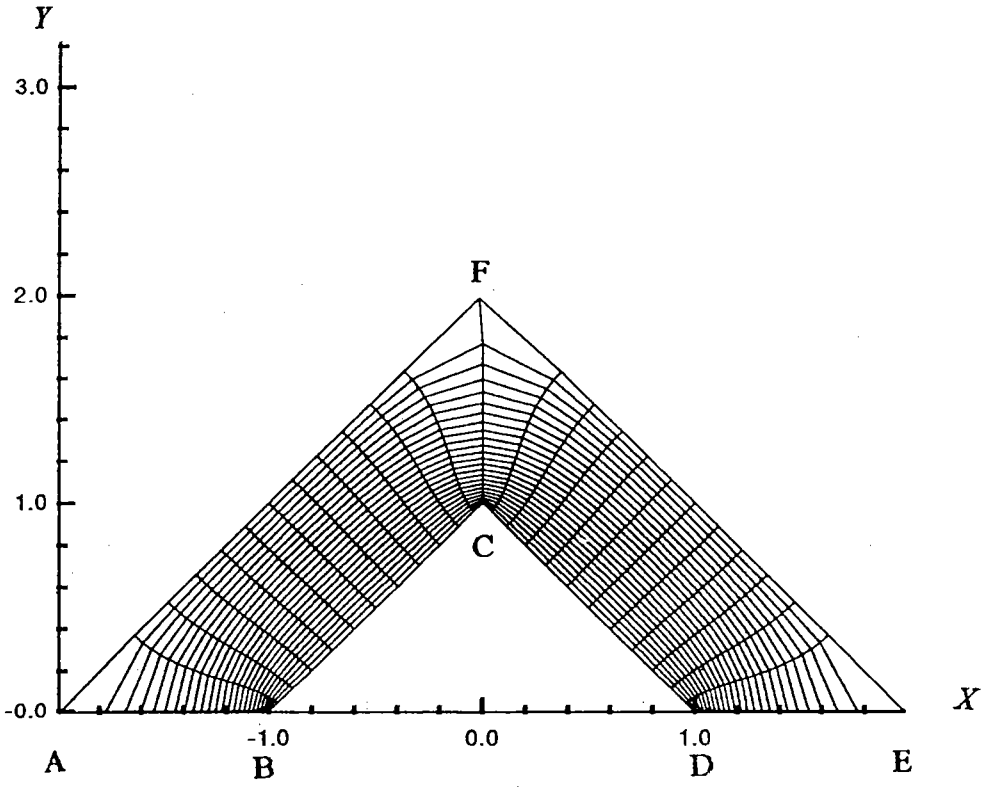

Fig.6 Grid generation on the physical domain by present method

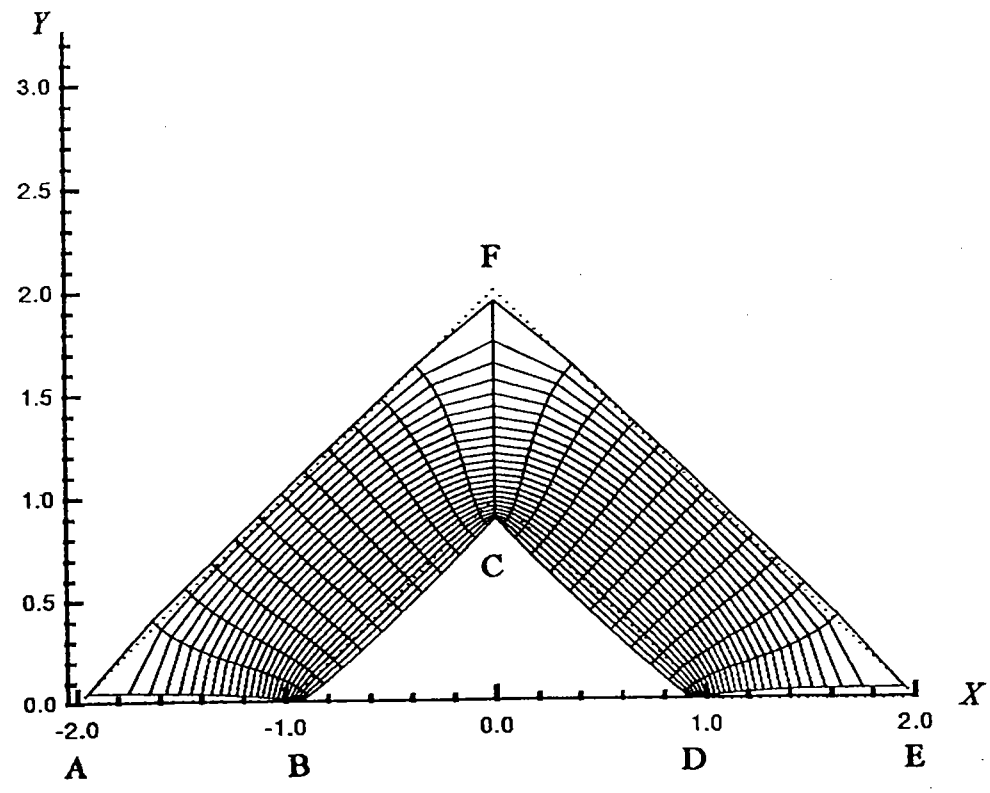

Fig.7 Grid generation on the physical domain by previous method

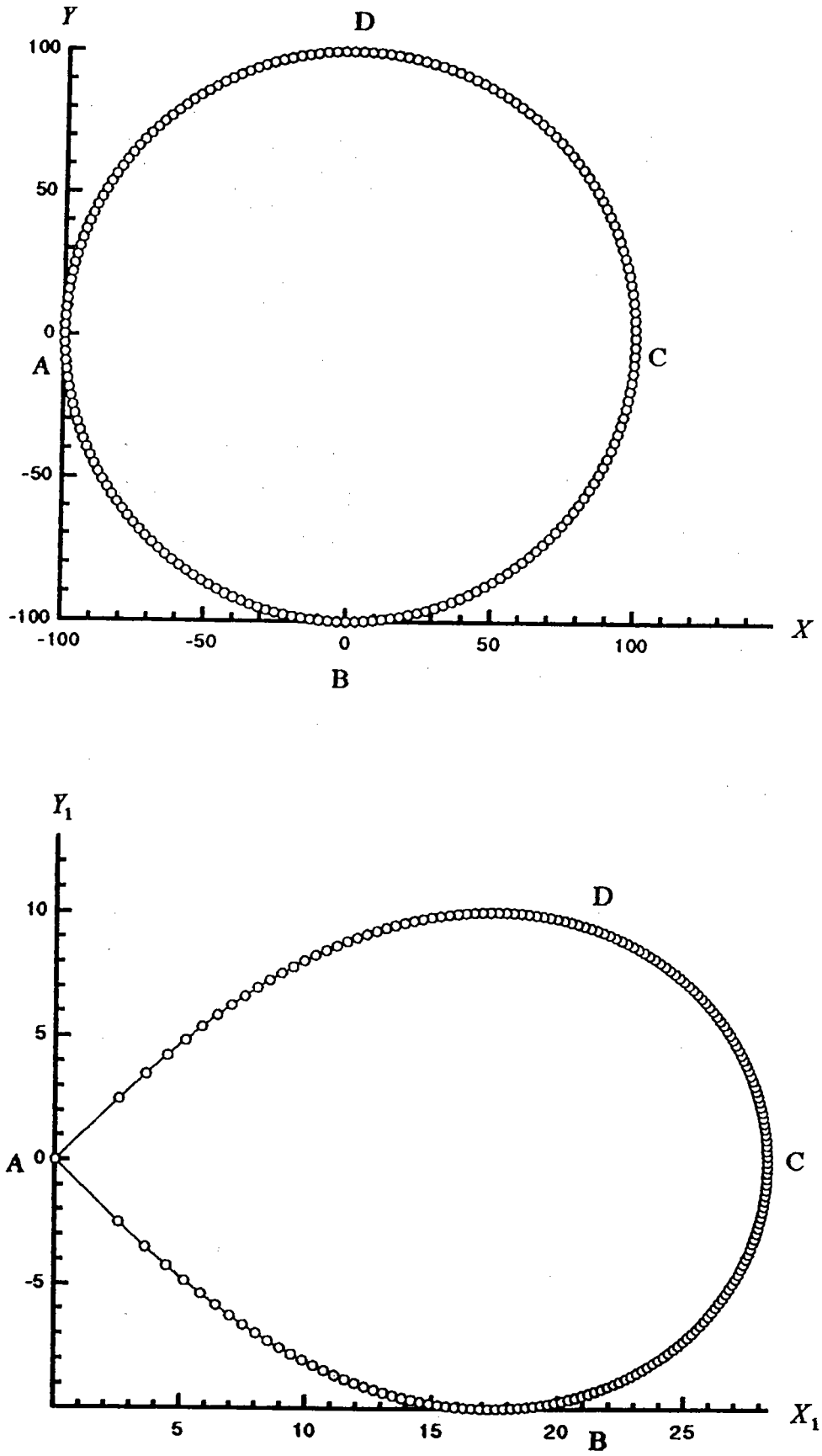

Fig. 8a,b Mapping of a circle into a rectangle

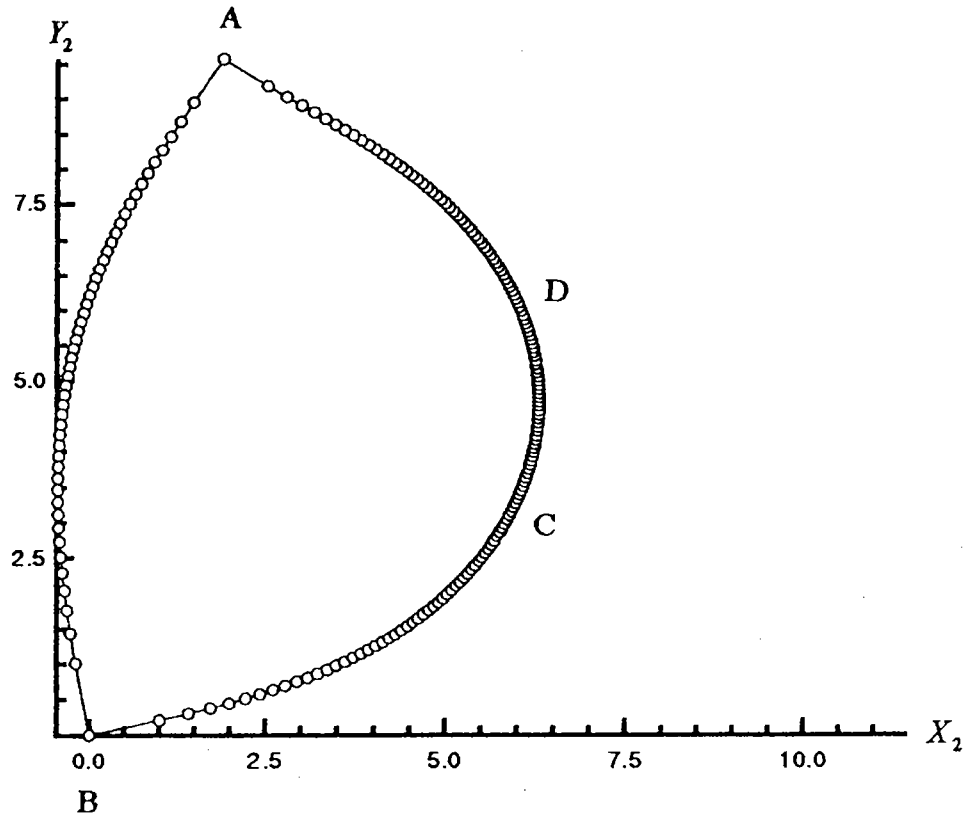

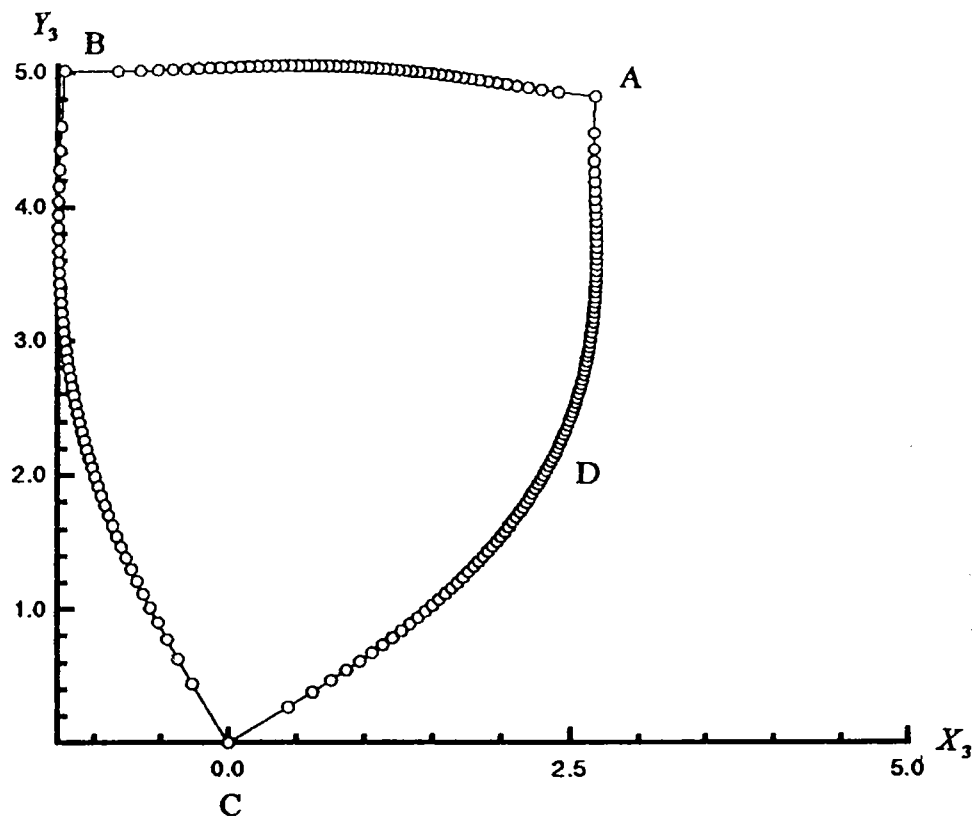

Fig. 8c,d Mapping of a circle into a rectangle

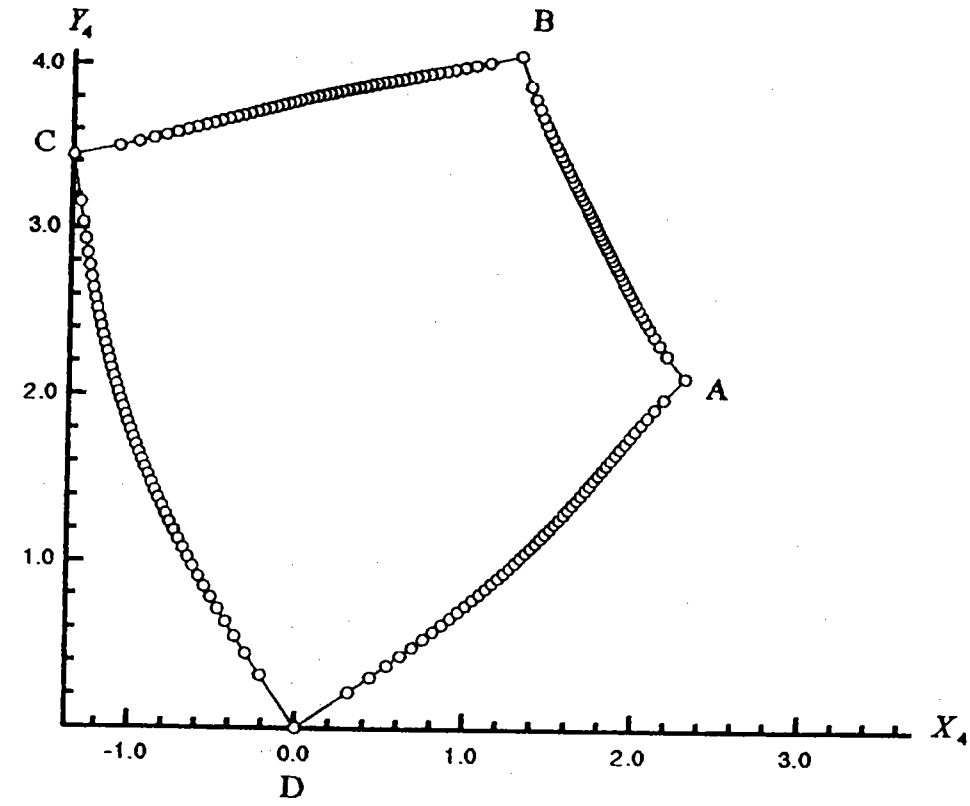

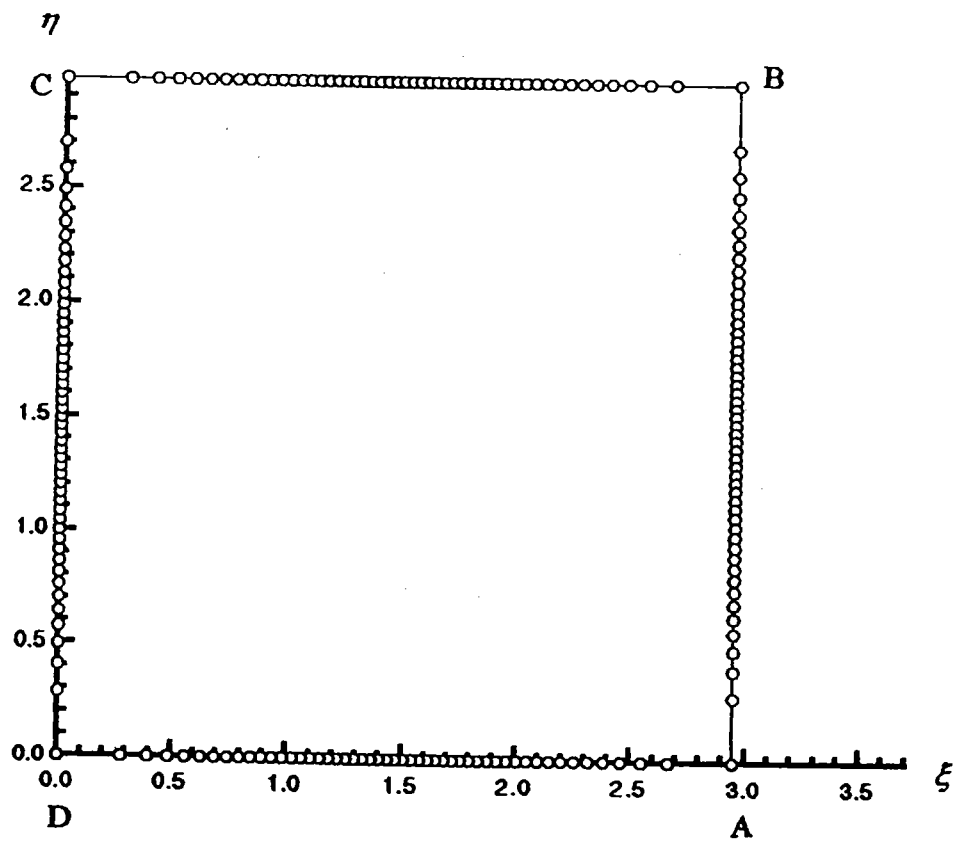

Fig. 8e,f Mapping of a circle into a rectangle

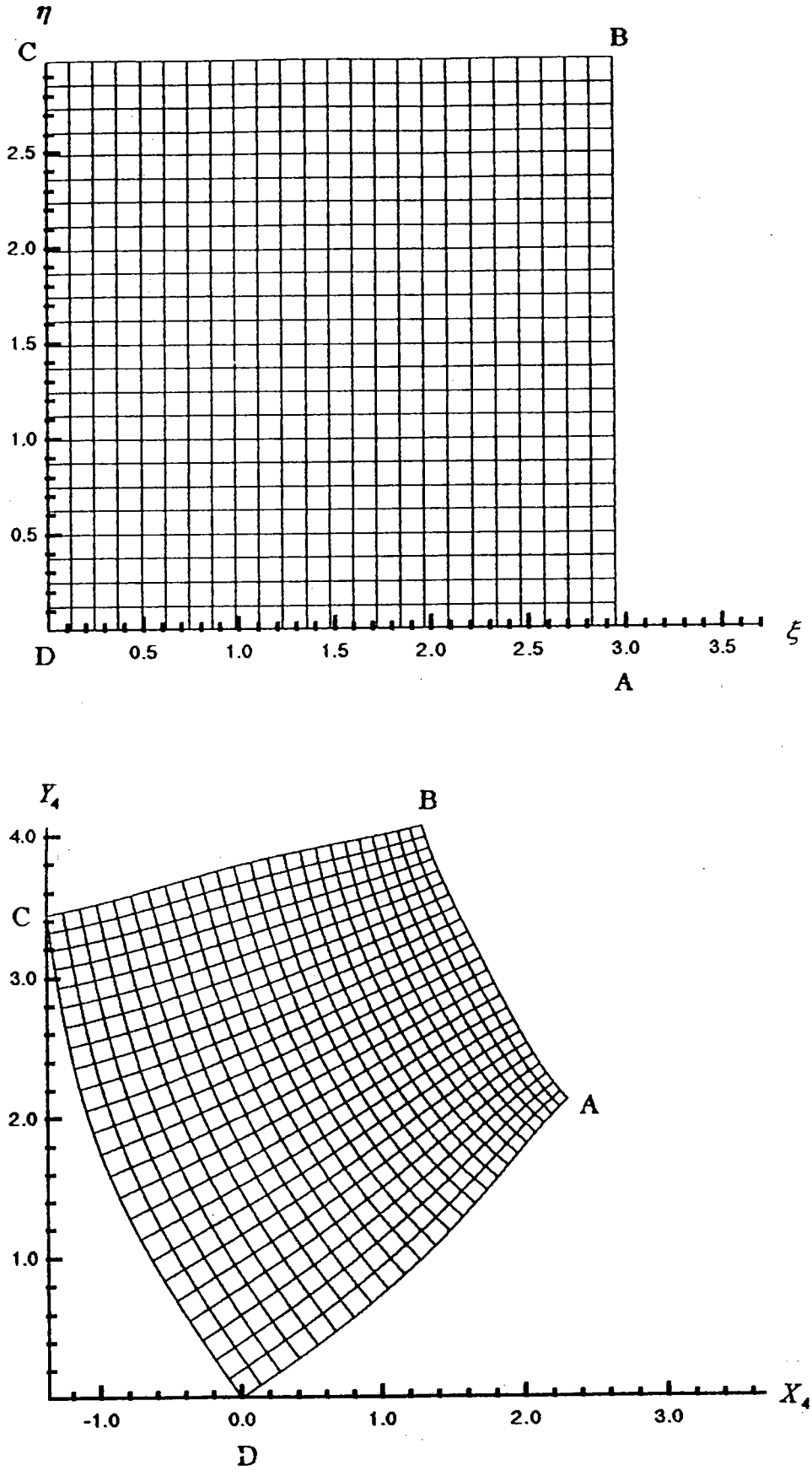

Fig. 9a,b Mapping of grid generation in a rectangle into a circle

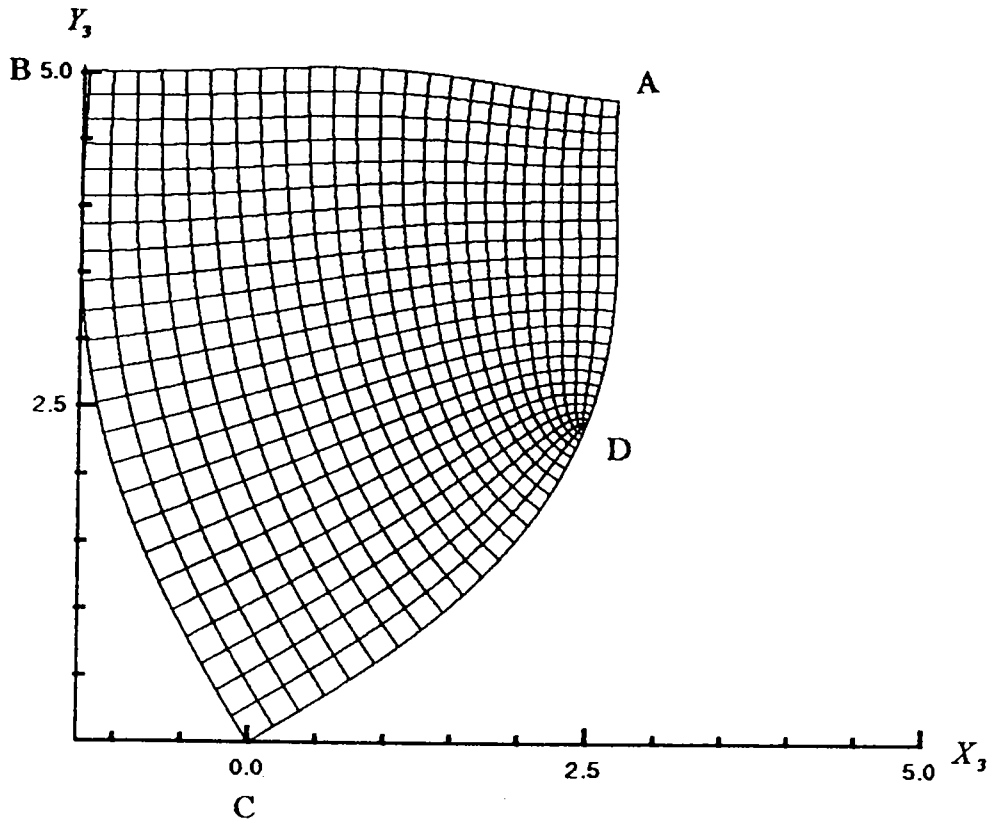

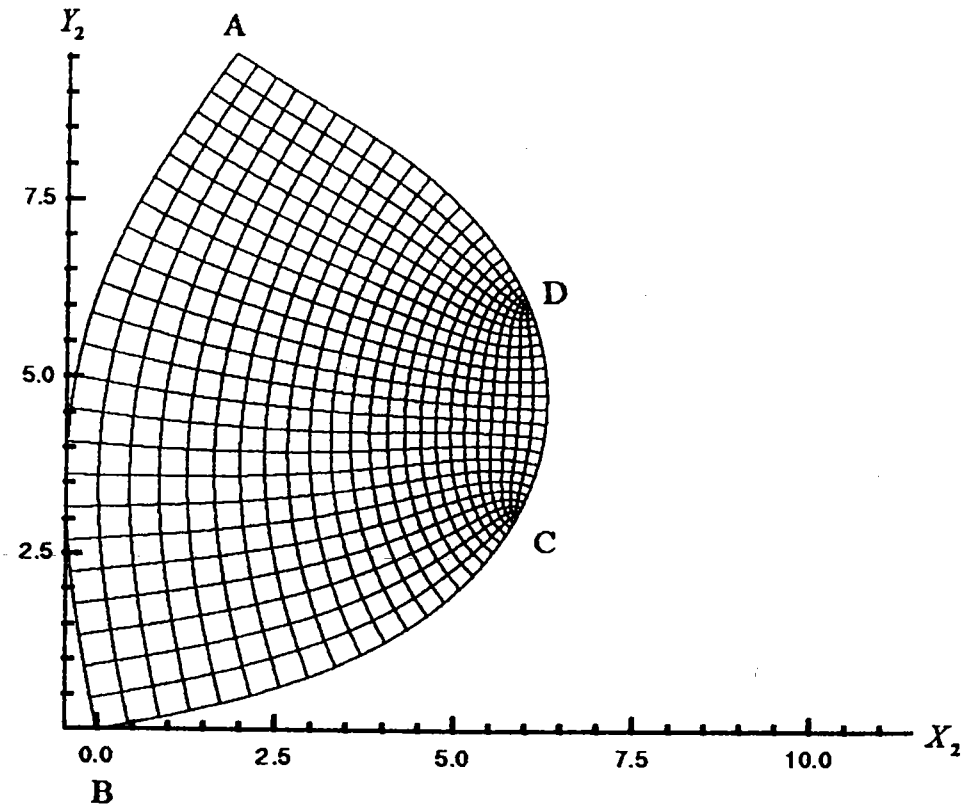

Fig. 9c,d Mapping of grid generation in a rectangle into a circle

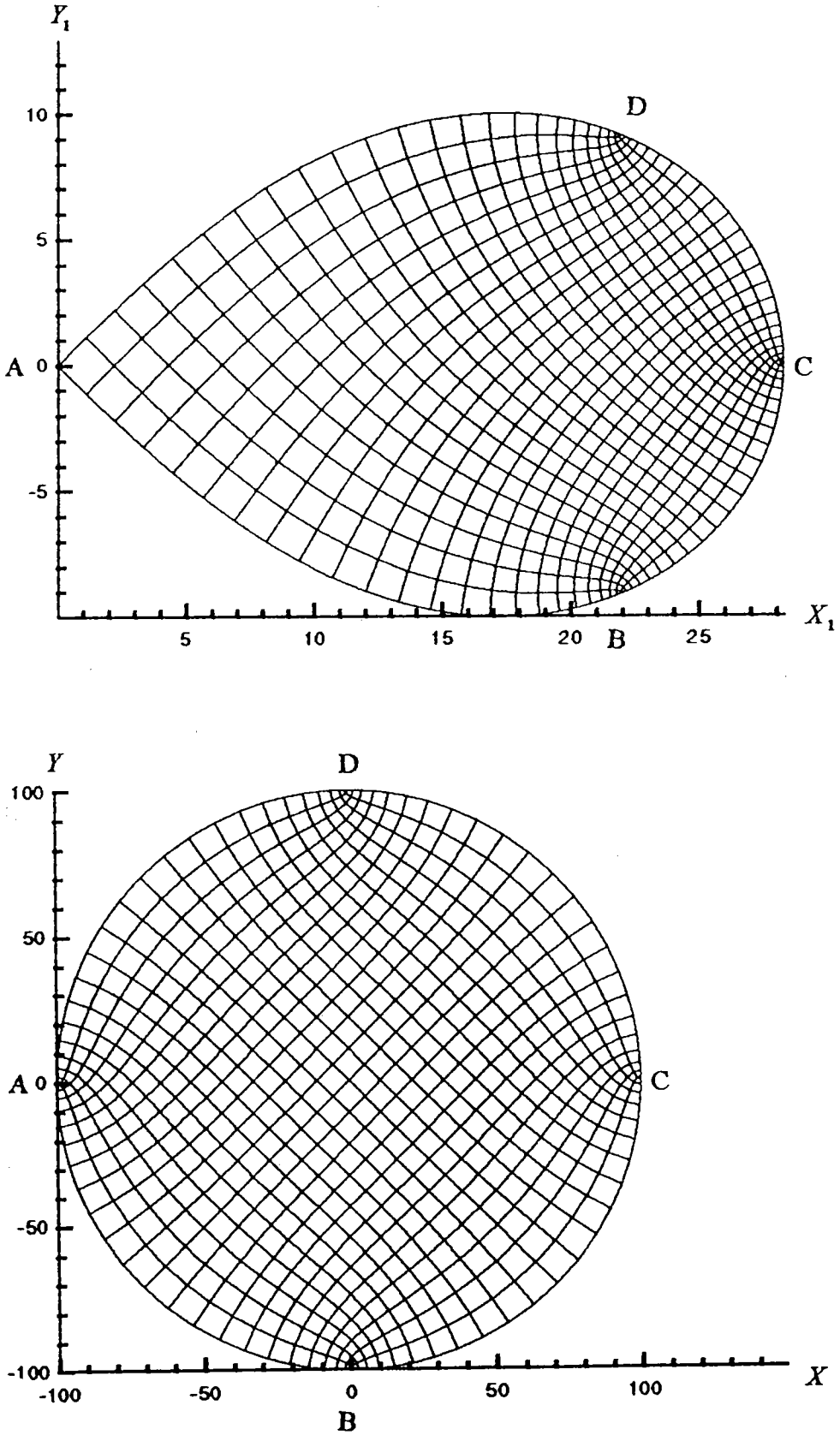

Fig. 9e,f Mapping of grid generation in a rectangle into a circle

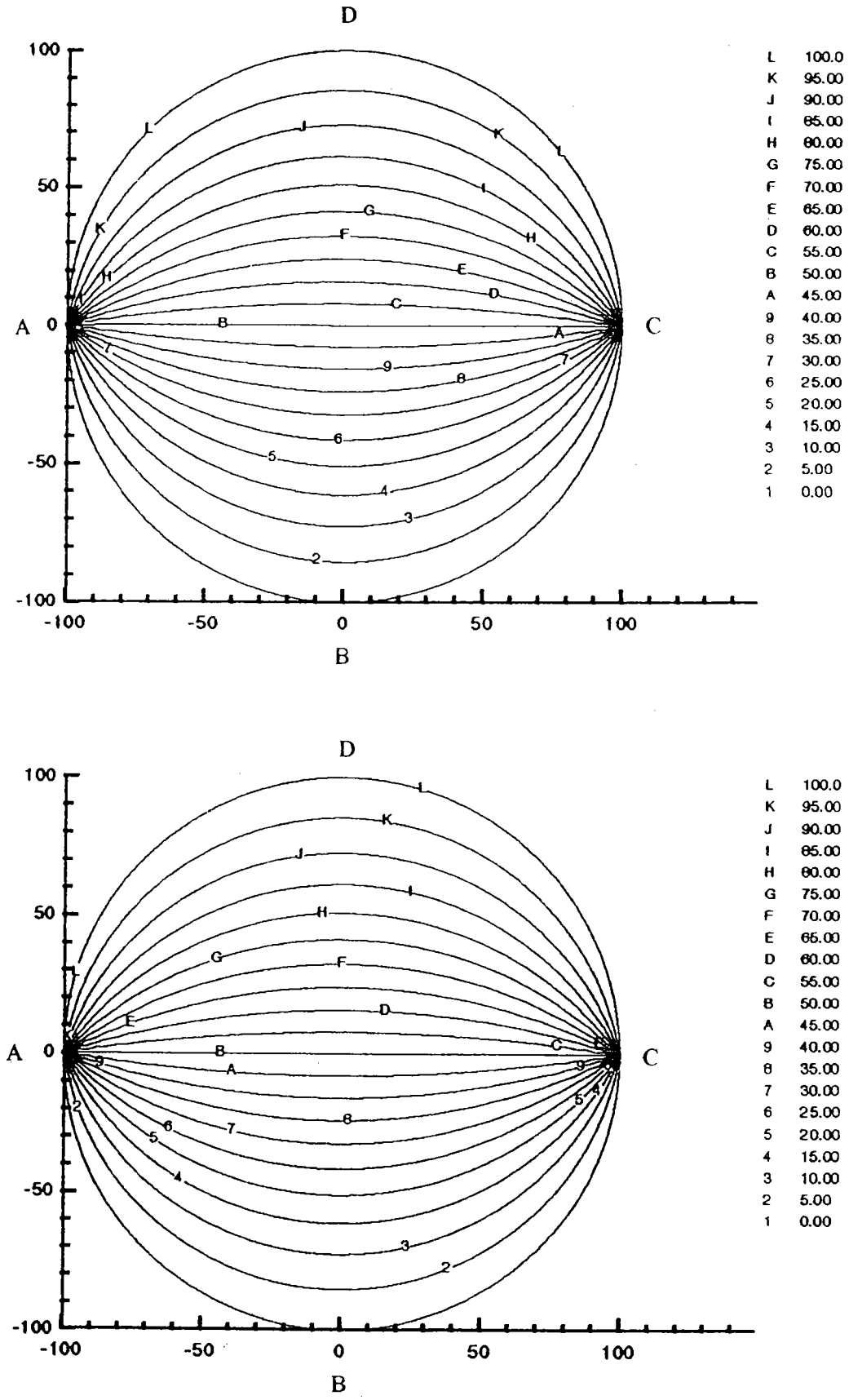

Fig.10 Comparison of analytical solution and numerical results of temperature distribution in a circular region

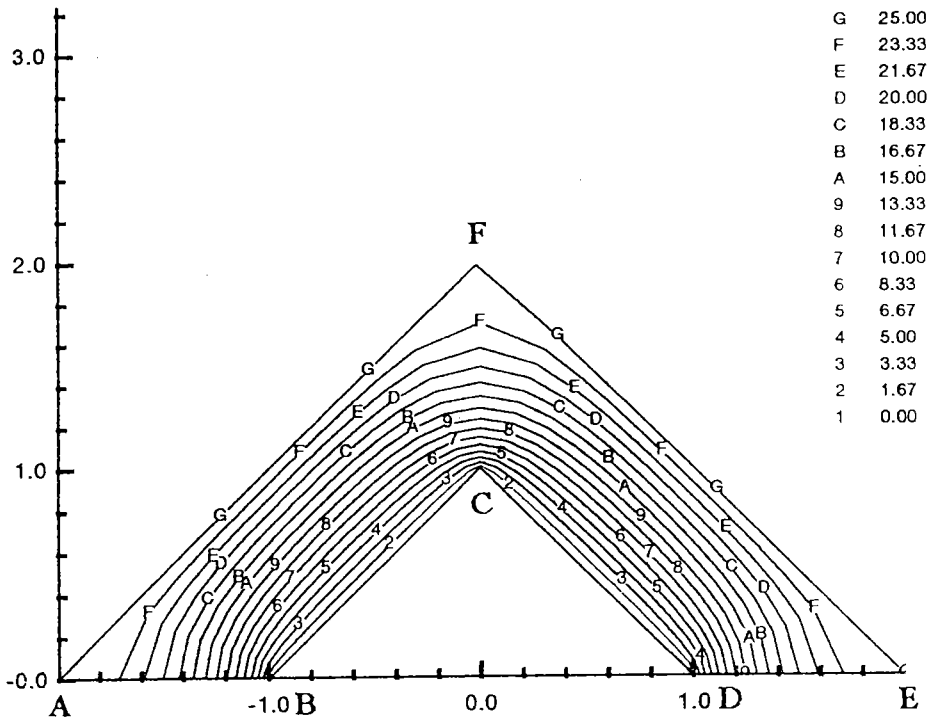

Fig.11 Temperature distribution in an area bounded by two triangles when it is heated from the top

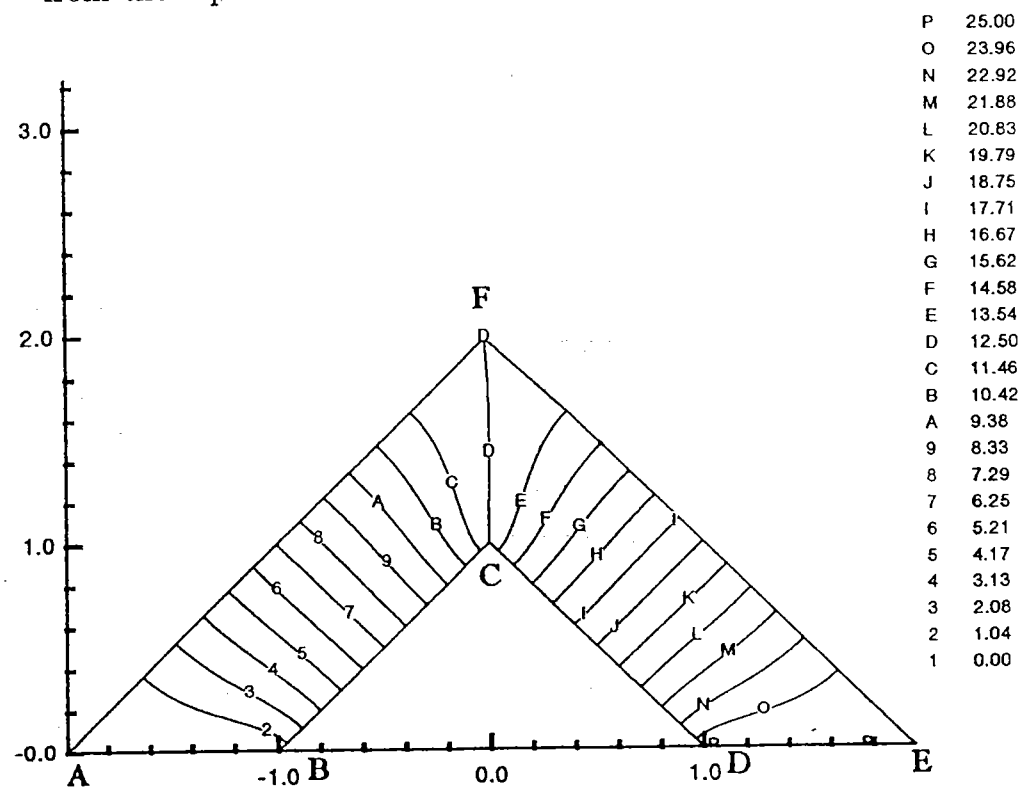

Fig.12 Temperature distribution in an area bounded by two triangles when it is heated from the left

「非線性波浪引起港池振盪之究(二)」期末簡報審查會議紀錄

一、時間：八十九年十二月十一日上午十時

二、地點：本所簡報室

三、主持人：莊副所長甲子

紀錄：陳冠宇

四、審查委員：

交通大學

中興大學

成功大學

港灣技術研究中心

五、出席人員：

台灣大學

港灣技術研究中心

六、主席致詞：

七、劉立方教授闡述有關「非線性波浪引起港池振盪之研究(二)」期末報告：略

八、綜合審查委員意見如下：

(一)期中報告改進情形請說明。

(二)題目 transient 之涵意為何？

(三)報告僅以例子資料說明，是否提供模式程式或相關操作說明。

(四)有限元素考慮三角形或四邊形？未來如何產生？

(五)P73 Fig10 之曲線中存在不規則的擾動，產生之原因為何？

(六)P55 Fig6 圖中理論部份是否與 2D FEM 相同的假設條件？

(七)本計畫為何不引用 full non-linear model 而採用 Weakly non-linear model。

(八)前言中建議增加相關模式的前人研究及發展說明。

(九)入射波與消波層在實際計算如何使用？

(十)線性與非線性與港池幾何形狀對共振之影響有何差異？

(十一)模式是否可能納入碎波條件？

(十二)模式計算時引用 U_α 而不引用 $\overline{U}$ 之原因為何？

(十三)模式之非線性驗證是否可考慮採用產生高階波現象之例子？

(十四)在模式驗證邊界條件是否正確之情形，是否可採用質量守恒原理？

(十五)模式在假設強非線性與弱分散性在物理上是否有矛盾之處?

(十六)部份反射邊界與消波層在數學處理有何差異?

九、委託單位之答覆:

(一)期中報告建議部份已納入期末報告改進。

(二)本模式為 time dependent 故題目以 transient 說明。

(三)本計畫將提供模式原始程式及操作使用說明。

(四)本模式可選擇使用三角形或四邊形元素,未來實際應用於計算花蓮港將引用網格自動產生模式執行格點分割。

(五)曲線中之擾動可能為數值誤差,本例子主要測試消波層之消波功能。

(六)理論部份與 2D FEM 之假設條件相同,與 2D FDM 之比較結果也相近。

(七)採用 Weakly nonlinear model 之原因有二:第一其模式穩定性較佳,第二 full-nonlinear 之適用範圍誰較廣,但相差甚少,未來引用於計算花蓮港之條件 Weakly nonlinear model 即可滿足。

(八)正式報告中將納入此部份之補充。

(九)入射波將以造波方法處理,其後方在放置消波層,以消減由港池之反射波,避免再反射進入港池,消波邊界條件可納入本模式。

(十)共振發生主要為外在波浪頻率與港池自然頻率(與港池形狀有關)相近而發生之共振,非線性或線性波皆可發生共振。僅二者特性不同,也是本研究計畫探討主題之一。

(十一)模式目前未考慮碎波條件,理論上可納入碎波條件。

(十二)模式應用 U_α 之原因為數值計算方便而且計算結果可較正確。

(十三)本計畫已採用甚多應用例子說明模式之正確性，利用產生高階波之現象也是方法之一。

(十四)利用質量守恒原理驗證邊算條件為可行方法。

(十五)非線性之強弱主要以 ε 參數控制，分散性之強弱主要以 μ 參數為指標，數學上二者可分開處理。

(十六)部份反射邊界與消波層邊界處理不同，前者有部份吸收及部份反射，但消波層之功能在完全吸收波能。

十、主席結論：

(一)期末報告初稿同意審查通過。

(二)審查委員之意見，請委託單位納入考量，並於正式期末報告補正。

國家圖書館出版品預行編目(CIP)資料

非線性波浪引起港池振盪之研究(二)

著　　者：蔡丁貴、劉立方、蘇青和
出版機關：交通部運輸研究所港灣技術研究中心
地　　址：台中縣梧棲鎮中橫十路二號
網　　址：www.ihmt.gov.tw
電　　話：(04)6564216
出版年月：中華民國八十九年十二月
印 刷 者：嘉泰彩色印刷股份有限公司
地　　址：新竹市中華路二段 162 巷 20 號
電　　話：035-324142
版(刷)次冊數：初版一刷 100 冊
工 本 費 ：　260 元
展 售 處：
交通部運輸研究所港灣技術研究中心　電話：(04)6564216

GPN：009254890350